Effective kinetics driven by dynamic concentration gradients under coupled transport and reaction

Charlotte Le Traon, Tomás Aquino, Camille Bouchez, Kate Maher, Tanguy Le Borgne

Journal Pre-proofs

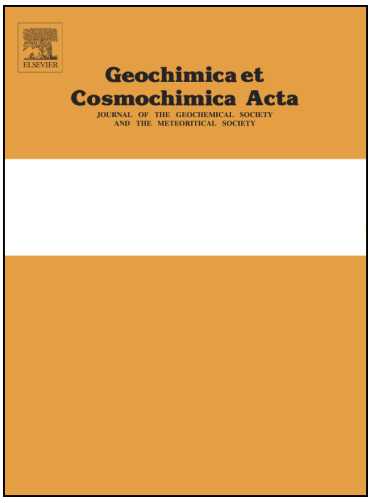

Effective kinetics driven by dynamic concentration gradients under coupled transport and reaction

Charlotte Le Traon, Tomás Aquino, Camille Bouchez, Kate Maher, Tanguy Le Borgne

PII: S0016-7037(21)00258-1
DOI: https://doi.org/10.1016/j.gca.2021.04.033
Reference: GCA 12179

To appear in: *Geochimica et Cosmochimica Acta*

Received Date: 21 October 2020
Accepted Date: 26 April 2021

Please cite this article as: Traon, C.L., Aquino, T., Bouchez, C., Maher, K., Borgne, T.L., Effective kinetics driven by dynamic concentration gradients under coupled transport and reaction, *Geochimica et Cosmochimica Acta* (2021), doi: https://doi.org/10.1016/j.gca.2021.04.033

Effective kinetics driven by dynamic concentration gradients under coupled transport and reaction

Charlotte Le Traon*[1], Tomás Aquino[1], Camille Bouchez[1], Kate Maher[2], and Tanguy Le Borgne[1]

[1]Université de Rennes 1, CNRS, Géosciences Rennes UMR 6118, 35042 Rennes, France
[2]Department of Geological and Environmental Sciences, Braun Hall #118, 450 Serra Mall, Stanford University, Stanford, CA, 94305, USA

March 31, 2021

Abstract

Biogeochemical reaction kinetics are generally established from batch reactors where concentrations are uniform. In natural systems, many biogeochemical processes are characterized by spatially and temporally variable concentration gradients that often occur at scales which are not resolved by field measurements or biogeochemical and reactive transport models. Yet, it is not clear how these sub-scale chemical gradients affect reaction kinetics compared to batch kinetics. Here we investigate this question by studying the paradigmatic case of localized pulses of solute reacting with a solid or a dissolved species in excess. We consider non-linear biogeochemical reactions, representative of mineral dissolution, adsorption and redox reactions, which we quantify using simplified power-law kinetics. The combined effect of diffusion and reaction leads to effective kinetics that differ quantitatively and qualitatively from the batch kinetics. Depending on the nonlinearity (reaction order) of the local kinetics, these effects lead to either enhancement or decrease of the overall reaction rate, and result in a rich variety of reaction dynamics. We derive analytical results for the effective kinetics, which are validated by comparison to direct numerical simulations for a broad range of Damköhler numbers and reaction order. Our findings provide new insights into the interpretation of imperfectly mixed lab experiments, the effective kinetics of field systems characterized by intermittent reactant release and the integration of sub-scale concentration gradients in reactive transport models.

1 Introduction

The kinetics of biogeochemical reactions are used to predict a range of processes, including the weathering of rock, the transport and degradation contaminants, and the nutrient cycling that sustains subsurface microbial life. Given the importance of transport processes in governing the removal and supply of products and reactants and the necessity to consider a variety of spatial and temporal scales, reactive transport models are increasingly used to predict processes occurring in the subsurface (e.g., see reviews by Van Cappellen and Gaillard, 2018; Steefel et al., 2005; Li et al., 2017; Maher and Navarre-Sitchler, 2019; Maher and Mayer, 2019) A host of other studies rely

*Corresponding author: charlotte.letraon@univ-rennes1.fr

on conceptual frameworks that integrate reactive transport principles, with applications ranging from interpretation of global elemental cycles (Lasaga et al., 1994), to catchment elemental fluxes over synoptic (e.g. Kirchner and Neal, 2013) or geologic timescales (e.g. Maher and Chamberlain, 2014), to nutrient cycling at microsites (e.g. Keiluweit et al., 2016). In all cases, biogeochemical kinetics have to be represented at an appropriate temporal and spatial scale. However, kinetic models are generally derived from well-mixed batch experiments in the lab. Yet, reaction kinetics can differ by orders of magnitude from homogeneous batch reactors to heterogeneous field systems (White and Brantley, 2003; Meile and Tuncay, 2006; Maher et al., 2006; Navarre-Sitchler and Brantley, 2007; Li et al., 2008; Salehikhoo et al., 2013; Wen and Li, 2017a; Wen and Li, 2018; Wang et al., 2018). Different hypotheses have been investigated to explain these discrepancies. These include diffusion limitations or geometrical constraints at the pore scale that reduce access of solutes to reactive surfaces compared to fully mixed systems (Molins et al., 2012; Molins et al., 2014; Beckingham et al., 2016; Soulaine et al., 2017; Beckingham et al., 2017; Deng et al., 2018), physical heterogeneity that induces spatially heterogeneous solute fluxes and modifies the effective reactive surfaces (Atchley et al., 2013; Wen and Li, 2017a; Wen and Li, 2018; Jung and Navarre-Sitchler, 2018a; Jung and Navarre-Sitchler, 2018b; Wang et al., 2018) and geochemical heterogeneity, where averaging can also lead to scale effects in effective reaction kinetics (Atchley et al., 2014; Salehikhoo et al., 2013). These studies highlight the role of delayed or heterogeneous access to reactive surfaces at different scales. A complementary question that has received less attention is: what is the impact of heterogeneous and time evolving concentration landscapes on reaction kinetics, when access to reactive surfaces or to other dissolved reactants is not limited?

Concentration gradients are created by spatially heterogeneous or transient release of solutes. They can be sustained by stretching induced by flow, whether at pore scale (Heyman et al., 2020) or at Darcy scale (Le Borgne et al., 2017), and are ultimately destroyed by diffusion. In the case of linear kinetics, heterogeneity in concentration fields does not impact the effective kinetics when access to reactive surfaces or other reactants is not limited. However, for non-linear kinetics that imply the local reaction rate is a non-linear function of local solute concentrations, the average reaction rate over a non-homogeneous concentration field is expected to differ from the local kinetics (Battiato et al., 2009; Battiato and Tartakovsky, 2011; Hubert et al., 2020). Such non-linear reaction kinetics play a central role in a broad range of biogeochemical reactions, including dissolution, redox and sorption reactions (Serrano, 2001; Serrano, 2003; Guo et al., 2015). Yet, it is not known how different types of non-linear kinetics may lead to either enhanced or reduced effective kinetics when considering heterogeneous solute plumes.

Many physical, climatic, and biological processes result in localized and intermittent release of solutes that generate temporally and spatially variable concentration fields in subsurface environments (Fig. 1). Rain events (Fig. 1.a) leach soil and induce pulses of dissolved chemical compounds into groundwater (Murphy et al., 2018). River stage variations (Fig. 1.b) induce pulses of oxygen-rich water in hyporheic zones and the underlying groundwater systems, leading to chemical disequilibrium and the degradation, fixation or release of contaminants, such as organic carbon, nitrate or arsenic (Datta et al., 2009; Malzone et al., 2016; Trauth and Fleckenstein, 2017; Bandopadhyay et al., 2018). Biological activity in general (Fig. 1.c), can induce pulses of chemical compounds (e.g. Hinsinger et al., 2003). For instance, roots release dissolved gases and other compounds through daily cycles of respiration and exudation, and via associated fungal and microbial organisms (e.g. Li et al., 2017). Finally engineered injections (Fig. 1.d) create chemical disequilibrium and trigger a range of reactive pulses. This includes managed aquifer recharge (Magesan et al., 1998; Urióstegui et al., 2016; Al-Yamani et al., 2019), which is often performed by periodically wetting and drying the system (Dutta et al., 2015), leading to biogeochemical reactions such as ammonium-nitrogen reduction and pathogen removal (Abel et al., 2014). Injection of concentrated carbon dioxide into the deep subsurface results

in density-driven instabilities, leading to localized high concentrations of reactive CO_2-rich fluid (Szulczewski et al., 2012). Collectively, reactive pulses play an important role in a broad range of engineered injections, including soil and groundwater remediation (Kitanidis and McCarty, 2012; Rolle and Le Borgne, 2019), seasonal energy storage, through heat, hydrogen or underground pumped storage hydroelectricity (Panfilov, 2010; Pujades et al., 2017; Hermans et al., 2018), geothermal dipoles (Burté et al., 2019), and injection and storage of water used for fracking operations (Llewellyn et al., 2015).

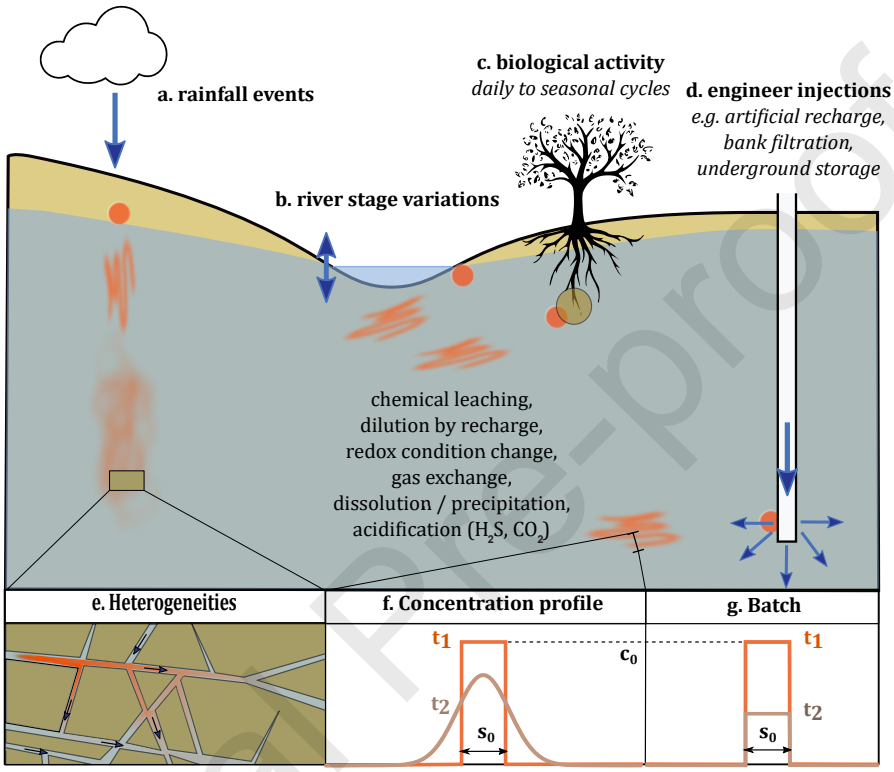

Figure 1: Conceptual representation of biogeochemical pulses in the subsurface. When released, pulses are concentrated and localized (orange dots). As they are transported in the subsurface, they are stretched by velocity gradients and form elongated lamella structures (Le Borgne et al., 2015). Solute concentrations are driven by dilution, which occurs by diffusion along the concentration gradients, and reactions either with minerals or other dissolved solutes. The arrows indicate an injection or an exchange of solute. Four types of processes generating reactive pulses are highlighted: a. soil leaching by rain, b. surface water – groundwater exchanges, c. biological activity (the brown circle represents the root zone), and d. engineered injections. In all these applications, chemical gradients can be enhanced and sustained by physical heterogeneities, as illustrated in inset e. The inset f. illustrates the considered simplified one-dimensional concentration profile that evolve under the action of diffusion and reaction. The effective kinetics of such reactive pulses are compared to batch kinetics that evolve through reaction alone under uniform concentrations (inset g.).

Because chemical gradients are enhanced and sustained by physical heterogeneities (Le Borgne et al., 2013; Heyman et al., 2020) (see inset of Fig. 1), they develop over a range of scales that cannot be fully resolved by field sampling approaches that average solute (e.g., screened groundwater wells) or reactive transport models. Hence, effective kinetic models that capture the effect

of sub-scale concentration gradients are required. Macrodispersion theory, where the dispersive flux is assumed to be proportional to the concentration gradient, tends to strongly underestimate concentration gradients, leading to significant errors when used in reactive transport models (Gramling et al., 2002; Dentz et al., 2011a). Non-Fickian dispersion theories have successfully described the asymmetry of solute plumes resulting from trapping in low velocity areas (Berkowitz et al., 2006). However, this framework aims at describing spatial dispersion of solute plumes and does not quantify subscale concentration gradients governed by mixing (Dentz et al., 2011b). Recent mixing theories have provided a new framework to predict the full distribution of concentrations and concentration gradients both at pore scale (Heyman et al., 2020) and at Darcy scale (Le Borgne et al., 2013). In this framework, solute plumes are represented as ensembles of elongated lamellar structures, i.e. solute filaments elongated in one direction and compressed in the other. The latter develop systematically in heterogeneous media both at the pore (De Anna et al., 2014b) and Darcy (Le Borgne et al., 2014) scale. This is due to velocity gradients at different scales that deform solute plumes into such filaments, whose formation and merging controls mixing rates (Le Borgne et al., 2015). At the scale of a solute lamella, the effect of stretching on the enhancement of concentration gradients and mixing is quantified explicitly by a change of variable that leads to one-dimensional equation formally identical to a diffusion equation in the direction perpendicular to the lamella (Villermaux, 2019). The full distribution of concentration is then predicted from the distribution of stretching rates. While this framework has been successfully used to model mixing-limited reactions (De Anna et al., 2014a; Rolle and Le Borgne, 2019), its coupling with other types of reactions, such as solid-fluid reactions is an outstanding challenge. The key difficulty for this is to first solve analytically the coupling of diffusion transverse to solute lamella with non-linear kinetic laws.

Here we use analytical solutions and numerical simulations to establish the effective kinetic laws that result from coupled diffusion and non-linear reactions in spatially and temporally variable concentration gradients. We consider pulses of solute that react either with a homogeneously distributed solid phase or fluid phase, both in excess with respect to the transported solute. Hence, there is no limitation of access to reactive surfaces or other reactants, which allow use to isolate and formalize the coupling between non-homogeneous concentration distributions and non-linear kinetics. Dilution of solute concentration by mixing with the background fluid transfers high concentrations towards lower concentrations (Kitanidis, 1994), which may either reduce or enhance the average kinetics, depending on the reaction order of the local kinetics. Although mixing plays an important role in this problem, it does not act to bring reactants into contact as extensively studied in the context of mixing-induced reactions, where reactions are limited by the mixing of spatially segregated reactants (see recent reviews of Rolle and Le Borgne, 2019; Valocchi et al., 2019). Instead, we study how changes in concentration distributions by mixing may lead to the emergence of effective kinetics that differ from local kinetics. In complex multi-component reactions, this effect acts together with a range of other processes and therefore it is difficult to understand and quantify. Therefore, although we have studied a simplified reaction in order to isolate a particular phenomenon, our results are expected to be relevant to a large range of geochemical systems, where this effect acts together with other known mechanisms, including spatial segregation of reactants either in fluid or in solid phases. In section 2, we present the reactive transport problem. In section 2.5, we define the studied effective quantities. In section 3, we present the numerical and analytical results for a range of Damköhler numbers and non-linear kinetics. In the section 4, we discuss the implications of our findings for different types of reaction, including mineral dissolution, redox reactions and soprtion.

2 Reactive transport problem

2.1 Reaction kinetics

We study the reaction of a mobile aqueous species, with concentration c, which reacts with other aqueous species or with a solid surface. The latter are assumed to be in excess and homogeneously distributed, so that the reaction kinetics r(c) only depends on the concentration c through the non-linear rate law:

$$r(c) = kc^{\beta}, \tag{1}$$

where $\beta > 0$ is the effective order of the reaction and k is the reaction rate constant, which integrates the effect of other species in excess (units $[\mathrm{mol}^{1-\beta} L^{d(\beta-1)} T^{-1}]$, where d is the spatial dimension).

In a well-mixed batch reactor, the concentration c is homogeneous in space and depends only on time (see lower right inset of Fig. 1). The concentration decreases everywhere according to the reaction rate (1), so that the kinetic rate law describing the evolution of the mean concentration $\overline{c}$ as a function of time t is given by

$$\frac{d}{dt}\overline{c} = -r(\overline{c}), \tag{2}$$

with $\overline{c} = M/V$, where M is the mass of reactant and V is the volume of the batch reactor.

Although it is simplified, the system isolates the effect of transient concentration gradients on upscaled kinetics. The characterization of this basic yet non-trivial system may thus guide the understanding of more complex biogeochemical systems, where this effect is coupled to other mechanisms, such as heterogeneous reactive surfaces, spatial segregation of multiple elements and mixing limitations. As discussed in section 4, it is relevant for mineral dissolution far-from-equilibrium (Hellmann and Tisserand, 2006; Maher, 2011; Guo et al., 2015), for non-linear sorption kinetics (Weber J. et al., 1991; Perry et al., 1997; Serrano, 2003) and for homogeneous redox reactions where β depends on the stoichiometric coefficients (Bethke, 1996; Bleam, 2017). We focus on $\beta \neq 1$, because dilution by mixing has no effect on linear reactions in the sense that the upscaled kinetics are the same as the local kinetics in this case. Indeed, for the linear reaction, $\beta = 1$, mass decay over time is independent of the spatial concentration distribution.

2.2 Reactive pulses

We wish to compare the batch dynamics Eq. (2), to the dynamics of the average concentration under diffusive transport for the same local reaction. Thus, we consider the reactant to be described by a non-homogeneous concentration $c(x,t)$ depending on both position x and time t (see lower middle inset of Fig.1). We assume that the concentration is independent of the other spatial coordinates y and z over a reference surface S. This assumption is taken here for simplicity of analytical derivations, and can be relaxed to consider three dimensional transport processes following the same approach. The concentration is thus assumed to obey the diffusion-reaction equation,

$$\frac{\partial c}{\partial t} - D\frac{\partial^2 c}{\partial x^2} = -r(c), \tag{3}$$

where $D[L^2T^{-1}]$ is the diffusion coefficient, which we assume to be constant. The initial condition is taken as a rectangular pulse identical to the batch conditions, but the pulse is allowed to diffuse in an infinite one-dimensional domain. At the boundaries, concentration tends to zero. Note that, in natural systems, boundaries limiting diffusive mass transfer would ultimately lead to a homogenization of the domain and a convergence to the batch reaction rates. Our results hence

describe the transient regimes before this happens. For a reference scale L larger than the pulse characteristic size, $L \gg \sqrt{Dt}$, the mean concentration is,

$$\overline{c} = \frac{M}{LS}. \tag{4}$$

The temporal evolution of the mean concentration is obtained by integrating Eq. (3) over space,

$$\frac{d}{dt}\overline{c}(t) = -\frac{k}{L}\int_{-L/2}^{L/2} dx\, c(x,t)^{\beta}. \tag{5}$$

Note that only the reaction term contributes directly to the change in mass, which can be shown by integration by parts. However, transport affects the shape of the concentration profile, and thus indirectly impacts the total mass and the average concentration. This one-dimensional diffusion-reaction approach is also relevant to understand the effect of plume stretching on reaction kinetics in heterogeneous media. Indeed, solutes transported in the subsurface tend to follow elongated lamella structures (Le Borgne et al., 2015) where concentrations vary weakly along the stretching direction and concentration gradients develop mostly in one-dimension transverse to lamellae (Fig. 1).

2.3 Non-dimensional units

In order to meaningfully compare the dynamics for different conditions, it is convenient to define non-dimensional quantities in terms of values characterizing the different physical processes at play. We define the non-dimensional position as $x_* = x/w_0$, where w_0 is the initial pulse width, the non-dimensional concentration as $c_* = c/c_0$, where c_0 is the initial concentration, and the non-dimensional average concentration as $\overline{c}_* = \overline{c}L/(c_0 w_0)$. Note that the non-dimensional initial concentration and average concentration are thus $c_*(0) = \overline{c}_*(0) = 1$. Furthermore, we define non-dimensional time as t/τ_R, where

$$\tau_R = \frac{1}{k c_0^{\beta-1}} \tag{6}$$

is the characteristic reaction time (inverse rate) associated with the initial concentration c_0. In the following, we drop the asterisk for notational brevity. All quantities discussed are non-dimensional in the sense discussed here unless mentioned.

In non-dimensional units, the kinetic equation for the batch is,

$$\frac{dc}{dt} = -c^{\beta}, \tag{7}$$

which can be solved with the initial condition $c(0) = 1$ to yield,

$$c(t) = [1 + (\beta - 1)t]^{-\frac{1}{\beta-1}}. \tag{8}$$

This solution holds whenever $\beta \neq 1$, that is, for nonlinear reactions. The special case of linear reactions leads to the classical $c(t) = e^{-t}$ exponential decay.

In order to account for the effect of dilution by mixing, we identify the time needed to homogenize the width of the initial condition as

$$\tau_D = \frac{w_0^2}{2D}, \tag{9}$$

corresponding to the time to homogenize a unit distance in nondimensional coordinates. The relative importance of reaction with respect to dilution is characterized by the dimensionless Damköhler number

$$\mathrm{Da} = \tau_D/\tau_R. \tag{10}$$

Fast reactions relative to dilution correspond to $\mathrm{Da} > 1$, while slow reactions correspond to $\mathrm{Da} < 1$. In nondimensional terms, the diffusion-reaction equation becomes

$$\frac{\partial c}{\partial t} - \frac{1}{2\mathrm{Da}}\frac{\partial^2 c}{\partial x^2} = -c^\beta. \tag{11}$$

Note that, in nondimensional variables, the initial condition is a rectangular pulse of unit width. The dimensionless total mass obeys

$$\frac{d}{dt}\overline{c}(t) = -\frac{1}{L}\int_{-L/2}^{L/2} dx\, c(x,t)^\beta. \tag{12}$$

All introduced parameters and their units are given in table 3 (Appendix A).

2.4 Numerical analysis

To explore the different effective reaction regimes, we first solved Eq. (11) numerically using Matlab's *pdepe* method, a numerical solver for one-dimensional partial differential equations (Skeel and Berzins, 1990). We use Neumann boundary conditions, i.e. no flux boundary condition, and a rectangular pulse of unit normalized width as initial condition (Fig. 1f). The domain size is chosen large enough to maintain close to zero concentrations at the domain boundaries at the end of the simulation, and the grid discretization is refined to ensure the convergence of the solver. To analyze the effective kinetics at the pulse scale, that is for averaged concentrations over the solute pulse, we study the time evolution of the average concentration $\overline{c}(t)$ and the evolution of the effective reaction rate as a function of the average concentration.

We compare these numerical simulations to analytical solutions that we derived using the approximation discussed in the following section. Furthermore, we test these analytical predictions for one geochemically relevant example using the multi-component reactive transport model, CrunchFlow (version 1.0). Boundary and initial conditions for these simulations are described in the corresponding section. As for Matlab simulations, we use a domain large enough to ensure that the pulse does not reach the boundary and a grid discretization small enough to ensure convergence of the results.

2.5 Gaussian approximation for analytical derivations

When reactions are described by nonlinear local kinetics, transport and reaction interact in complex ways. Reaction impacts local concentration gradients, which in turn affect diffusive fluxes. The latter leads to changes in the spatial concentration profile, which affects reaction. These interactions are captured by the diffusion-reaction equation (11). In order to better understand the interplay between reaction dynamics and dilution, and how it leads to different average kinetics compared to a well-mixed batch reactor, we develop an approximate analytical description of the average concentration, for a range of Damköhler numbers Da and reaction orders β.

In non-dimensional units, the initial condition is a rectangular pulse of unit finite width, identical with the batch conditions. Before diffusion has time to deform the pulse substantially, which is the case for times much smaller than the characteristic diffusion time τ_D, we expect

the dynamics to be well-approximated by the batch kinetics, so that the average concentration approximately follows Eq. (8). This corresponds to $t \ll \mathrm{Da}$ in nondimensional terms. For non-dimensional times $t \gtrsim \mathrm{Da}$, diffusion has appreciably deformed the initial pulse. To derive analytical solutions for this problem, we approximate the reactive solute profiles as Gaussian distributions. This approximation is expected to be highly accurate for low Da when diffusion is faster at modifying the concentration distribution than reaction. It turns out to be also accurate in intermediate and high Da ranges (Appendix C), which facilitates an analytical solutions for the effective kinetics. The concentration distribution of reactive pulses is thus approximated as,

$$c(x,t) = \frac{M(t)}{\sqrt{2\pi\sigma^2(t)}} e^{-\frac{x^2}{2\sigma^2(t)}}, \tag{13}$$

where the variance $\sigma^2(t)$ and mass $M(t)$ evolve in time as a function of diffusion and reaction. Note that in the absence of reaction, the solution corresponds to $M(t) = 1$, and $\sigma^2(t) \propto t/\mathrm{Da}$.

Inserting Eq. (13) into Eq. (12), we obtain,

$$\frac{d}{dt}M(t) = -\frac{M(t)^\beta}{\sqrt{\beta}}[2\pi\sigma^2(t)]^{\frac{1-\beta}{2}}. \tag{14}$$

The Gaussian assumption allows second spatial derivatives in Eq. (11) to be estimated as,

$$\frac{\partial^2 c}{\partial x^2} = \left(-\frac{1}{\sigma^2} + \frac{x^2}{\sigma^4}\right) c, \tag{15}$$

hence, at $x = 0$, we have for the maximum concentration,

$$c(0,t) = \frac{M(t)}{\sqrt{2\pi\sigma^2(t)}}, \tag{16}$$

and for the second spatial derivative,

$$\frac{\partial^2 c}{\partial x^2}\Big|_{x=0} = -\frac{M(t)}{\sqrt{2\pi}\sigma(t)^3}. \tag{17}$$

Inserting Eq. (16) and (17) in Eq. (11) at $x = 0$, we obtain

$$\frac{d}{dt}\frac{M(t)}{\sqrt{2\pi\sigma^2(t)}} = -\frac{M(t)}{2\mathrm{Da}\sqrt{2\pi}\sigma(t)^3} - \frac{M(t)^\beta}{(2\pi)^{\beta/2}\sigma(t)^\beta}. \tag{18}$$

As discussed in Appendix B, Eq. (14) and (18) provide two independent equations to solve for the two unknowns $M(t)$ and $\sigma(t)$. Since the average concentration is proportional to the total mass (equation (4)), the dimensionless average concentration is equal to the dimensionless mass, $\overline{c(t)} = M(t)$. The accuracy of the Gaussian approximation is discussed in Appendix C.

3 Results

First, numerical simulations for the average concentration as a function of time for different values of β are presented for broad range of Damköhler numbers and reaction orders in order to demonstrate the resulting behavior and departure of the effective kinetics from the batch systems. As expected, for $\beta = 1$, the effective kinetics are equal to the batch kinetics (Fig. 2.b). For the other cases, the results can be generalized as:

- For$\beta < 1$, the average concentration of the pulse decreases faster than in the batch reactor, and the effective reaction rate of the pulse system is globally greater than the batch reactor (Fig. 2a).
- For $\beta > 1$, the average concentration of the pulse decreases more slowly than in the batch reactor and the effective reaction rate of the pulse injected system is globally less than the batch reactor (Fig. 2c-d).

Qualitatively, this effect may be understood as follows. For $\beta < 1$, the reaction is more efficient when distributing a given mass in the low concentration range because of the form of the kinetics (Eq. (1)). Dilution by diffusion accelerates the transfer of mass towards lower concentration values and thus enhances the average kinetics compared to the batch case.As a result, the time at which the average concentration goes to zero (Fig. 2.a) decreases with decreasing Da as dilution accelerates the effective kinetics. The opposite effect occurs for $\beta > 1$, leading to a reduction of the effective kinetics compared to batch kinetics. For the extreme case of $\beta > 3$, dilution retards the reaction to such a level that the average concentration converges asymptotically to a nonzero value (Fig. 2.d), with the asymptotic residual concentration increasing with decreasing Da.

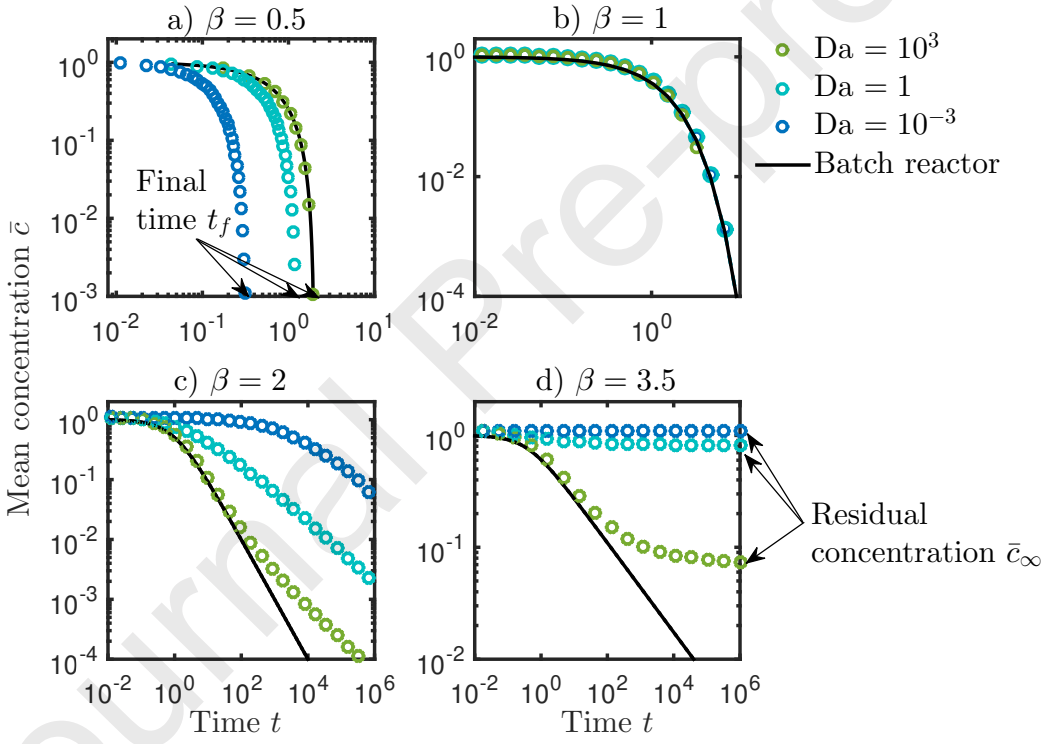

Figure 2: Average concentration in a reactive pulse as a function of time for a) $\beta = 0.5$, b) $\beta = 1$, c) $\beta = 2$ and d) $\beta = 3.5$. Numerical simulations for low, intermediate and high Da numbers (circles) are compared to batch kinetics (black solid line). The final time for full reactant consumption t_f, which occurs for $\beta < 1$, is indicated with arrows in figure a). The residual average concentration $\bar{c}_\infty$, which occurs for $\beta > 3$, is indicated with arrows in figure d). Note that the y-axis differs between panels to resolve the differences in concentration evolution.

The impact of dilution on reaction kinetics may be also understood by plotting the total reaction rate as a function of the average concentration (Fig. 3). For linear kinetics, the effective

kinetics are identical to the batch kinetics independent of Da (Fig. 3.b). For low Da and $\beta < 1$, the global reaction rates are always greater than the batch for a given average concentration (Fig. 3.a). For low Da and $\beta > 1$, the global reaction rates are always less than the batch for a given average concentration (Fig. 3.c and Fig. 3.d). The difference between effective reaction kinetics and batch kinetics can reach several orders of magnitude. At low Damköhler numbers (Blue dots in Fig. 3) and quasi-constant average concentration, the variation in the reaction rates is substantial (an increase for $\beta < 1$ and a decrease for $\beta > 1$) . This counterintuitive regime is due to the action of diffusion, which distributes mass towards low concentration values, such that while the total reaction rate varies, the overall rate is insufficient to affect the total mass. At high Damköhler numbers (Green dots in Fig. 4) the effective rate first follows a batch-like behavior and then departs towards effective kinetics that are a function on β. In the following, we present our analytical results for the effective kinetics as a function of β.

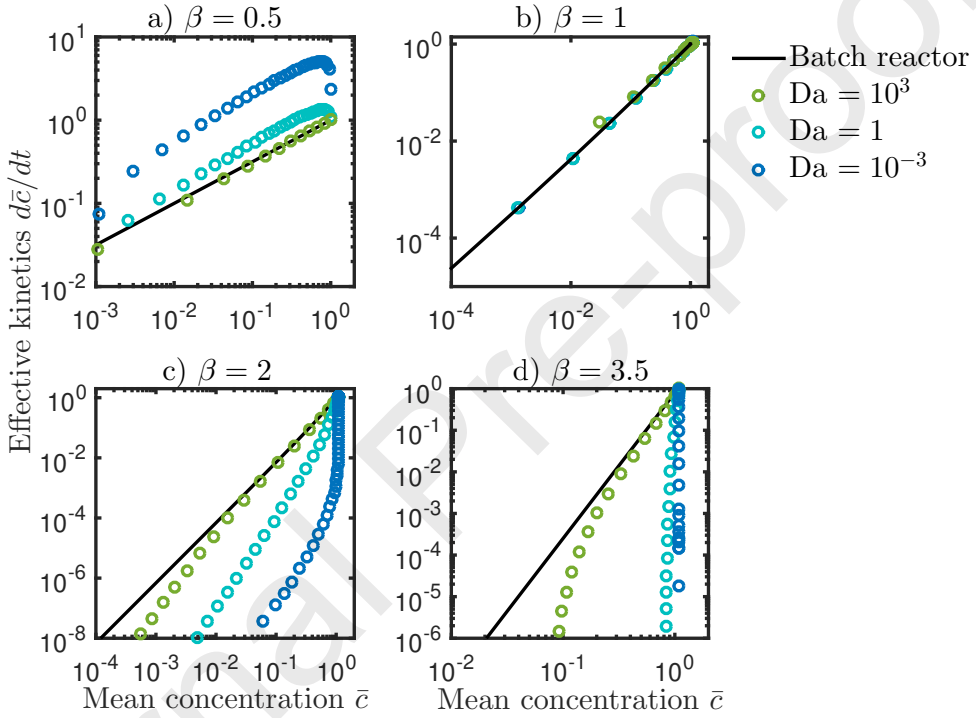

Figure 3: Effective kinetics of reactive pulses quantified as the rate of change of the mean concentration as a function of mean concentration for a) $\beta = 0.5$, b) $\beta = 1$, c) $\beta = 2$ and d) $\beta = 3.5$. Numerical simulations for low, intermediate and high Da numbers (circles) are compared to the batch reactor solution (black solid line). Note that the y-axis differs between panels to resolve the differences in concentration evolution.

3.1 Reaction order $\beta < 1$

For $\beta < 1$, the average concentration reaches zero at a finite time t_f (Fig. 4.a). For large Damköhler numbers, diffusion does not have time to induce significant dilution before $t = t_f$. Therefore, this time is identical to the time required to consume the full reactant mass in batch

reactions (Green dots and line in Fig. 4.a, Appendix B.2.1):

$$t_f = \frac{1}{1-\beta}, \text{ for } \mathrm{Da} > 1. \tag{19}$$

For low Damköhler numbers, using the assumption of a Gaussian concentration distribution, we obtain a solution for the evolution of the average concentration (Appendix B.1, Eq. (B.2)), in good agreement with numerical simulations (Blue dots and dashed lines in Fig. 4.a). This leads to the following estimate of t_f (Appendix B.1, Eq. (B.4)),

$$t_f \sim \mathrm{Da}^{\frac{1-\beta}{3-\beta}}, \text{ for } \mathrm{Da} < 1. \tag{20}$$

This scaling and the convergence to a constant value given by Eq. (19) at large Da are verified from numerical simulations in Fig. 4.b. The effect of dilution is thus to accelerate the effective kinetics, with a consumption time up to ten times less than predicted from the batch kinetics for $\mathrm{Da} = 10^{-3}$.

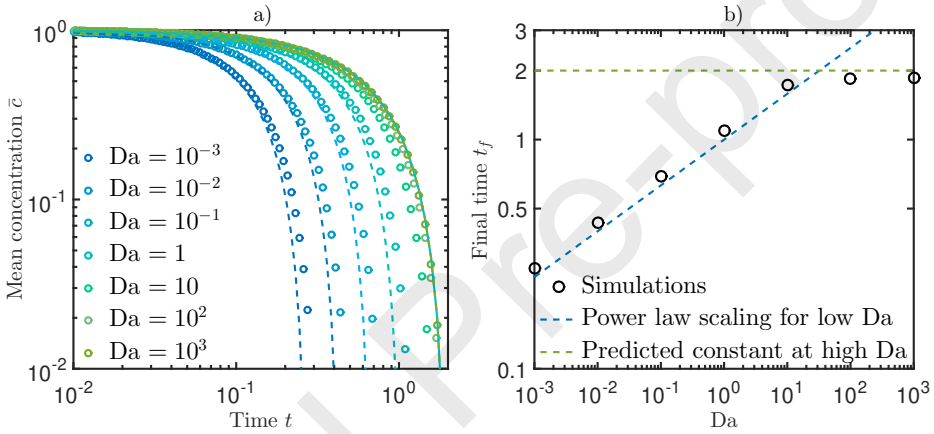

Figure 4: Effect of Damköhler on effective kinetics for $\beta = 0.5$, a) Average concentration as a function of time for several Damköhler numbers. Numerical results (dots) are compared to the analytical solutions of Eq. (B.2) (dashed lines). The batch solution is shown as a continuous line. b) Time t_f at which the mean concentration reaches zero as a function of Damköhler number. Black circles represents simulations, dashed lines represents the analytical predicions of Eq. (19) for low Damköhler numbers and Eq. (20) for high Damköhler number.

3.2 Reaction order $1 < \beta < 3$

For $1 < \beta < 3$, we predict that the departure from the batch kinetics is not only a difference in the magnitude of the reaction but also in its order. The latter is shown by the power law scaling that relates the average reaction rate to the average concentration (dashed lines in Fig. 5), with an exponent that differs from the batch reaction order. For low Damköhler numbers, our solution implies that the average concentration decays in time as a power law (Appendix B.1, Eq. (B.6)),

$$\bar{c}(t) \sim t^{-\frac{3-\beta}{2(\beta-1)}}, \tag{21}$$

and the effective rate r_M follows (Appendix B.1, Eq. (B.9))

$$\frac{d\bar{c}}{dt} \sim \bar{c}^{\tilde{\beta}}, \tag{22}$$

with the effective reaction order $\tilde{\beta}$,

$$\tilde{\beta} = \frac{1+\beta}{3-\beta}. \tag{23}$$

For high Damköhler numbers, two regimes occur (Fig. 8). The first regime, for $t < \mathrm{Da}$, follows the batch kinetics (Appendix B.2.1). In the second regime, for $t > \mathrm{Da}$, (Appendix B.2.2), the effective kinetics follow the same power law behavior as for low Damköhler number (Fig. 5.a) defined by Eq. (22).

These predictions are consistent with numerical simulations for all Damköhler numbers (Fig. 5.a) and all local reaction order β (Fig. 5.b). For low to intermediate Damköhler numbers, the effective kinetics follow the predicted power law kinetics, characterized by the effective reaction order $\tilde{\beta}$ for the full range of concentrations (Fig. 5.b). For large Damköhler numbers (green dots in Fig. 5.a) the effective kientic shows two regimes: a first regime following the batch kinetics given by Eq. (1) and a second power law regime given by Eq. (22). The difference between the effective and local reaction orders is largest for large reaction orders (Fig. 6). For $\beta = 1.5$, the effective order $\tilde{\beta} = 1.7$ is relatively close to the batch reaction order. Above $\beta = 1.5$, the effective order increases rapidly and is equal to $\tilde{\beta} = 3$ for $\beta = 2$. As β tends to 3, the deviation between the effective reaction order and the batch reaction order can become very large as the effective reaction order tends to infinity (Fig. 6).

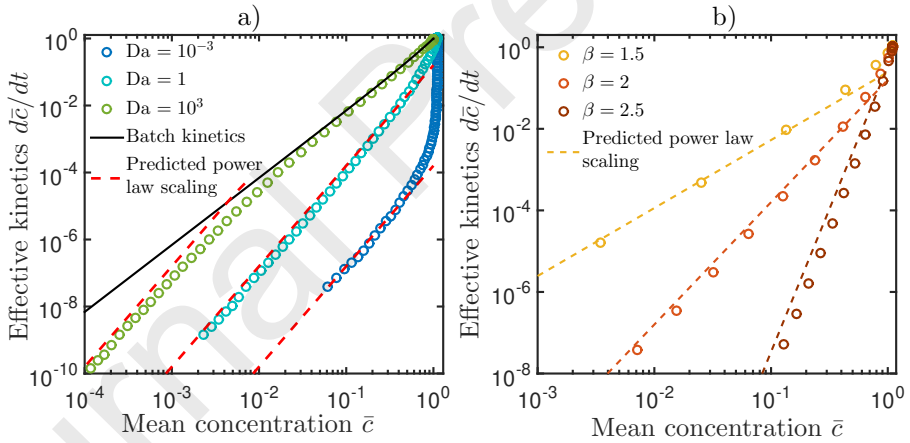

Figure 5: Effective kinetics in terms of mean concentration, a) $\beta = 2$, for Low, intermediate and high Da numbers, b) $\mathrm{Da} = 1$ for different β in the range $1 < \beta < 3$. Numerical results (dots) are compared to analytical solutions (dashed lines). The power law behavior predicted by Eq. (22) is shown as a dashed line.

3.3 Reaction order $\beta \geqslant 3$

For $\beta \geqslant 3$, the pulse reaction is much less efficient compared to a batch reactor, in the sense that the average reaction rate is smaller than in batch conditions for a given average concentration. For $\beta > 3$, dilution slows down the reaction so that the average concentration does not reach zero

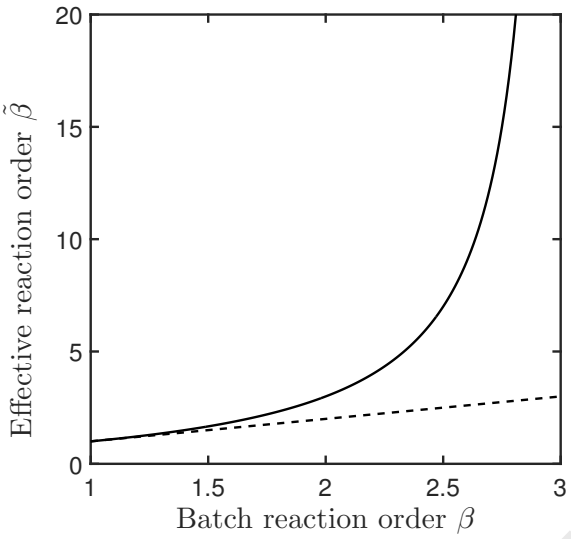

Figure 6: Effective reaction order $\tilde{\beta}$ predicted by Eq. (23) as a function of the batch reaction order for $1 < \beta < 3$ (solid line). The dashed line represents $\tilde{\beta} = \beta$.

but converges to an asymptotic minimum value $\bar{c}_\infty$ (Fig. 7). For $\beta = 3$, the average concentration decays to zero logarithmically as $t \to \infty$ (Appendix B.1, Eq. (B.3)). Note that this behavior differs fundamentally from the lower reaction orders discussed above, for which the reaction rate is always larger than zero and there is no residual concentration, except for $\mathrm{Da} = 0$.

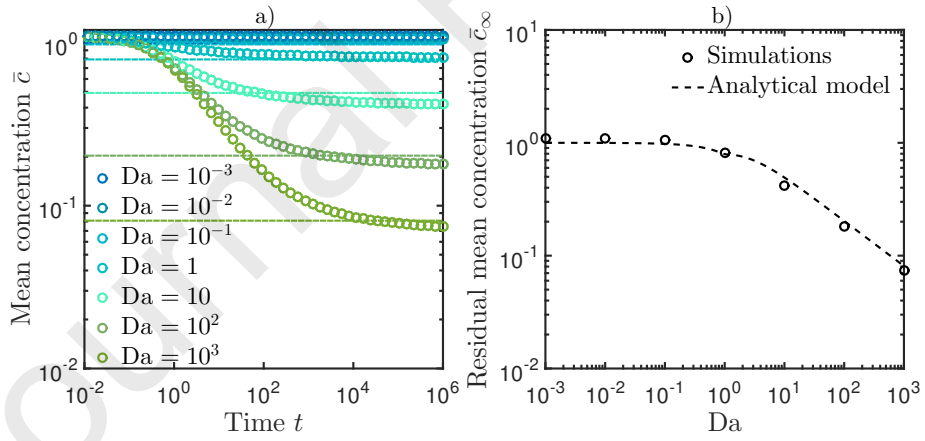

Figure 7: Effect of Damköhler on effective kinetics for $\beta = 3.5$, a) Numerical simulations (circles) as a function of time for different Damköhler number. Analytical model predictions for the asymptotic residual concentration are shown as dashed lines. b) Asymptotic residual mean concentration as a function of Damköhler number. Black circles represents simulations, the dashed black line represents the analytical model corresponding to Eq. (B.5) in Appendix B for low Damköhler numbers and to Eq. (25) for high Damköhler numbers.

For low Damköhler numbers, the solution for the evolution of the mean concentration (Appendix B.1, Eq. (B.2)) leads for $\beta > 3$ to an asymptotic value $\overline{c}_\infty$ such that (Eq. (B.5))

$$1 - \overline{c}_\infty \sim \mathrm{Da}. \tag{24}$$

As Da tends to zero, the asymptotic residual mean concentration tends to one (Fig. 7), which highlights the inhibiting effect of dilution on mass evolution for $\beta > 3$.

For high Damköhler numbers, the asymptotic residual mean concentration occurs in the second regime, leading to an asymptotic minimum value (Appendix B.2.2, Eq. (B.21))

$$\overline{c}_\infty \sim \mathrm{Da}^{-\frac{1}{\beta-1}}, \tag{25}$$

which again quantifies the inhibiting effect of dilution on reaction as Da increases. These analytical results closely match numerical simulations (Fig. 7.b).

4 Discussion

Our findings demonstrate that chemical gradients alter effective reactive kinetics through the coupling of diffusion and nonlinear reactions. By investigating the evolution of reactive solute pulses, as a paradigm for chemical gradients that evolve over space and time, we have uncovered a diverse spectrum of effective kinetic dynamics that depend on (1) the reaction nonlinearity (reaction order β) and (2) the relative importance of reaction and dilution quantified by the Damköhler number Da. A central conclusion of our study is that dynamic chemical gradients not only change the magnitude of the effective kinetic coefficient but also change the nature of the non-linearity compared to the local kinetics. This result is in contrast with previous studies that have studied how diffusive limitation, physical and geochemical heterogeneities (e.g. Soulaine et al., 2017; Wen and Li, 2017b; Deng et al., 2018), alter the effective kinetic coefficients, while keeping the same effective kinetic laws as the local kinetics. While we have focused on simplified reaction kinetics to quantify and formalize this mechanism, these dynamics are expected to impact a large range of geochemical systems where they are coupled to other processes. In the following, we discuss the relevance to common classes of biogeochemical reactions based on a synthesis of the results discussed above. Subsequently, we provide an example for a mineral dissolution reactions where rate discrepancies are commonly observed. However, the approach is also applicable to other types of reactions, including redox, precipitation, complexation and adsorption reactions, as discussed in the following section.

4.1 Characteristic persistence time of reactive pulses

To illustrate the consequences of the derived effective kinetics across a broad range of β and Da, we calculate the persistence time of reactive pulses that quantifies a characteristic time for the decay of the pulse mass under the effect of reaction. We define this time as a the time required for the pulse mass to reach a given fraction of the initial mass. To compare with the batch reactor, we divide it by the time it would take for a batch reactor to reach the same fraction of the initial mass. This normalized persistence time t_c is shown in Fig. 8 as a function of β and Da. We have taken here the fraction of the initial mass to calculate this time to be equal to 1%. Qualitatively similar results are obtained for other fractions. We have considered the full range of Damköhler numbers, from $\mathrm{Da} = 10^{-3}$ (fast dilution compared to reaction) to $\mathrm{Da} = 10^{3}$ (fast reaction compared to dilution). This covers a range of characteristic reaction times, that vary broadly depending on the type of reaction, and of transport time scales, which depend on the pulse size and species diffusion coefficient (Eq. (9)).

On the left-hand side of Fig. 8, for $\beta < 1$, reactants disappear on the order of ten times faster than in the batch in the low Damköhler range, which is consistent with the analytical estimate of t_f (Fig. 4). For $1 < \beta < 3$, the characteristic persistence time increases sharply with the non-linear reaction order β, reaching several orders of magnitude increase. This is due to the emergence of effective reaction orders $\tilde{\beta}$ that become much larger than the batch reaction order for increasing β (Fig. 6). Within the grey zone, for $\beta > 3$, residual mass persists indefinitely and the characteristic persistence time tends to infinity. Collectively, these findings imply that when concentration fields are heterogeneous the commonly used approach of coupling residence time to batch kinetics may underestimate/overestimate the persistence of reactants by orders of magnitude. Our main analytical findings in the different quadrants of Fig. 8 provide a framework for assessing the impact of concentration gradients on effective kinetics for a given type of reaction, as discussed below.

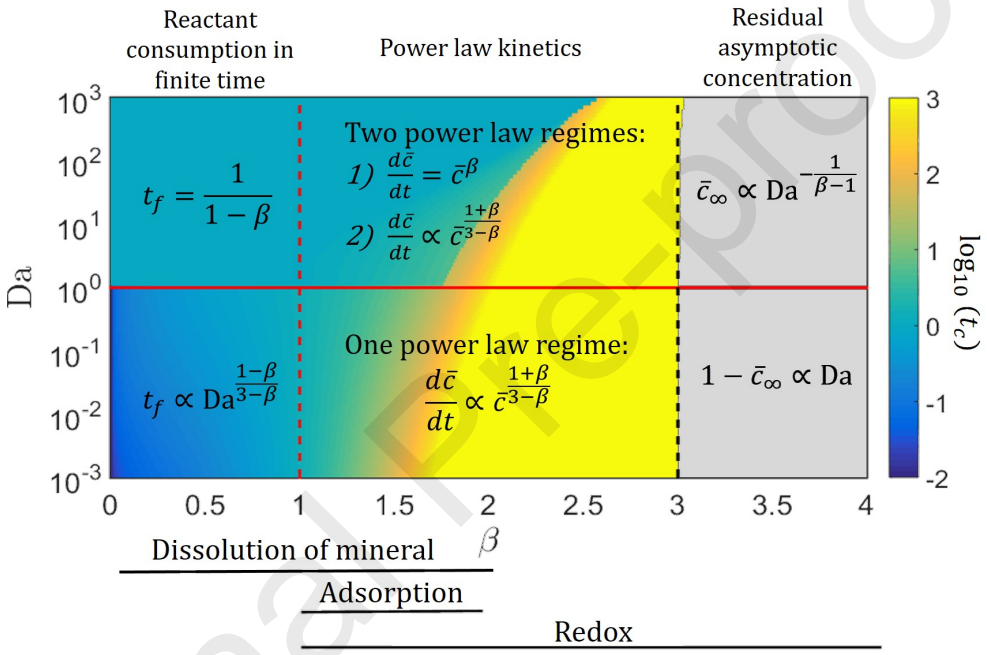

Figure 8: (Da, β) phase diagram of characteristic persistence time t_c and synthesis of main analytical results. The solid red line represents Da = 1. The dashed red and black lines correspond respectively to $\beta = 1$ and $\beta = 3$. The color scale represents the time t_c needed for the mean concentration to reach 1% of initial mean concentration for the reactive pulses, normalized by the same time for the batch reactor. The main reaction enhancement occurs for $\beta < 1$ and Da < 1 (blue area) while the effective reaction rate is strongly slowed down for $\beta > 1.5$ (yellow area). For $\beta > 3$, residual mass persists indefinitely and the characteristic persistence time may never be reached if the residual mass is larger than 1% (grey area). The typical range of effective reaction orders β for mineral dissolution, adsorption and redox reactions are indicated at the bottom.

4.2 Geochemical relevance of effective kinetics

Our results are strictly valid when the concentration of one element is spatially variable and the others are in excess in the fluid or in the mineral phase. This simplification isolates and

formalizes the impact of transient concentration gradients on upscaled kinetics. In complex multi-component reactive system, this effect will act together with other known mechanisms, such as geochemical and physical heterogeneities, as well as multiple reactions. Although other processes will also contribute to the effective kinetics, we argue that the new phenomena described here will likely have a major contribution as it can alter reaction rates over orders of magnitude and modify the effective orders of reaction. For single step reactions, the reaction order β with respect to a given chemical species is equal to its stoichiometric coefficient. However, most biogeochemical reactions are complex multi-step reactions such that the rate-limiting step is unknown and hence most reaction orders are determined empirically and may range from 0 to 5.

The lower left hand side of Fig. 8 would be typical of silicate mineral dissolution where reactions involve multiple steps that can be effectively described by an adaptation of transition state theory (Aagaard and Helgeson, 1982; Lasaga et al., 1994; Steefel and Lasaga, 1994):

$$r = k \prod_{i=1}^{N} a_i^n \left(1 - \frac{Q}{K_{eq}}\right)^m, \tag{26}$$

where r is the overall rate, k is the intrinsic kinetic constant, a_i the ion activity, N the number of species, Q the ion activity product for the mineral-water reaction, and K_{eq} the corresponding equilibrium constant. The empirical exponents n and m introduce a non-linearity of the reaction rate with respect to the species concentration (Hellmann and Tisserand, 2006). Far from equilibrium, $Q \gg K_{eq}$ or $Q \ll K_{eq}$, and when a single species is limiting, equation (26) can be written as the simplified non-linear kinetics that we consider (equation (1)), with $\beta = n$. Effective reaction orders estimated from laboratory experiments and typically range from $\beta = 0.1$ to 2 (Plummer and Wigley, 1976; Palandri and Kharaka, 2004). Such mineral dissolution reactions are typically slow and therefore correspond to the low Da range. The upper right-hand sider region of Fig. 8 may be typical of redox reactios. Metal redox reactions are typically characterized by $1 \leqslant \beta \leqslant 4$, while other redox reactions tend to have lower orders $1 \leqslant \beta \leqslant 2$ (Bethke, 1996). Redox reactions involving organic matter may have orders as high as $\beta = 5$ (Bleam, 2017). In the middle region of Fig. 8, where t_c transitions rapidly, adsorption kinetics may be particularly susceptible to the effects observed here. Adsorption reaction kinetics are generally modelled with first-order or pseudo-second-order kinetics (Rudzinski and Plazinski, 2006; Wu et al., 2009; Robati, 2013; Moussout et al., 2018), which correspond to $\beta = 1$ or $\beta = 2$, but higher reaction orders are also observed (Largitte and Pasquier, 2016).

The first application of our findings is for understanding the behavior of reactive solutes in field systems (Fig. 9a). As illustrated in Fig. 1, concentration gradients in natural systems can be driven by a diverse set of processes, ranging from intermittent sources to physical heterogeneity. For a given transport time, the reaction efficiency may be much faster (for $\beta < 1$) and much slower (for $\beta > 1$) than anticipated from batch kinetics (Fig. 8). This could lead to a much deeper penetration of reactive pulses or to a much faster consumption of solutes. A second application is reactive transport modelling; to capture the effect of concentration gradients on reaction kinetics, reactive transport models should have a spatial resolution finer than the smallest scale of concentration gradients (Fig. 9b). This is not possible for catchment scale applications (e.g. Li et al., 2017) but it is also challenging for modeling column experiments because chemical gradients often persist at the microscale (Heyman et al., 2020). Hence, our findings may help defining effective kinetics that quantify the impact of subscale gradients in reactive transport models. A third application is the interpretation of biogeochemical kinetics measured in experimental systems that are not well mixed, i.e. where chemical gradients persist (Fig. 9c). Geochemical reactions occurring at high temperatures and pressures, such as those associated with geologic carbon storage (e.g. DePaolo and Cole, 2013; Jun et al., 2013; Beckingham et al.,

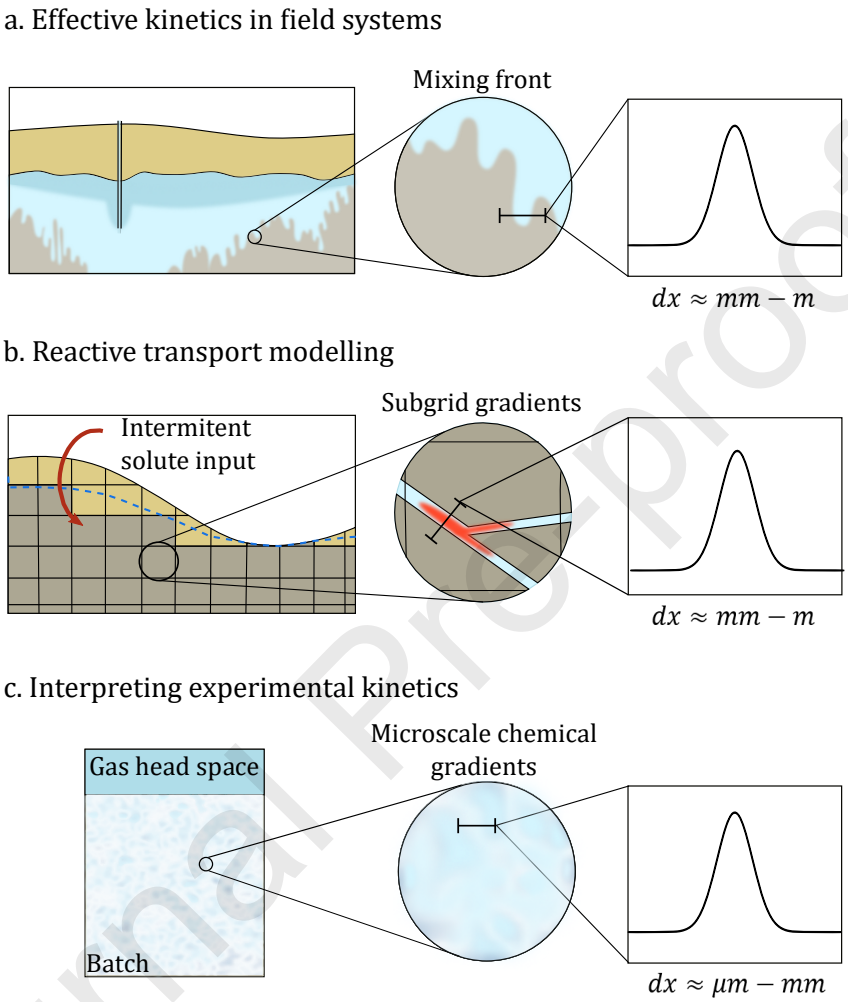

Figure 9: Illustration of different applications where unresolved chemical gradients may alter effective kinetics. a. Effective kinetics in field systems, such as CO_2 injection in the subsurface, where reactive pulses develop in mixing fronts. b. Reactive transport modeling, where subgrid chemical gradients cannot be resolved in models. c. Interpreting experimental kinetics in unmixed batches, where microscale chemical gradients can affect measured kinetics. The typical scales of expected chemical gradients for these applications is indicated as dx. textcolorblueUpdate the order of subfigures to match new order of section 5.

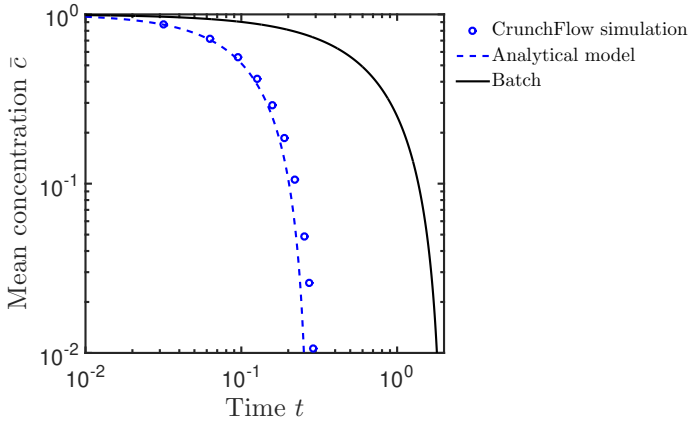

Figure 10: Simulation of pyrite dissolution by a pulse of dissolved oxygen for Da $= 10^{-3}$ ($\beta = 0.5$). Normalized mean concentration is shown as a function of normalized time, following the same definition as above. Results of the CrunchFlow simulation are shown as dots, the analytical model as a dashed line (Eq. B.2) and the batch model as a continuous line (Eq. B.11).

2016; Beckingham et al., 2017), are often studied using batch reactors, where a gas headspace of a constant volume is used to maintain a constant pressure (Giammar et al., 2005; Johnson et al., 2014). Depending on the experimental conditions, pressure vessels can be difficult to mix via rocking or internal stirring, and are often static. Hence, in the absence of mechanical mixing, chemical gradients of different origin may develop, including dissolved gas convection, transport limitations and spatially heterogeneous reaction rates.

4.3 Example of the oxidation of pyrite by a pulse of dissolved oxygen

To illustrate these effective kinetics for a specific geochemical system, we take the example of pyrite dissolution by a pulse of dissolved oxygen. The aqueous oxidation of pyrite by oxygen is an example of geochemical process studied with reactive transport models to address a range of problems, including aquifer storage and recovery (Lazareva et al., 2015), acid mine drainage (Hubbard et al., 2009), and radioactive waste migration (Malmström et al., 2000; Yang et al., 2007). Intermittent release of dissolved oxygen, due to rainfall events or river stage variations (Fig. 1.a and 1.b), or flow heterogeneities (Fig. 1.e) often lead to small-scale dissolved oxygen gradients (Xu et al., 2000; Bochet et al., 2020) that are typically not resolved by reactive transport models. The reaction of oxidation of pyrite by oxygen can be written as,

$$\mathrm{FeS_2} + \tfrac{7}{2}\,\mathrm{O_2} + \mathrm{H_2O} \longrightarrow \mathrm{Fe^{2+}} + 2\,\mathrm{SO_4^{2-}} + 2\,\mathrm{H^+}$$

Assuming that the other species are in excess, the kinetic rate law for pyrite oxidation by oxygen may be written with respect to oxygen as (McKibben and Barnes, 1986)

$$\frac{1}{3.5}\frac{dc_{O_2}}{dt} \approx -k c_{O_2}^{0.5}, \tag{27}$$

corresponding to $\beta = 0.5$.

For the geochemical system considered here, the kinetics of subscale unresolved oxygen pulses would be faster than predicted by batch kinetics (Fig. 8). For instance, assuming a Damköhler number of 10^{-4}, resulting from a kinetic rate constant of 6.6×10^{-9} mol/m^2/s (Yang et al., 2007) and a diffusion coefficient of 10^{-9} mol/m^2/s (Jung and Navarre-Sitchler, 2018a), dissolved

Table 1: Initial and injection chemistry used in CrunchFlow simulations for a single pulse, pyrite dissolution

Species	Initial condition (mol/L)	Injection condition (mol/L)
Fe^{2+}	10^{-8}	10^{-8}
H^+	10^{-4}	10^{-4}
$O_{2,aq}$	10^{-11}	10^{-4}
SO_4^{2-}	10^{-8}	10^{-8}
Cl^-	Equilibrates charge	Equilibrates charge

oxygen would be consumed 10 times faster than it would be in the well-mixed homogeneous system. The more rapid release of both Fe^{2+} and trace metals typically associated with pyrite (i.e., As, Pb, etc.) may have further implications for water quality. Although our results imply that kinetic rates used in reactive transport models of systems with sub-grid scale concentrations will be subject to additional uncertainty, our approach provides a concrete means of evaluating the range of kinetic parameters to enable robust sensitivity analysis or uncertainty quantification (e.g. Fenwick et al., 2014; Song et al., 2015).

We have verified that this geochemical system can be accurately modeled by our framework under the considered assumptions (Fig. 10) using the multi-component reactive transport model CrunchFlow (Steefel et al., 2015). We first consider the case of a single pulse. The system is composed of pyrite with a porosity of 30% and dissolution kinetic constant $k = 10^{-8.31}$ m mol^{-1} s^{-1} (Yang et al., 2007). The considered solute species are $O_{2,aq}$, Fe^{2+}, SO_4^{2-}, and H^+. For the initial condition in the domain prior to injection, the species concentrations are $c_{O_2} = 10^{-11}$ mol/L, $c_{Fe^{2+}} = 10^{-8}$ mol/L, $c_{SO_4^{2-}} = 10^{-8}$ mol/L, and pH is 4. Chloride is designated as the charge balancing ion to maintain electroneutrality. In the injected pulse, concentrations are the same as in the domain except for the oxygen concentration is set as $c_0 = 10^{-4}$ mol/L (Bochet et al., 2020, Table 1). The simulations were performed at 25°C with a diffusion coefficient of 10^{-7} m^2 s^{-1} (Elberling et al., 1994), leading to Da $= 10^{-3}$ (Table 2). The CrunchFlow simulation is in good agreement with the analytical model (Fig. 10). As predicted, the average concentration reaches zero much faster than the batch.

In order to evaluate the effect of a non-ideal concentration profile, we performed a CrunchFlow simulation with five irregularly spaced pulse injections of width 10^{-2} m each, with different initial oxygen concentrations ($log(c_{O_2}) = -4, -5, -6, -7, -8$) (Table 2). The initial conditions are the same as in the single pulse case (Table 1) and all the injected concentrations except oxygen are the same as in the background domain. The equivalent batch is defined with initial concentration equal to the mean of the pulse initial concentrations. The parameters are adapted to the single-pulse analytical model with an equivalent pulse width equal to the sum of the pulse widths, and an equivalent initial concentration set as the mean of injection concentrations, resulting in Da$= 5\ 10^{-2}$ (Table 2). In this case, the match with the analytical prediction remains excellent (Fig. 11) even though the concentration distribution is more complex than assumed in the analytical derivations.

Table 2: Parameters of the analytical model for the pyrite dissolution case.

Parameter	w_0	D	c_0	ν	k	A	Φ	τ_D	τ_R	Da
Unit	m	m^2/s	mol/L	[–]	[unit]	m^2/m^3	[–]	[–]	[–]	[–]
Single pulse	10^{-2}	10^{-7} [a]	10^{-4} [b]	3.5	$4.8\ 10^{-9}$ [c]	350	0.3	$1.6\ 10^{-5}$	$1.6\ 10^{-2}$	10^{-3}
$\beta = 0.5$										
Several pulses	10^{-2}	10^{-7}	10^{-4}	3.5	$4.8\ 10^{-9}$	350	0.3	$4\ 10^{-4}$	$7.5\ 10^{-3}$	$5\ 10^{-2}$
$\beta = 0.5$			10^{-5}							
			10^{-6}							
			10^{-7}							
			10^{-8}							

[a] (Elberling et al., 1994)
[b] (Bochet et al., 2020)
[c] (Yang et al., 2007)

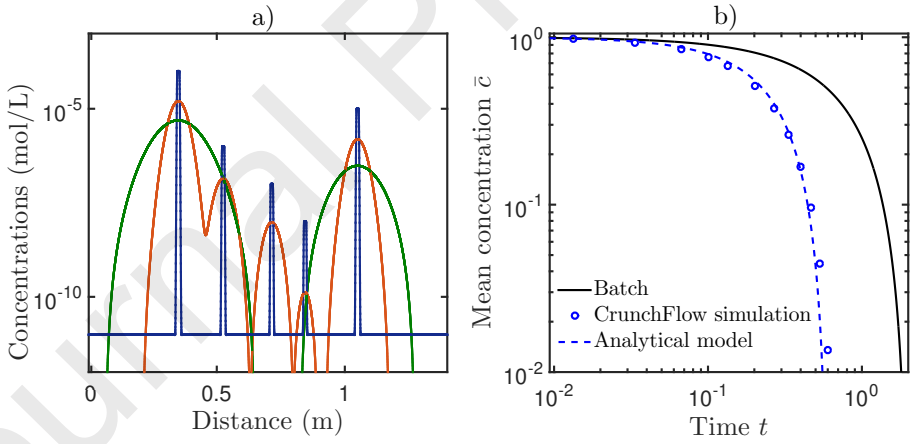

Figure 11: Simulation of pyrite dissolution by multiple pulses of dissolved oxygen ($\beta = 0.5$). Five pulses with different initial concentrations and irregularly spaced are injected in the domain. a) is the concentration profile in space at normalized time $t \approx 10^{-5}$ (blue), $t \approx 10^{-2}$ (orange), $t \approx 10^{-1}$ (green). b) the normalized mean concentration as a function of normalized time for the CrunchFlow simulation (dots), an equivalent batch system (with initial concentration equal to the mean of injected concentrations Eq. (B.11), continuous line), and an equivalent analytical model (considering one pulse with initial concentration equal to the mean of injected concentrations, Eq. (B.2), dashed line), thus corresponding to Da $= 5\ 10^{-2}$.

5 Conclusions

The effective kinetics of reactive pulses reveal a rich diversity of behaviors driven by the interplay between dilution and non-linear reaction (Fig. 8). In the presence of concentration gradients, diffusion acts to redistribute mass towards lower concentrations, which, when coupled with non-linear reactions, can either enhance or inhibit the reaction efficiency depending on the local reaction order. We have derived approximate analytical solutions that capture these reactive dynamics and predict the different effective kinetic laws as a function of Damköhler number and the reaction order, which are representative of a range of reactive transport systems (Fig. 1, 8 and 9). An important consequence of our results is the emergence of new effective kinetic laws characterized by upscaled orders that can be very different from those of the local kinetics. The coupling of transient concentration gradients and non-linear reactions hence leads to effective kinetics that can be much more non-linear than the batch kinetics (Fig. 6).

To isolate this mechanism and derive approximate analytical solutions for the effective kinetics, we considered here the idealized case of reactive pulses evolving through diffusion and reaction. In complex natural reaction networks, this effect acts together with a range of other processes and therefore it is difficult to understand and quantify. Other important phenomenon known to impact the effective kinetics include the limited access of solutes to reactive surfaces and mixing limitations, due to physical and geochemical heterogeneity at the pore or Darcy scale (Molins et al., 2014; Beckingham et al., 2017; Wen and Li, 2018; Jung and Navarre-Sitchler, 2018a; Valocchi et al., 2019). In multi-components systems, our results are strictly valid when one element is varying in space and time and the others are in excess. In natural systems several elements may be spatially variable and react with different orders leading to more complex behaviour. However, since the effect that we have uncovered leads to orders of magnitude differences between batch and effective reaction rates, it is likely playing a major, and so far unappreciated, role in multi-component systems.

Although we explicitly solve the system for the ideal case of pulses, our general findings are expected to apply qualitatively to different types of concentration landscapes. Indeed, in the presence of concentration inhomogeneities, induced by intermittent reactant release or physical heterogeneity (Fig. 1), diffusion tends to redistribute mass towards lower concentrations, which leads to reaction enhancement or inhibition depending on the local reaction order β as described here. The derived analytical framework is an essential step to integrate a range of biogeochemical reactions in new mixing theories that describe the statistics of concentration gradients (Le Borgne et al., 2017). The lamella mixing theory was successfully used to predict the upscaled kinetics of mixing-driven reactions at pore scale (De Anna et al., 2014b) and Darcy scale (Le Borgne et al., 2014; Bandopadhyay et al., 2018) by coupling the one-dimensional compression-diffusion equation transverse to stretched solute lamellae with bi-molecular reactions in the fluid phase. By solving explicitly the coupling of diffusion and non-linear reactions, the method presented here resolves the main difficulty for the development of a reactive lamella framework to upscale the effective kinetics of a range of non-linear reactions under incomplete mixing conditions, including fluid-solid reactions.

These findings would thus be useful to interpret the result of reactive experiments in which subscale chemical gradients develop due to poor mixing. These analytical results may also be used to guide reactive transport models that cannot fully resolve the scale of concentration gradients, which occurs in many reactive transport problems. Finally, they provide a new framework to understand the effect of concentration gradients on chemical reactions in field applications, in particular to understand the possible longer/smaller persistent time or penetration length of reactive solutes. These findings indeed suggest that the characteristic persistence time of biogeochemical pulses can differ by orders of magnitude from the predictions of models that

couple solute residence time with batch kinetics. Reactive pulses are consumed much faster when the order of the reaction is less than one, whereas they persist for a much longer time when the order of the reaction is larger than one. These effects are particularly important at low Damköhler number i.e., for reactions that are slow compared to the characteristic diffusion time. For orders of reaction larger than three, dilution slows down reaction to the point that a residual mass persists asymptotically.

Acknowledgments

CLT and TLB gratefully acknowledge funding by the ERC under the project *ReactiveFronts* 648377. CLT would like to thank also l'Ecole des Docteurs de l'UBL, le Conseil Regional de Bretagne and OZCAR-RI for supporting this work. TA is supported by a Marie Skłodowska Curie Individual Fellowship, under the project *ChemicalWalks* 792041. CB acknowledges funding from Region Bretagne and Rennes Metropole.

Appendix A Notations

We detail all notations used in the study in table 3.

Appendix B Analytical solutions

This appendix details the analytical derivations for effective kinetics under coupled diffusion and non-linear reactions based on the assumption of Gaussian distribution of the reactant (Eq. (13)) for $t \gg \mathrm{Da}$ and of negligible diffusion for $t \ll \mathrm{Da}$. The validity of these assumptions is discussed in Appendix C. The cases of low and high Damköhler are detailed separately below.

B.1 Low Damköhler number

In the limit of low Da, diffusion quickly deforms the pulse into a Gaussian distribution (Eq. (13)), whose variance evolves diffusively (see Appendix C and Fig. C.3),

$$\sigma^2(t) \approx \frac{t + \mathrm{Da}/12}{\mathrm{Da}}, \tag{B.1}$$

where we have set $\sigma^2(0) = 1/12$ to match the variance of the initial rectangular profile. Inserting Eq. (B.1) into (14), we obtain

$$M(t) = \left[M_i - \frac{2}{\sqrt{\beta}} \frac{1-\beta}{3-\beta} \left(\frac{2\pi}{\mathrm{Da}} \right)^{\frac{1-\beta}{2}} \left[(t+\mathrm{Da})^{\frac{3-\beta}{2}} - \mathrm{Da}^{\frac{3-\beta}{2}} \right] \right]^{\frac{1}{1-\beta}}, \tag{B.2}$$

with the initial mass $M_i \approx M(0) = 1$. Note that for $\beta = 1, 3$ this solution is singular and is not valid. For linear kinetics, $\beta = 1$, the concentration profile is exactly Gaussian, and the total mass decays exponentially. For $\beta = 3$, combining Eq. (14) and Eq. (B.1), and carrying out the integration explicitly, we obtain

$$M_{\beta=3}(t) = \left[1 + \frac{\mathrm{Da}}{\sqrt{3\pi^2}} \log\left(1 + \frac{12t}{\mathrm{Da}} \right) \right]^{-1/2}, \tag{B.3}$$

Table 3: Definition of model parameters and units

Parameter	Definition	Units
r	Reaction rate	mol $L^{-\mathrm{d}}$ T^{-1}
c	Concentration	mol $L^{-\mathrm{d}}$
c_0	Initial concentration	mol $L^{-\mathrm{d}}$
$\overline{c}$	Mean concentration	mol $L^{-\mathrm{d}}$
$\overline{c}_\infty$	Normalized residual mean concentration, [−]	
β	non-linear power law exponent	[−]
$\tilde{\beta}$	Power law exponent of the effective kinetic	[−]
k	reaction rate constant	$\mathrm{mol}^{1-\beta} L^{\mathrm{d}(\beta-1)}$ T^{-1}
D	Diffusion coefficient	L^2 T^{-1}
Da	Damköhler number	[−]
L	Characteristic length	L
M	Mass	kg
S	Reference surface	L^2
w_0	Initial width	L
σ	Normalized variance	[−]
t	Time, normalized time	T, [−]
t_c	Normalized persistence time	[−]
t_f	Normalized final time, $\beta < 1$	[−]
τ_D	Diffusion characteristic time	T
τ_R	Reaction characteristic time	T
u	Fluid velocity	L T^{-1}
V	Volume of the batch	L^3
x	Distance	mol $L^{-\mathrm{d}}$ T^{-1}

which decays to zero logarithmically as $t \to \infty$.

Since the average concentration is proportional to the total mass (equation (4)), the dimensionless average concentration is equal to the dimensionless mass, $\overline{c(t)} = M(t)$. When $\beta < 1$, the mass reaches zero in a finite time according to Eq. (B.2), given to leading order in Da by

$$t_f = \left(\frac{\sqrt{\beta}}{2}\frac{3-\beta}{1-\beta}\right)^{\frac{2}{3-\beta}} \left(\frac{\mathrm{Da}}{2\pi}\right)^{\frac{1-\beta}{3-\beta}}. \tag{B.4}$$

For $\beta > 3$, the mass converges from above to an asymptotic minimum value according to Eq. (B.2). To leading order in Da, this gives,

$$\overline{c}_\infty = 1 - \frac{2\mathrm{Da}}{\sqrt{\beta}(\beta-3)(2\pi)^{\frac{\beta-1}{2}}}. \tag{B.5}$$

For $1 < \beta < 3$, Eq. (B.2) follows a power-law decay, which leads to the average concentration,

$$\overline{c}(t) \approx \sqrt{\frac{2\pi}{\mathrm{Da}}} \left(\frac{\sqrt{\beta}}{2}\frac{3-\beta}{\beta-1}\right)^{\frac{1}{\beta-1}} t^{-\frac{3-\beta}{2(\beta-1)}}, \tag{B.6}$$

for $t \gg \mathrm{Da}$.

Differentiating Eq. (B.6), we find

$$\frac{d}{dt}\overline{c}(t) = -\frac{3-\beta}{2(\beta-1)}\frac{\overline{c}(t)}{t}, \tag{B.7}$$

Because the average concentration decreases monotonically, $\overline{c}(t)$ is invertible, Solving Eq. (B.6) for time as a function of mean concentration, we have

$$t(\overline{c}) = \left(\frac{2\pi}{\mathrm{Da}}\right)^{\frac{\beta-1}{3-\beta}} \left(\frac{\sqrt{\beta}}{2}\frac{3-\beta}{\beta-1}\right)^{\frac{2}{3-\beta}} \overline{c}^{-\frac{2(\beta-1)}{3-\beta}}. \tag{B.8}$$

Thus, the effective kinetics are given by

$$\frac{d}{dt}\overline{c}(t) = \beta^{-\frac{1}{3-\beta}} \left(\frac{\mathrm{Da}}{\pi}\frac{\beta-1}{3-\beta}\right)^{\frac{\beta-1}{3-\beta}} \overline{c}^{\frac{1+\beta}{3-\beta}}. \tag{B.9}$$

B.2 High Damköhler number

We now develop an approximate description for the behavior of the average concentration at high Damköhler. This involves two different regimes.

B.2.1 First regime, $t \ll \mathrm{Da}$

First, for times $t \ll \mathrm{Da}$, diffusion has not had time to significantly deform the initial condition. Thus, the average concentration evolves approximately according to the batch dynamics,

$$\frac{d\overline{c}(t)}{dt} = -\overline{c}(t)^\beta, \tag{B.10}$$

and we obtain

$$\overline{c}(t) = [1 + (\beta-1)t]^{-\frac{1}{\beta-1}}. \tag{B.11}$$

For $\beta < 1$, the average concentration reaches zero during this regime at the time given by Eq. (19).

B.2.2 Second regime, $t \gg \mathrm{Da}$,

For $t > \mathrm{Da}$, the spreading of the pulse by diffusion cannot be neglected. Rearranging Eqs. (14) and (18), we obtain for the variance

$$\frac{d\log\sigma(t)}{dt} = \frac{1}{2\mathrm{Da}\sigma^2(t)} - (\sqrt{\beta}-1)\frac{d\log M(t)}{dt}. \tag{B.12}$$

If the first term on the right hand side of Eq. (B.12) dominates compared to the second term, the evolution of the variance is approximately diffusive. Otherwise, if the second term dominates, the evolution of the variance is driven by the effect of reaction. Inserting Eq. (B.11) into (B.12), the condition for diffusion-dominated growth is thus

$$\sigma(t)^{3-\beta}M(t)^{\beta-1} < \frac{\sqrt{\beta}-1}{\sqrt{\beta}}\frac{(2\pi)^{\frac{\beta-1}{2}}}{2\mathrm{Da}}. \tag{B.13}$$

We start by evaluating this inequality at $t = \mathrm{Da}$, which is the onset of this second regime. Since mass follows the batch dynamics in the first regime (Eq. (B.11)), at $t = \mathrm{Da}$, it is given by

$$M(\mathrm{Da}) = [1+(\beta-1)\mathrm{Da}]^{-\frac{1}{\beta-1}}. \tag{B.14}$$

We substitute Eq. (B.14) and $\sigma(\mathrm{Da}) = 1/12$ (corresponding to the initial variance of a rectangular pulse, assumed not to change appreciably up to $t = \mathrm{Da}$) in Eq. (B.13), which gives the condition for a dominant diffusive variance growth at $t = \mathrm{Da}$,

$$\frac{2\mathrm{Da}}{(2\pi)^{\frac{\beta-1}{2}}}\frac{\sqrt{\beta}-1}{\sqrt{\beta}}\frac{12^{-\frac{3-\beta}{2}}}{1+(\beta-1)\mathrm{Da}} < 1. \tag{B.15}$$

For a given β, the left hand side of Eq. (B.15) is largest for $\mathrm{Da}\to\infty$. Therefore, if the criterion holds in this limit, it holds for all Da. In this limit, the condition is

$$\frac{2}{\sqrt{\beta}(\sqrt{\beta}+1)(2\pi)^{\frac{\beta-1}{2}}12^{\frac{3-\beta}{2}}} < 1. \tag{B.16}$$

This holds for $\beta \lesssim 5$, as verified numerically. We focus on such β since higher β are not commonly encountered. Therefore, at $t = \mathrm{Da}$, the variance growth is dominated by diffusion for the range of β that we consider, leading to a variance equal to

$$\sigma^2(t) \approx \sigma^2(\mathrm{Da}) + \frac{t-\mathrm{Da}}{\mathrm{Da}}, \tag{B.17}$$

with $\sigma^2(\mathrm{Da}) = 1/12$, and a mass given by the same equation as for the low Da regime, with the initial mass $M_i \approx M(\mathrm{Da})$, see Eq. (B.2). To test whether the criterion of diffusion dominated variance holds true at larger times, we substitute Eq. (B.17) and Eq. (B.2) in Eq. (B.13). This gives the criterion

$$\frac{2\mathrm{Da}}{(2\pi)^{\frac{\beta-1}{2}}}\frac{\sqrt{\beta}-1}{\sqrt{\beta}}\frac{\left[\frac{1}{12}+\frac{t-\mathrm{Da}}{\mathrm{Da}}\right]^{\frac{3-\beta}{2}}}{M(\mathrm{Da}) - \frac{2}{\sqrt{\beta}}\frac{1-\beta}{3-\beta}\left(\frac{2\pi}{\mathrm{Da}}\right)^{\frac{1-\beta}{2}}\left[(t+\mathrm{Da})^{\frac{3-\beta}{2}} - \mathrm{Da}^{\frac{3-\beta}{2}}\right]} < 1. \tag{B.18}$$

It can be verified numerically that this criterion holds true at all times. For $t\to\infty$, this simplifies into

$$\frac{3-\beta}{\sqrt{\beta}+1} < 1, \tag{B.19}$$

which is always true for $\beta > 1$. Hence, the variance evolves diffusively at $t = \mathrm{Da}$ and at all later times, and a regime with reaction-dominated variance growth is never observed. The accuracy of the growth of the variance according to Eq. (B.17) is discussed in Appendix C.

The effective kinetics can thus be derived as follows for different β. For $1 < \beta < 3$, the effective kinetics remain given by Eq. (B.9), and the average concentration by Eq. (B.6) with $M_i = M(\mathrm{Da})$ (Eq. (B.14)). For $\beta > 3$, according to Eq. (B.11) after replacing the initial mass M_i by $M(\mathrm{Da})$, the mass tends to an asymptotic constant value given by

$$M_\infty = \left[M(\mathrm{Da}) + \mathrm{Da} \frac{2}{\sqrt{\beta}} \frac{\beta - 1}{\beta - 3} (2\pi)^{-\frac{\beta-1}{2}} \right]^{-\frac{1}{\beta-1}} . \tag{B.20}$$

At sufficiently large Da, we can neglect $M(\mathrm{Da})$ according to Eq. (B.14) because $\mathrm{Da}^{-\frac{1}{\beta-1}} \ll \mathrm{Da}$. Thus, we obtain the asymptotic value for the average concentration,

$$\bar{c}_\infty \approx \mathrm{Da}^{-\frac{1}{\beta-1}} \sqrt{2\pi} \left(\frac{\sqrt{\beta}}{2} \frac{\beta - 3}{\beta - 1} \right)^{\frac{1}{\beta-1}} . \tag{B.21}$$

Appendix C Hypothesis validation

In addition to the numerical validation of the analytical derivation for the effective kinetics, we further test the validity of the assumptions that we use in our analytical derivations. The Gaussian assumption and the variance growth assumptions are discussed separately below.

C.1 Gaussian assumption

Here we assess the validity of the Gaussian assumption for different Damköhler numbers at times corresponding to different regimes. As highlighted by Eq. (13), Gaussian distributions of different widths σ and maximum value c_{peak} collapse to a single curve when represented according to the normalized variables x/σ and c/c_{peak}. It is thus convenient to use this normalization to test the Gaussian assumption. Furthermore, Gaussian curves are uniquely characterized by the power law scaling

$$\log(c/c_{peak}) \sim (x/\sigma)^{-2} . \tag{C.1}$$

Therefore, Gaussian distributions are characterized by a straight line of slope 2 when representing $\log(|\log(c/c_{peak})|)$ against $\log(|x/\sigma|)$. Hence, any deviation from this slope corresponds to a non-Gaussian profile.

In Fig. C.1, we test the Gaussian assumption in the case of $\beta = 2$ for low and high Damköhler numbers, respectively $\mathrm{Da} = 10^{-3}$ and $\mathrm{Da} = 10^3$. At low Da, diffusion acts over much smaller time scales than reaction, and the profiles are Gaussian at all times (Fig. C.1.a and c), consistently with the hypothesis of Appendix B.1. For high Da, the early time profiles are non Gaussian and close to the initial square injection (Fig. C.1.b and d). In this regime, we do not assume Gaussianity but instead the dominance of reaction over diffusion (Appendix B.2.1). At late times, $t \gg \mathrm{Da}$, the profiles are very close to Gaussian (Fig. C.1.a and C.1.b) and closely follow the power law scaling of Eq. (C.1) (Fig. C.1.b and d), which is consistent with the assumption of Appendix B.2.2.

In Fig. C.2, we test the Gaussian assumption for the case of $\beta = 0.5$ for low Damköhler number, $\mathrm{Da} = 10^{-3}$. We do not represent large Da in Figure C.2 because mass reaches zero before $t = \mathrm{Da}$ in this case and only the first regime where we do not assume Gaussianity (Appendix B.2.1) is relevant. Again, consistently with the assumption of Appendix B.1, for low

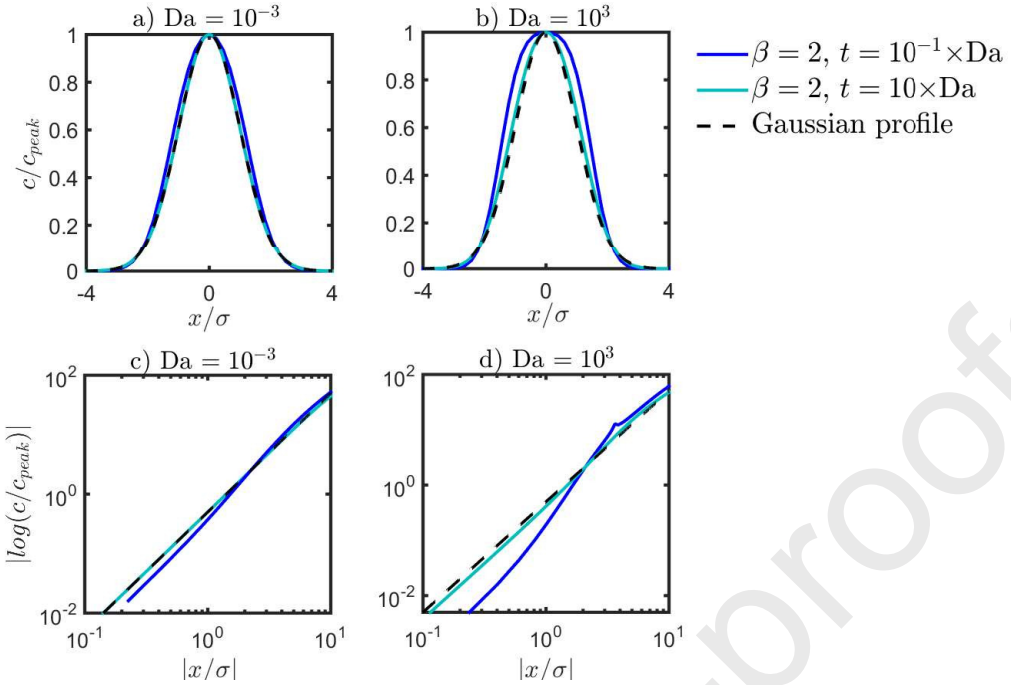

Figure C.1: Test of Gaussianity of reactive pulses from numerical simulations for $\beta = 2$. Comparison of reactive profiles, normalized by their peak values c_{peak} along the y axis and their standard deviation σ along the x axis, with Gaussian profiles at early and late times, respectively $t \approx 10^{-1} \times$ Da and $t \approx 10 \times$ Da for a) Da $= 10^{-3}$, and b) Da $= 10^{3}$. Test of Gaussian power law scaling (Eq. (C.1)) for the same cases respectively for c) low Da and d) high Da.

Da, the profiles are very close to Gaussian at all times (Fig. C.2.a) and closely follows the power law scaling of Eq. (C.1) (Fig. C.2.b). Results are similar for other reaction orders $\beta < 1$.

These results confirm the assumptions that we have made in Appendix B for deriving approximated analytical solution for the evolution of concentration distributions. For $t \ll$ Da, we dot not assume that profiles are Gaussian but we assume that diffusion plays no role and that the evolution of concentration profiles is dominated by reaction alone. For small Da, this regime is very short and not considered here. For large Da, this regime is discussed in Appendix B.2.1. For $t \gg$ Da, we assume that profiles are Gaussian, which is consistent with numerical simulations for all values of Da and β. This regime is discussed in Appendix B.1 and B.2.2.

C.2 Variance growth assumption

Here, we assess the validity of the assumption that the evolution of the variance is dominated by the diffusion term in Eq. (B.12). This leads to the prediction that the variance is constant for $t \ll$ Da and grows diffusively for $t \gg$ Da following Eq. (B.1) for Da ≤ 1 and Eq. (B.17) for Da > 1. We compare the variance growth in time obtained from numerical simulations with these predictions for different Damköhler numbers and β in Fig. C.3.

In all cases, simulations are found to be in good agreement with analytical solutions. Note that for $\beta < 1$, the variance computed from numerical simulations starts decreasing at the end of the simulations, which is not captured by our model (Fig. C.3, a). A short time before the whole profile reaches zero, concentrations on the sides are reacting faster than they diffuse so

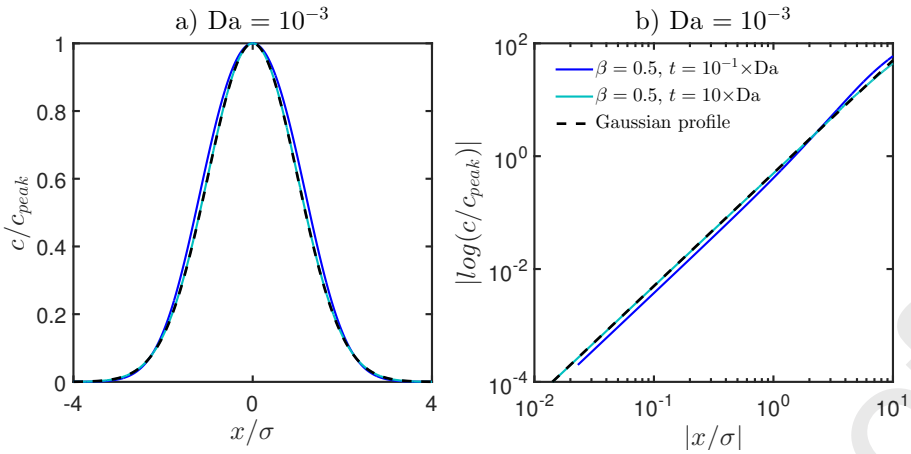

Figure C.2: Test of Gaussianity of reactive pulses from numerical simulations for $\beta = 0.5$. a) Comparison of reactive profiles, normalized by their peak values c_{peak} along the y axis and their standard deviation σ along the x axis, with Gaussian profiles at early and late times, $t \approx 10^{-1} \times$Da and $t \approx 10 \times$Da for Da $= 10^{-3}$. The high Da profile is not represented because the mean concentration reaches zero before the times at which we assume Gaussianity, $t =$ Da. b) Test of Gaussian power law scaling represented by Eq. (C.1).

that the variance starts to decrease before the whole profile reaches zero. This regime of variance decay is thus very short.

6 Research data

Research Data associated with this article can be accessed at https://doi.org/10.5281/zenodo.4114532.

References

Aagaard, P. and H. C. Helgeson (1982). "Thermodynamic and kinetic constraints on reaction rates among minerals and aqueous solutions; I, Theoretical considerations". In: *American journal of Science* 282.3, pp. 237–285.

Abel, C. D. T., S. K. Sharma, S. A. Mersha, and M. D. Kennedy (2014). "Influence of intermittent infiltration of primary effluent on removal of suspended solids, bulk organic matter, nitrogen and pathogens indicators in a simulated managed aquifer recharge system". In: *Ecological engineering* 64, pp. 100–107.

Al-Yamani, W., S. Green, R. Pangilinan, S. Dixon, S. A. Shahid, P. Kemp, and B. Clothier (2019). "Water use of Al Samr (Acacia tortilis) forests irrigated with saline groundwater and treated sewage effluent in the hyper-arid deserts of Abu Dhabi". In: *Agricultural Water Management* 216, pp. 361–364.

Atchley, A. L., R. M. Maxwell, and A. K. Navarre-Sitchler (2013). "Using streamlines to simulate stochastic reactive transport in heterogeneous aquifers: Kinetic metal release and transport in CO2 impacted drinking water aquifers". In: *Advances in water resources* 52, pp. 93–106.

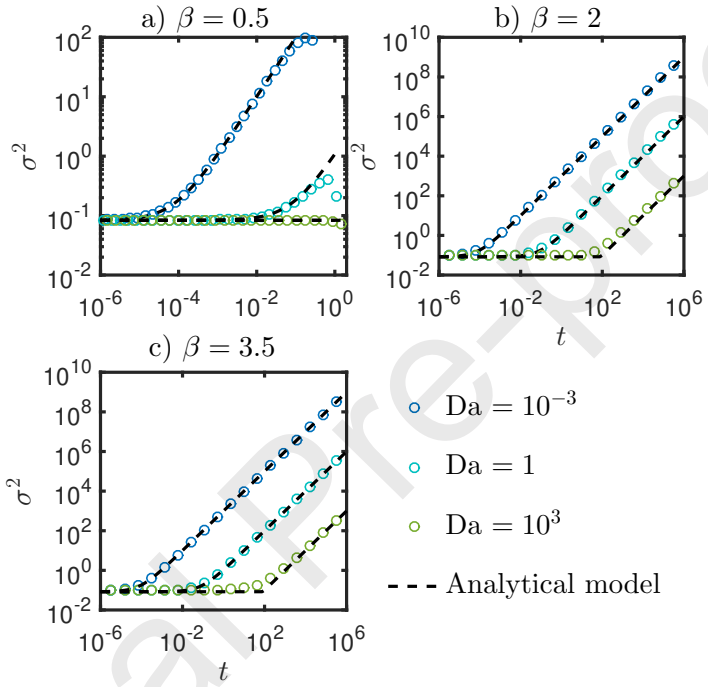

Figure C.3: Test of analytical model for variance growth. Temporal evolution of the reactive pulse variance for a) $\beta = 0.5$, b) $\beta = 2$, c) $\beta = 3.5$, and Da $= 0.001$ (blue circles), Da $= 1$ (turquoise circles), and Da $= 1000$ (green circles). The analytical model predictions, shown by black dashed lines, is given by Eq. (B.1) for Da ≤ 1 and Eq. (B.17) for Da ≥ 1

Atchley, A. L., A. K. Navarre-Sitchler, and R. M. Maxwell (2014). "The effects of physical and geochemical heterogeneities on hydro-geochemical transport and effective reaction rates". In: *Journal of contaminant hydrology* 165, pp. 53–64.

Bandopadhyay, A., P. Davy, and T. Le Borgne (2018). "Shear flows accelerate mixing dynamics in hyporheic zones and hillslopes". In: *Geophysical Research Letters* 45.21, pp. 11–659.

Battiato, I. and D. M. Tartakovsky (2011). "Applicability regimes for macroscopic models of reactive transport in porous media". In: *Journal of contaminant hydrology* 120, pp. 18–26.

Battiato, I., D. M. Tartakovsky, A. M. Tartakovsky, and T. Scheibe (2009). "On breakdown of macroscopic models of mixing-controlled heterogeneous reactions in porous media". In: *Advances in water resources* 32.11, pp. 1664–1673.

Beckingham, L. E., E. H. Mitnick, C. I. Steefel, S. Zhang, M. Voltolini, A. M. Swift, L. Yang, D. R. Cole, J. M. Sheets, J. B. Ajo-Franklin, et al. (2016). "Evaluation of mineral reactive surface area estimates for prediction of reactivity of a multi-mineral sediment". In: *Geochimica et Cosmochimica Acta* 188, pp. 310–329.

Beckingham, L. E., C. I. Steefel, A. M. Swift, M. Voltolini, L. Yang, L. M. Anovitz, J. M. Sheets, D. R. Cole, T. J. Kneafsey, E. H. Mitnick, et al. (2017). "Evaluation of accessible mineral surface areas for improved prediction of mineral reaction rates in porous media". In: *Geochimica et Cosmochimica Acta* 205, pp. 31–49.

Berkowitz, B., A. Cortis, M. Dentz, and H. Scher (2006). "Modeling non-Fickian transport in geological formations as a continuous time random walk". In: *Reviews of Geophysics* 44.2.

Bethke, C. (1996). *Geochemical reaction modeling: Concepts and applications*. Oxford University Press on Demand.

Bleam, W. (2017). "Chapter 9-reduction-oxidation chemistry". In: *Soil and Environmental Chemistry*, pp. 445–489.

Bochet, O., L. Bethencourt, A. Dufresne, J. Farasin, M. Pédrot, T. Labasque, E. Chatton, N. Lavenant, C. Petton, B. W. Abbott, et al. (2020). "Iron-oxidizer hotspots formed by intermittent oxic–anoxic fluid mixing in fractured rocks". In: *Nature Geoscience* 13.2, pp. 149–155.

Burté, L., C. A. Cravotta III, L. Bethencourt, J. Farasin, M. Pédrot, A. Dufresne, M.-F. Gerard, C. Baranger, T. Le Borgne, and L. Aquilina (2019). "Kinetic study on clogging of a geothermal pumping well triggered by mixing-induced biogeochemical reactions". In: *Environmental science & technology* 53.10, pp. 5848–5857.

Datta, S., B. Mailloux, H.-B. Jung, M. A. Hoque, M. Stute, K. M. Ahmed, and Y. Zheng (2009). "Redox trapping of arsenic during groundwater discharge in sediments from the Meghna riverbank in Bangladesh". In: *Proceedings of the National Academy of Sciences* 106.40, pp. 16930–16935.

De Anna, P., J. Jimenez-Martinez, H. Tabuteau, R. Turuban, T. Le Borgne, M. Derrien, and Y. Meheust (2014a). "Mixing and reaction kinetics in porous media: An experimental pore scale quantification". In: *Environmental Science and Technology* 48.1, pp. 508–516.

De Anna, P., M. Dentz, A. Tartakovsky, and T. Le Borgne (2014b). "The filamentary structure of mixing fronts and its control on reaction kinetics in porous media flows". In: *Geophysical Research Letters* 41.13, pp. 4586–4593.

DePaolo, D. J. and D. R. Cole (2013). "Geochemistry of geologic carbon sequestration: an overview". In: *Reviews in Mineralogy and Geochemistry* 77.1, pp. 1–14.

Deng, H., S. Molins, D. Trebotich, C. Steefel, and D. DePaolo (2018). "Pore-scale numerical investigation of the impacts of surface roughness: Upscaling of reaction rates in rough fractures". In: *Geochimica et Cosmochimica Acta* 239, pp. 374–389.

Dentz, M., T. Le Borgne, A. Englert, and B. Bijeljic (2011a). "Mixing, spreading and reaction in heterogeneous media: A brief review". In: *Journal of contaminant hydrology* 120, pp. 1–17.

Dentz, M., T. Le Borgne, A. Englert, and B. Bijeljic (2011b). "Mixing, spreading and reaction in heterogeneous media: A brief review". In: *Journal of Contaminant Hydrology* 120-121, pp. 1–17.

Dutta, T., A. Carles-Brangarí, D. Fernàndez-Garcia, S. Rubol, J. Tirado-Conde, and X. Sanchez-Vila (2015). "Vadose zone oxygen (O2) dynamics during drying and wetting cycles: an artificial recharge laboratory experiment". In: *Journal of Hydrology* 527, pp. 151–159.

Elberling, B, R. Nicholson, and J. Scharer (1994). "A combined kinetic and diffusion model for pyrite oxidation in tailings: a change in controls with time". In: *Journal of Hydrology* 157.1-4, pp. 47–60.

Fenwick, D., C. Scheidt, and J. Caers (2014). "Quantifying asymmetric parameter interactions in sensitivity analysis: application to reservoir modeling". In: *Mathematical Geosciences* 46.4, pp. 493–511.

Giammar, D. E., R. G. Bruant Jr, and C. A. Peters (2005). "Forsterite dissolution and magnesite precipitation at conditions relevant for deep saline aquifer storage and sequestration of carbon dioxide". In: *Chemical Geology* 217.3-4, pp. 257–276.

Gramling, C. M., C. F. Harvey, and L. C. Meigs (2002). "Reactive transport in porous media: A comparison of model prediction with laboratory visualization". In: *Environmental science & technology* 36.11, pp. 2508–2514.

Guo, J., M. Quintard, and F. Laouafa (2015). "Dispersion in porous media with heterogeneous nonlinear reactions". In: *Transport in Porous Media* 109.3, pp. 541–570.

Hellmann, R. and D. Tisserand (2006). "Dissolution kinetics as a function of the Gibbs free energy of reaction: An experimental study based on albite feldspar". In: *Geochimica et Cosmochimica Acta* 70.2, pp. 364–383.

Hermans, T., F. Nguyen, M. Klepikova, A. Dassargues, and J. Caers (2018). "Uncertainty quantification of medium-term heat storage from short-term geophysical experiments using Bayesian evidential learning". In: *Water Resources Research* 54.4, pp. 2931–2948.

Heyman, J., D. R. Lester, R. Turuban, Y. Méheust, and T. Le Borgne (2020). "Stretching and folding sustain microscale chemical gradients in porous media". In: *Proceedings of the National Academy of Sciences*.

Hinsinger, P., C. Plassard, C. Tang, and B. Jaillard (2003). "Origins of root-mediated pH changes in the rhizosphere and their responses to environmental constraints: a review". In: *Plant and soil* 248.1-2, pp. 43–59.

Hubbard, C. G., S. Black, and M. L. Coleman (2009). "Aqueous geochemistry and oxygen isotope compositions of acid mine drainage from the Río Tinto, SW Spain, highlight inconsistencies in current models". In: *Chemical Geology* 265.3-4, pp. 321–334.

Hubert, A., T. Aquino, H. Tabuteau, Y. Méheust, and T. Le Borgne (2020). "Enhanced and non-monotonic effective kinetics of solute pulses under Michaelis–Menten reactions". In: *Advances in Water Resources* 146, p. 103739.

Johnson, N. C., B. Thomas, K. Maher, R. J. Rosenbauer, D. Bird, and G. E. Brown Jr (2014). "Olivine dissolution and carbonation under conditions relevant for in situ carbon storage". In: *Chemical Geology* 373, pp. 93–105.

Jun, Y.-S., D. E. Giammar, and C. J. Werth (2013). *Impacts of geochemical reactions on geologic carbon sequestration*.

Jung, H. and A. Navarre-Sitchler (2018a). "Physical heterogeneity control on effective mineral dissolution rates". In: *Geochimica et Cosmochimica Acta* 227, pp. 246–263.

— (2018b). "Scale effect on the time dependence of mineral dissolution rates in physically heterogeneous porous media". In: *Geochimica et Cosmochimica Acta* 234, pp. 70–83.

Keiluweit, M., P. S. Nico, M. Kleber, and S. Fendorf (2016). "Are oxygen limitations under recognized regulators of organic carbon turnover in upland soils?" In: *Biogeochemistry* 127.2, pp. 157–171.

Kirchner, J. W. and C. Neal (2013). "Universal fractal scaling in stream chemistry and its implications for solute transport and water quality trend detection". In: *Proceedings of the National Academy of Sciences* 110.30, pp. 12213–12218.

Kitanidis, P. K. (1994). "The concept of the dilution index". In: *Water resources research* 30.7, pp. 2011–2026.

Kitanidis, P. K. and P. L. McCarty (2012). *Delivery and Mixing in the Subsurface: Processes and Design Principles for In Situ Remediation*. Vol. 4. Springer Science & Business Media.

Largitte, L. and R. Pasquier (2016). "A review of the kinetics adsorption models and their application to the adsorption of lead by an activated carbon". In: *Chemical Engineering Research and Design* 109, pp. 495–504.

Lasaga, A. C., J. M. Soler, J. Ganor, T. E. Burch, and K. L. Nagy (1994). "Chemical weathering rate laws and global geochemical cycles". In: *Geochimica et Cosmochimica Acta* 58.10, pp. 2361–2386.

Lazareva, O., G. Druschel, and T. Pichler (2015). "Understanding arsenic behavior in carbonate aquifers: Implications for aquifer storage and recovery (ASR)". In: *Applied Geochemistry* 52, pp. 57–66.

Le Borgne, T., M. Dentz, and E. Villermaux (2013). "Stretching, coalescence, and mixing in porous media". In: *Physical review letters* 110.20, p. 204501.

Le Borgne, T., T. R. Ginn, and M. Dentz (2014). "Impact of fluid deformation on mixing-induced chemical reactions in heterogeneous flows". In: *Geophysical Research Letters* 41.22, pp. 7898–7906.

Le Borgne, T., M. Dentz, and E. Villermaux (2015). "The lamellar description of mixing in porous media". In:

Le Borgne, T., P. D. Huck, M. Dentz, and E. Villermaux (2017). "Scalar gradients in stirred mixtures and the deconstruction of random fields". In:

Li, L., C. I. Steefel, and L. Yang (2008). "Scale dependence of mineral dissolution rates within single pores and fractures". In: *Geochimica et Cosmochimica Acta* 72.2, pp. 360–377.

Li, L., K. Maher, A. Navarre-Sitchler, J. Druhan, C. Meile, C. Lawrence, J. Moore, J. Perdrial, P. Sullivan, and A. e. a. Thompson (2017). "Expanding the role of reactive transport models in critical zone processes". In: *Earth-science reviews* 165, pp. 280–301.

Llewellyn, G. T., F. Dorman, J. L. Westland, D. Yoxtheimer, P. Grieve, T. Sowers, E. Humston-Fulmer, and S. L. Brantley (2015). "Evaluating a groundwater supply contamination incident attributed to Marcellus Shale gas development". In: *Proceedings of the National Academy of Sciences* 112.20, pp. 6325–6330.

Magesan, G. N., C. D. A. McLay, and V. V. Lal (1998). "Nitrate leaching from a free-draining volcanic soil irrigated with municipal sewage effluent in New Zealand". In: *Agriculture, ecosystems & environment* 70.2-3, pp. 181–187.

Maher, K. (2011). "The role of fluid residence time and topographic scales in determining chemical fluxes from landscapes". In: *Earth and Planetary Science Letters* 312.1-2, pp. 48–58.

Maher, K. and C. P. Chamberlain (2014). "Hydrologic regulation of chemical weathering and the geologic carbon cycle". In: *Science* 343.6178, pp. 1502–1504.

Maher, K. and A. Navarre-Sitchler (2019). "Reactive transport processes that drive chemical weathering: From making space for water to dismantling continents". In: *Reviews in Mineralogy and Geochemistry* 85.1, pp. 349–380.

Maher, K. and K. U. Mayer (2019). "The art of reactive transport model building". In: *Elements* 15.2, pp. 117–118.

Maher, K., C. I. Steefel, D. J. DePaolo, and B. E. Viani (2006). "The mineral dissolution rate conundrum: Insights from reactive transport modeling of U isotopes and pore fluid chemistry in marine sediments". In: *Geochimica et Cosmochimica Acta* 70.2, pp. 337–363.

Malmström, M. E., G. Destouni, S. A. Banwart, and B. H. E. Strömberg (2000). "Resolving the scale-dependence of mineral weathering rates". In: *Environmental science & technology* 34.7, pp. 1375–1378.

Malzone, J. M., C. S. Lowry, and A. S. Ward (2016). "Response of the hyporheic zone to transient groundwater fluctuations on the annual and storm event time scales". In: *Water Resources Research* 52.7, pp. 5301–5321.

McKibben, M. A. and H. L. Barnes (1986). "Oxidation of pyrite in low temperature acidic solutions: Rate laws and surface textures". In: *Geochimica et Cosmochimica Acta* 50.7, pp. 1509–1520.

Meile, C. and K. Tuncay (2006). "Scale dependence of reaction rates in porous media". In: *Advances in Water Resources* 29.1, pp. 62–71.

Molins, S., D. Trebotich, C. I. Steefel, and C. Shen (2012). "An investigation of the effect of pore scale flow on average geochemical reaction rates using direct numerical simulation". In: *Water Resources Research* 48.3.

Molins, S., D. Trebotich, L. Yang, J. B. Ajo-Franklin, T. J. Ligocki, C. Shen, and C. I. Steefel (2014). "Pore-scale controls on calcite dissolution rates from flow-through laboratory and numerical experiments". In: *Environmental science & technology* 48.13, pp. 7453–7460.

Moussout, H., H. Ahlafi, M. Aazza, and H. Maghat (2018). "Critical of linear and nonlinear equations of pseudo-first order and pseudo-second order kinetic models". In: *Karbala International Journal of Modern Science* 4.2, pp. 244–254.

Murphy, S. F., R. B. McCleskey, D. A. Martin, J. H. Writer, and B. A. Ebel (2018). "Fire, flood, and drought: extreme climate events alter flow paths and stream chemistry". In: *Journal of Geophysical Research: Biogeosciences* 123.8, pp. 2513–2526.

Navarre-Sitchler, A. and S. Brantley (2007). "Basalt weathering across scales". In: *Earth and Planetary Science Letters* 261.1-2, pp. 321–334.

Palandri, J. L. and Y. K. Kharaka (2004). *A compilation of rate parameters of water-mineral interaction kinetics for application to geochemical modeling*. Tech. rep. Geological Survey Menlo Park CA.

Panfilov, M. (2010). "Underground storage of hydrogen: in situ self-organisation and methane generation". In: *Transport in porous media* 85.3, pp. 841–865.

Perry, R. H., D. W. Green, and J. O. Maloney (1997). "Perry's handbook of chemical engineering". In: *Perry's Handbook of Chemical Engineering*.

Plummer, L. N. and T. M. L. Wigley (1976). "The dissolution of calcite in CO2-saturated solutions at 25 C and 1 atmosphere total pressure". In: *Geochimica et Cosmochimica Acta* 40.2, pp. 191–202.

Pujades, E., S. Orban P.and Bodeux, P. Archambeau, S. Erpicum, and A. Dassargues (2017). "Underground pumped storage hydropower plants using open pit mines: How do groundwater exchanges influence the efficiency?" In: *Applied energy* 190, pp. 135–146.

Robati, D. (2013). "Pseudo-second-order kinetic equations for modeling adsorption systems for removal of lead ions using multi-walled carbon nanotube". In: *Journal of nanostructure in Chemistry* 3.1, p. 55.

Rolle, M. and T. Le Borgne (2019). "Mixing and reactive fronts in the subsurface". In: *Reviews in Mineralogy and Geochemistry* 85.1, pp. 111–142.

Rudzinski, W. and W. Plazinski (2006). "Kinetics of solute adsorption at solid/solution interfaces: a theoretical development of the empirical pseudo-first and pseudo-second order kinetic rate

equations, based on applying the statistical rate theory of interfacial transport". In: *The Journal of Physical Chemistry B* 110.33, pp. 16514–16525.
Salehikhoo, F., L. Li, and S. L. Brantley (2013). "Magnesite dissolution rates at different spatial scales: The role of mineral spatial distribution and flow velocity". In: *Geochimica et Cosmochimica Acta* 108, pp. 91–106.
Serrano, S. E. (2001). "Solute transport under non-linear sorption and decay". In: *Water Research* 35.6, pp. 1525–1533.
— (2003). "Propagation of nonlinear reactive contaminants in porous media". In: *Water Resources Research* 39.8.
Skeel, R. D. and M. Berzins (1990). "A method for the spatial discretization of parabolic equations in one space variable". In: *SIAM journal on scientific and statistical computing* 11.1, pp. 1–32.
Song, X., J. Zhang, C. Zhan, Y. Xuan, M. Ye, and C. Xu (2015). "Global sensitivity analysis in hydrological modeling: Review of concepts, methods, theoretical framework, and applications". In: *Journal of hydrology* 523, pp. 739–757.
Soulaine, C., S. Roman, A. Kovscek, and H. A. Tchelepi (2017). "Mineral dissolution and wormholing from a pore-scale perspective". In:
Steefel, C. I. and A. C. Lasaga (1994). "A coupled model for transport of multiple chemical species and kinetic precipitation/dissolution reactions with application to reactive flow in single phase hydrothermal systems". In: *American Journal of science* 294.5, pp. 529–592.
Steefel, C., C. Appelo, B. Arora, D. Jacques, T. Kalbacher, O Kolditz, V. Lagneau, P. Lichtner, K. U. Mayer, J. Meeussen, et al. (2015). "Reactive transport codes for subsurface environmental simulation". In: *Computational Geosciences* 19.3, pp. 445–478.
Steefel, C. I., D. J. DePaolo, and P. C. Lichtner (2005). "Reactive transport modeling: An essential tool and a new research approach for the Earth sciences". In: *Earth and Planetary Science Letters* 240.3-4, pp. 539–558.
Szulczewski, M. L., C. W. MacMinn, H. J. Herzog, and R. Juanes (2012). "Lifetime of carbon capture and storage as a climate-change mitigation technology". In: *Proceedings of the National Academy of Sciences* 109.14, pp. 5185–5189.
Trauth, N. and J. H. Fleckenstein (2017). "Single discharge events increase reactive efficiency of the hyporheic zone". In: *Water Resources Research* 53.1, pp. 779–798.
Urióstegui, S. H., R. K. Bibby, B. K. Esser, and J. F. Clark (2016). "Quantifying groundwater travel time near managed recharge operations using 35S as an intrinsic tracer". In: *Journal of Hydrology* 543, pp. 145–154.
Valocchi, A. J., D. Bolster, and C. J. Werth (2019). "Mixing-limited reactions in porous media". In: *Transport in Porous Media* 130.1, pp. 157–182.
Van Cappellen, P. and J.-F. Gaillard (2018). "Biogeochemical dynamics in aquatic sediments". In: *Reactive transport in porous media*, pp. 335–376.
Villermaux, E. (2019). "Mixing versus stirring". In: *Annual Review of Fluid Mechanics* 51, pp. 245–273.
Wang, L., H. Wen, and L. Li (2018). "Scale dependence of surface complexation capacity and rates in heterogeneous media". In: *Science of The Total Environment* 635, pp. 1547–1555.
Weber J., W. J., P. M. McGinley, and L. E. Katz (1991). "Sorption phenomena in subsurface systems: concepts, models and effects on contaminant fate and transport". In: *Water research* 25.5, pp. 499–528.
Wen, H. and L. Li (2017a). "An upscaled rate law for magnesite dissolution in heterogeneous porous media". In: *Geochimica et Cosmochimica Acta* 210, pp. 289–305.
— (2017b). "An upscaled rate law for magnesite dissolution in heterogeneous porous media". In: *Geochimica et Cosmochimica Acta* 210, pp. 289–305.

Wen, H. and L. Li (2018). "An upscaled rate law for mineral dissolution in heterogeneous media: The role of time and length scales". In: *Geochimica et Cosmochimica Acta* 235, pp. 1–20.

White, A. F. and S. L. Brantley (2003). "The effect of time on the weathering of silicate minerals: why do weathering rates differ in the laboratory and field?" In: *Chemical Geology* 202.3-4, pp. 479–506.

Wu, F.-C., R.-L. Tseng, S.-C. Huang, and R.-S. Juang (2009). "Characteristics of pseudo-second-order kinetic model for liquid-phase adsorption: a mini-review". In: *Chemical Engineering Journal* 151.1-3, pp. 1–9.

Xu, T., S. P. White, K. Pruess, and G. H. Brimhall (2000). "Modeling of pyrite oxidation in saturated and unsaturated subsurface flow systems". In: *Transport in porous media* 39.1, pp. 25–56.

Yang, C., J. Samper, J. Molinero, and M. Bonilla (2007). "Modelling geochemical and microbial consumption of dissolved oxygen after backfilling a high level radiactive waste repository". In: *Journal of Contaminant Hydrology* 93.1-4, pp. 130–148.

Effective kinetics driven by dynamic concentration gradients under coupled transport and reaction

Charlotte Le Traon*[1], Tomás Aquino[1], Camille Bouchez[1], Kate Maher[2], and Tanguy Le Borgne[1]

[1]Université de Rennes 1, CNRS, Géosciences Rennes UMR 6118, 35042 Rennes, France
[2]Department of Geological and Environmental Sciences, Braun Hall #118, 450 Serra Mall, Stanford University, Stanford, CA, 94305, USA

March 31, 2021

Abstract

Biogeochemical reaction kinetics are generally established from batch reactors where concentrations are uniform. In natural systems, many biogeochemical processes are characterized by spatially and temporally variable concentration gradients that often occur at scales which are not resolved by field measurements or biogeochemical and reactive transport models. Yet, it is not clear how these sub-scale chemical gradients affect reaction kinetics compared to batch kinetics. Here we investigate this question by studying the paradigmatic case of localized pulses of solute reacting with a solid or a dissolved species in excess. We consider non-linear biogeochemical reactions, representative of mineral dissolution, adsorption and redox reactions, which we quantify using simplified power-law kinetics. The combined effect of diffusion and reaction leads to effective kinetics that differ quantitatively and qualitatively from the batch kinetics. Depending on the nonlinearity (reaction order) of the local kinetics, these effects lead to either enhancement or decrease of the overall reaction rate, and result in a rich variety of reaction dynamics. We derive analytical results for the effective kinetics, which are validated by comparison to direct numerical simulations for a broad range of Damköhler numbers and reaction order. Our findings provide new insights into the interpretation of imperfectly mixed lab experiments, the effective kinetics of field systems characterized by intermittent reactant release and the integration of sub-scale concentration gradients in reactive transport models.

1 Introduction

The kinetics of biogeochemical reactions are used to predict a range of processes , including the weathering of rock, the transport and degradation contaminants, and the nutrient cycling that sustains subsurface microbial life. Given the importance of transport processes in governing the removal and supply of products and reactants and the necessity to consider a variety of spatial and temporal scales, reactive transport models are increasingly used to predict processes occurring in the subsurface (e.g., see reviews by Van Cappellen and Gaillard, 2018; Steefel et al., 2005; Li et al., 2017; Maher and

*Corresponding author: charlotte.letraon@univ-rennes1.fr

) A host of other studies rely on conceptual frameworks that integrate reactive transport principles, with applications ranging from interpretation of global elemental cycles (Lasaga et al., 1994) , to catchment elemental fluxes over synoptic (e.g. Kirchner and Neal, 2013) or geologic timescales (e.g. Maher and Chamberlain, 2014), to nutrient cycling at microsites (e.g. Keiluweit et al., 2016) . In all cases, biogeochemical kinetics have to be represented at an appropriate temporal and spatial scale. However, kinetic models are generally derived from well-mixed batch experiments in the lab . Yet, reaction kinetics can differ by orders of magnitude from homogeneous batch reactors to heterogeneous field systems (White and Brantley, 2003; Meile and Tuncay, 2006; Maher et al., 2006; Navarre-Sitchle . Different hypotheses have been investigated to explain these discrepancies. These include diffusion limitations or geometrical constraints at the pore scale that reduce access of solutes to reactive surfaces compared to fully mixed systems (Molins et al., 2012; Molins et al., 2014; Beckingham et al., 2016; Soula , physical heterogeneity that induces spatially heterogeneous solute fluxes and modifies the effective reactive surfaces (Atchley et al., 2013; Wen and Li, 2017a; Wen and Li, 2018; Jung and Navarre-Sitchler, 2018a; and geochemical heterogeneity, where averaging can also lead to scale effects in effective reaction kinetics (Atchley et al., 2014; Salehikhoo et al., 2013). These studies highlight the role of delayed or heterogeneous access to reactive surfaces at different scales. A complementary question that has received less attention is: what is the impact of heterogeneous and time evolving concentration landscapes on reaction kinetics, when access to reactive surfaces or to other dissolved reactants is not limited?

Concentration gradients are created by spatially heterogeneous or transient release of solutes. They can be sustained by stretching induced by flow, whether at pore scale (Heyman et al., 2020) or at Darcy scale (Le Borgne et al., 2017), and are ultimately destroyed by diffusion. In the case of linear kinetics, heterogeneity in concentration fields does not impact the effective kinetics when access to reactive surfaces or other reactants is not limited. However, for non-linear kinetics that imply the local reaction rate is a non-linear function of local solute concentrations, the average reaction rate over a non-homogeneous concentration field is expected to differ from the local kinetics (Battiato et al., 2009; Battiato and Tartakovsky, 2011; Hubert et al., 2020). Such non-linear reaction kinetics play a central role in a broad range of biogeochemical reactions, including dissolution, redox and sorption reactions (Serrano, 2001; Serrano, 2003; Guo et al., 2015). Yet, it is not known how different types of non-linear kinetics may lead to either enhanced or reduced effective kinetics when considering heterogeneous solute plumes.

Many physical, climatic, and biological processes result in localized and intermittent release of solutes that generate temporally and spatially variable concentration fields in subsurface environments (Fig. 1). Rain events (Fig. 1.a) leach soil and induce pulses of dissolved chemical compounds into groundwater (Murphy et al., 2018). River stage variations (Fig. 1.b) induce pulses of oxygen-rich water in hyporheic zones and the underlying groundwater systems, leading to chemical disequilibrium and the degradation, fixation or release of contaminants, such as organic carbon, nitrate or arsenic (Datta et al., 2009; Malzone et al., 2016; Trauth and Fleckenstein, 2017; Bandopadhyay et al., 2018). Biological activity in general (Fig. 1.c) , can induce pulses of chemical compounds (e.g. Hinsinger et al., 2003). For instance, roots release dissolved gases and other compounds through daily cycles of respiration and exudation, and via associated fungal and microbial organisms (e.g. Li et al., 2017). Finally engineered injections (Fig. 1.d) create chemical disequilibrium and trigger a range of reactive pulses. This includes managed aquifer recharge (Magesan et al., 1998; Urióstegui et al., 2016; Al-Yamani et al., 2019) , which is often performed by periodically wetting and drying the system (Dutta et al., 2015), leading to biogeochemical reactions such as ammonium-nitrogen reduction and pathogen removal (Abel et al., 2014). Injection of concentrated carbon dioxide into the deep subsurface results in density-driven instabilities, leading to localized high concentrations of reactive CO_2-rich fluid (Szulczewski et al., 2012). Collectively, reactive pulses play an important role in a broad range of

engineered injections, including soil and groundwater remediation (Kitanidis and McCarty, 2012; Rolle and Le Borgne, 2019), seasonal energy storage, through heat, hydrogen or underground pumped storage hydroelectricity (Panfilov, 2010; Pujades et al., 2017; Hermans et al., 2018), geothermal dipoles (Burté et al., 2019), and injection and storage of water used for fracking operations (Llewellyn et al., 2015).

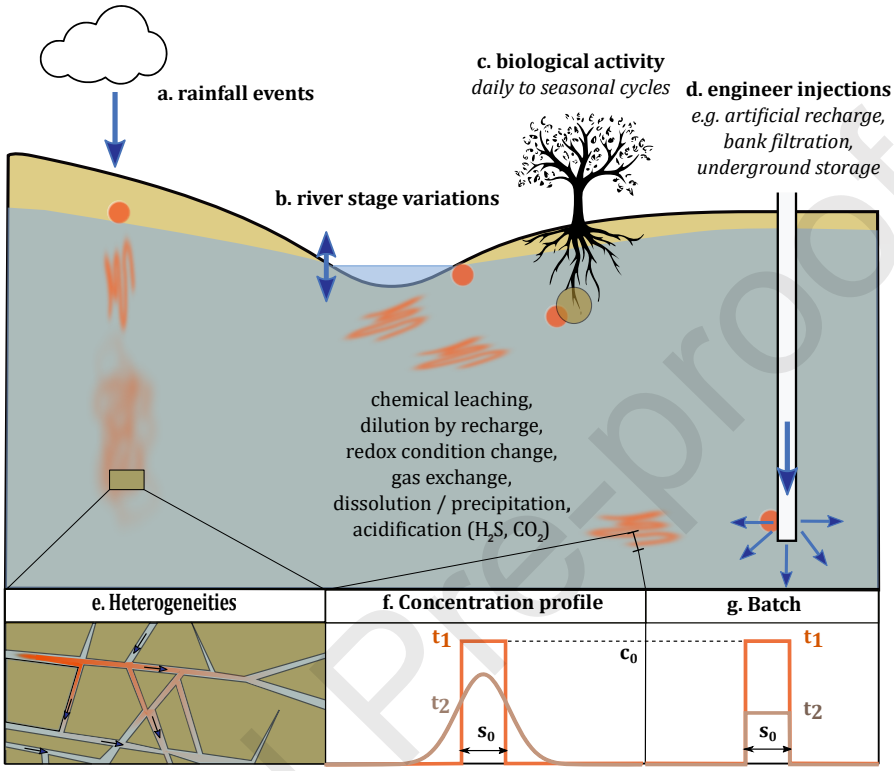

Figure 1: Conceptual representation of biogeochemical pulses in the subsurface. When released, pulses are concentrated and localized (orange dots). As they are transported in the subsurface, they are stretched by velocity gradients and form elongated lamella structures (Le Borgne et al., 2015). Solute concentrations are driven by dilution, which occurs by diffusion along the concentration gradients, and reactions either with minerals or other dissolved solutes. The arrows indicate an injection or an exchange of solute. Four types of processes generating reactive pulses are highlighted: a. soil leaching by rain, b. surface water – groundwater exchanges, c. biological activity (the brown circle represents the root zone), and d. engineered injections. In all these applications, chemical gradients can be enhanced and sustained by physical heterogeneities, as illustrated in inset e. The inset f. illustrates the considered simplified one-dimensional concentration profile that evolve under the action of diffusion and reaction. The effective kinetics of such reactive pulses are compared to batch kinetics that evolve through reaction alone under uniform concentrations (inset g.).

Because chemical gradients are enhanced and sustained by physical heterogeneities (Le Borgne et al., 2013; Heyman et al., 2020) (see inset of Fig. 1) , they develop over a range of scales that cannot be fully resolved by field sampling approaches that average solute (e.g., screened groundwater wells) or reactive transport models. Hence, effective kinetic models that capture the effect of sub-scale concentration gradients are required. Macrodispersion theory, where the dispersive flux is assumed to be proportional to the concentration gradient, tends to strongly

underestimate concentration gradients, leading to significant errors when used in reactive transport models (Gramling et al., 2002; Dentz et al., 2011a). Non-Fickian dispersion theories have successfully described the asymmetry of solute plumes resulting from trapping in low velocity areas (Berkowitz et al., 2006). However, this framework aims at describing spatial dispersion of solute plumes and does not quantify subscale concentration gradients governed by mixing (Dentz et al., 2011b). Recent mixing theories have provided a new framework to predict the full distribution of concentrations and concentration gradients both at pore scale (Heyman et al., 2020) and at Darcy scale (Le Borgne et al., 2013). In this framework, solute plumes are represented as ensembles of elongated lamellar structures, i.e. solute filaments elongated in one direction and compressed in the other. The latter develop systematically in heterogeneous media both at the pore (De Anna et al., 2014b) and Darcy (Le Borgne et al., 2014) scale. This is due to velocity gradients at different scales that deform solute plumes into such filaments, whose formation and merging controls mixing rates (Le Borgne et al., 2015). At the scale of a solute lamella, the effect of stretching on the enhancement of concentration gradients and mixing is quantified explicitly by a change of variable that leads to one-dimensional equation formally identical to a diffusion equation in the direction perpendicular to the lamella (Villermaux, 2019) . The full distribution of concentration is then predicted from the distribution of stretching rates. While this framework has been successfully used to model mixing-limited reactions (De Anna et al., 2014a; Rolle and Le Borgne, 2019), its coupling with other types of reactions, such as solid-fluid reactions is an outstanding challenge. The key difficulty for this is to first solve analytically the coupling of diffusion transverse to solute lamella with non-linear kinetic laws.

Here we use analytical solutions and numerical simulations to establish the effective kinetic laws that result from coupled diffusion and non-linear reactions in spatially and temporally variable concentration gradients. We consider pulses of solute that react either with a homogeneously distributed solid phase or fluid phase, both in excess with respect to the transported solute. Hence, there is no limitation of access to reactive surfaces or other reactants, which allow use to isolate and formalize the coupling between non-homogeneous concentration distributions and non-linear kinetics. Dilution of solute concentration by mixing with the background fluid transfers high concentrations towards lower concentrations (Kitanidis, 1994), which may either reduce or enhance the average kinetics, depending on the reaction order of the local kinetics. Although mixing plays an important role in this problem, it does not act to bring reactants into contact as extensively studied in the context of mixing-induced reactions, where reactions are limited by the mixing of spatially segregated reactants (see recent reviews of Rolle and Le Borgne, 2019; Valocchi et al., 2019). Instead, we study how changes in concentration distributions by mixing may lead to the emergence of effective kinetics that differ from local kinetics. In complex multi-component reactions, this effect acts together with a range of other processes and therefore it is difficult to understand and quantify. Therefore, although we have studied a simplified reaction in order to isolate a particular phenomenon, our results are expected to be relevant to a large range of geochemical systems, where this effect acts together with other known mechanisms, including spatial segregation of reactants either in fluid or in solid phases. In section 2, we present the reactive transport problem. In section 2.1, we define the studied effective quantities. In section 3, we present the numerical and analytical results for a range of Damköhler numbers and non-linear kinetics. In the section 4, we discuss the implications of our findings for different types of reaction, including mineral dissolution, redox reactions and soprtion.

2 Reactive transport problem

2.1 Reaction kinetics

We study the reaction of a mobile aqueous species, with concentration c, which reacts with other aqueous species or with a solid surface. The latter are assumed to be in excess and homogeneously distributed, so that the reaction kinetics r(c) only depends on the concentration c through the non-linear rate law:

$$r(c) = kc^{\beta}, \tag{1}$$

where $\beta > 0$ is the effective order of the reaction and k is the reaction rate constant, which integrates the effect of other species in excess (units [$\mathrm{mol}^{1-\beta} L^{d(\beta-1)} T^{-1}$], where d is the spatial dimension).

In a well-mixed batch reactor, the concentration c is homogeneous in space and depends only on time (see lower right inset of Fig. 1). The concentration decreases everywhere according to the reaction rate (1), so that the kinetic rate law describing the evolution of the mean concentration $\overline{c}$ as a function of time t is given by

$$\frac{d}{dt}\overline{c} = -r(\overline{c}), \tag{2}$$

with $\overline{c} = M/V$, where M is the mass of reactant and V is the volume of the batch reactor.

Although it is simplified, the system isolates the effect of transient concentration gradients on upscaled kinetics. The characterization of this basic yet non-trivial system may thus guide the understanding of more complex biogeochemical systems, where this effect is coupled to other mechanisms, such as heterogeneous reactive surfaces, spatial segregation of multiple elements and mixing limitations. As discussed in section 4, it is relevant for mineral dissolution far-from-equilibrium (Hellmann and Tisserand, 2006; Maher, 2011; Guo et al., 2015), for non-linear sorption kinetics (Weber J. et al., 1991; Perry et al., 1997; Serrano, 2003) and for homogeneous redox reactions where β depends on the stoichiometric coefficients (Bethke, 1996; Bleam, 2017) . We focus on $\beta \neq 1$, because dilution by mixing has no effect on linear reactions in the sense that the upscaled kinetics are the same as the local kinetics in this case. Indeed, for the linear reaction, $\beta = 1$, mass decay over time is independent of the spatial concentration distribution.

2.2 Reactive pulses

We wish to compare the batch dynamics Eq. (2), to the dynamics of the average concentration under diffusive transport for the same local reaction. Thus, we consider the reactant to be described by a non-homogeneous concentration $c(x,t)$ depending on both position x and time t (see lower middle inset of Fig.1). We assume that the concentration is independent of the other spatial coordinates y and z over a reference surface S. This assumption is taken here for simplicity of analytical derivations, and can be relaxed to consider three dimensional transport processes following the same approach. The concentration is thus assumed to obey the diffusion-reaction equation,

$$\frac{\partial c}{\partial t} - D\frac{\partial^2 c}{\partial x^2} = -r(c), \tag{3}$$

where $D[L^2T^{-1}]$ is the diffusion coefficient, which we assume to be constant. The initial condition is taken as a rectangular pulse identical to the batch conditions, but the pulse is allowed to diffuse in an infinite one-dimensional domain.

At the boundaries, concentration tends to zero. Note that, in natural systems, boundaries limiting diffusive mass transfer would ultimately lead to a homogenization of the domain and a

convergence to the batch reaction rates. Our results hence describe the transient regimes before this happens. For a reference scale L larger than the pulse characteristic size, $L \gg \sqrt{Dt}$, the mean concentration is,

$$\overline{c} = \frac{M}{LS}. \tag{4}$$

The temporal evolution of the mean concentration is obtained by integrating Eq. (3) over space,

$$\frac{d}{dt}\overline{c}(t) = -\frac{k}{L}\int_{-L/2}^{L/2} dx\, c(x,t)^{\beta}. \tag{5}$$

Note that only the reaction term contributes directly to the change in mass, which can be shown by integration by parts. However, transport affects the shape of the concentration profile, and thus indirectly impacts the total mass and the average concentration. This one-dimensional diffusion-reaction approach is also relevant to understand the effect of plume stretching on reaction kinetics in heterogeneous media. Indeed, solutes transported in the subsurface tend to follow elongated lamella structures (Le Borgne et al., 2015) where concentrations vary weakly along the stretching direction and concentration gradients develop mostly in one-dimension transverse to lamellae (Fig. 1).

2.3 Non-dimensional units

In order to meaningfully compare the dynamics for different conditions, it is convenient to define non-dimensional quantities in terms of values characterizing the different physical processes at play. We define the non-dimensional position as $x_* = x/w_0$, where w_0 is the initial pulse width , the non-dimensional concentration as $c_* = c/c_0$, where c_0 is the initial concentration, and the non-dimensional average concentration as $\overline{c}_* = \overline{c}L/(c_0 w_0)$. Note that the non-dimensional initial concentration and average concentration are thus $c_*(0) = \overline{c}_*(0) = 1$. Furthermore, we define non-dimensional time as t/τ_R, where

$$\tau_R = \frac{1}{k c_0^{\beta-1}} \tag{6}$$

is the characteristic reaction time (inverse rate) associated with the initial concentration c_0. In the following, we drop the asterisk for notational brevity. All quantities discussed are non-dimensional in the sense discussed here unless mentioned.

In non-dimensional units, the kinetic equation for the batch is,

$$\frac{dc}{dt} = -c^{\beta}, \tag{7}$$

which can be solved with the initial condition $c(0) = 1$ to yield,

$$c(t) = [1 + (\beta - 1)t]^{-\frac{1}{\beta-1}}. \tag{8}$$

This solution holds whenever $\beta \neq 1$, that is, for nonlinear reactions. The special case of linear reactions leads to the classical $c(t) = e^{-t}$ exponential decay.

In order to account for the effect of dilution by mixing, we identify the time needed to homogenize the width of the initial condition as

$$\tau_D = \frac{w_0^2}{2D}, \tag{9}$$

corresponding to the time to homogenize a unit distance in nondimensional coordinates. The relative importance of reaction with respect to dilution is characterized by the dimensionless Damköhler number

$$\mathrm{Da} = \tau_D/\tau_R. \tag{10}$$

Fast reactions relative to dilution correspond to $\mathrm{Da} > 1$, while slow reactions correspond to $\mathrm{Da} < 1$. In nondimensional terms, the diffusion-reaction equation becomes

$$\frac{\partial c}{\partial t} - \frac{1}{2\mathrm{Da}}\frac{\partial^2 c}{\partial x^2} = -c^\beta. \tag{11}$$

Note that, in nondimensional variables, the initial condition is a rectangular pulse of unit width. The dimensionless total mass obeys

$$\frac{d}{dt}\overline{c}(t) = -\frac{1}{L}\int_{-L/2}^{L/2} dx\, c(x,t)^\beta. \tag{12}$$

All introduced parameters and their units are given in table 3 (Appendix A).

2.4

2.4 Numerical analysis

To explore the different effective reaction regimes, we first solved Eq. (11) numerically using Matlab's *pdepe* method, a numerical solver for one-dimensional partial differential equations (Skeel and Berzins, 1990). We use Neumann boundary conditions, i.e. no flux boundary condition, and a rectangular pulse of unit normalized width as initial condition (Fig. 1f). The domain size is chosen large enough to maintain close to zero concentrations at the domain boundaries at the end of the

2.5

simulation, and the grid discretization is refined to ensure the convergence of the solver. To analyze the effective kinetics at the pulse scale, that is for averaged concentrations over the solute pulse, we study the time evolution of the average concentration $\overline{c}(t)$ and the evolution of the effective reaction rate as a function of the average concentration.

We compare these numerical simulations to analytical solutions that we derived using the approximation discussed in the following section. Furthermore, we test these analytical predictions for one geochemically relevant example using the multi-component reactive transport model, CrunchFlow (version 1.0). Boundary and initial conditions for these simulations are described in the corresponding section. As for Matlab simulations, we use a domain large enough to ensure that the pulse does not reach the boundary and a grid discretization small enough to ensure convergence of the results.

3

2.1 Gaussian approximation for analytical derivations

When reactions are described by nonlinear local kinetics, transport and reaction interact in complex ways. Reaction impacts local concentration gradients, which in turn affect diffusive fluxes.

The latter leads to changes in the spatial concentration profile, which affects reaction. These interactions are captured by the diffusion-reaction equation (11). In order to better understand the interplay between reaction dynamics and dilution, and how it leads to different average kinetics compared to a well-mixed batch reactor, we develop an approximate analytical description of the average concentration, for a range of Damköhler numbers Da and reaction orders β.

In non-dimensional units, the initial condition is a rectangular pulse of unit finite width, identical with the batch conditions. Before diffusion has time to deform the pulse substantially, which is the case for times much smaller than the characteristic diffusion time τ_D, we expect the dynamics to be well-approximated by the batch kinetics, so that the average concentration approximately follows Eq. (8). This corresponds to $t \ll \mathrm{Da}$ in nondimensional terms. For non-dimensional times $t \gtrsim \mathrm{Da}$, diffusion has appreciably deformed the initial pulse. To derive analytical solutions for this problem, we approximate the reactive solute profiles as Gaussian distributions. This approximation is expected to be highly accurate for low Da when diffusion is faster at modifying the concentration distribution than reaction. It turns out to be also accurate in intermediate and high Da ranges (Appendix C), which facilitates an analytical solutions for the effective kinetics. The concentration distribution of reactive pulses is thus approximated as,

$$c(x,t) = \frac{M(t)}{\sqrt{2\pi\sigma^2(t)}} e^{-\frac{x^2}{2\sigma^2(t)}}, \tag{13}$$

where the variance $\sigma^2(t)$ and mass $M(t)$ evolve in time as a function of diffusion and reaction. Note that in the absence of reaction, the solution corresponds to $M(t) = 1$, and $\sigma^2(t) \propto t/\mathrm{Da}$.

Inserting Eq. (13) into Eq. (12), we obtain,

$$\frac{d}{dt}M(t) = -\frac{M(t)^\beta}{\sqrt{\beta}}[2\pi\sigma^2(t)]^{\frac{1-\beta}{2}}. \tag{14}$$

The Gaussian assumption allows second spatial derivatives in Eq. (11) to be estimated as,

$$\frac{\partial^2 c}{\partial x^2} = \left(-\frac{1}{\sigma^2} + \frac{x^2}{\sigma^4}\right) c, \tag{15}$$

hence, at $x = 0$, we have for the maximum concentration,

$$c(0,t) = \frac{M(t)}{\sqrt{2\pi\sigma^2(t)}}, \tag{16}$$

and for the second spatial derivative,

$$\frac{\partial^2 c}{\partial x^2}\Big|_{x=0} = -\frac{M(t)}{\sqrt{2\pi}\sigma(t)^3}. \tag{17}$$

Inserting Eq. (16) and (17) in Eq. (11) at $x = 0$, we obtain

$$\frac{d}{dt}\frac{M(t)}{\sqrt{2\pi\sigma^2(t)}} = -\frac{M(t)}{2\mathrm{Da}\sqrt{2\pi}\sigma(t)^3} - \frac{M(t)^\beta}{(2\pi)^{\beta/2}\sigma(t)^\beta}. \tag{18}$$

As discussed in Appendix B, Eq. (14) and (18) provide two independent equations to solve for the two unknowns $M(t)$ and $\sigma(t)$. Since the average concentration is proportional to the total mass (equation (4)), the dimensionless average concentration is equal to the dimensionless mass, $\overline{c(t)} = M(t)$. The accuracy of the Gaussian approximation is discussed in Appendix C.

3 Results

First, numerical simulations for the average concentration as a function of time for different values of β are presented for broad range of Damköhler numbers and reaction orders in order to demonstrate the resulting behavior and departure of the effective kinetics from the batch systems. As expected, for $\beta = 1$, the effective kinetics are equal to the batch kinetics (Fig. 2.b). For the other cases, the results can be generalized as:

- For$\beta < 1$, the average concentration of the pulse decreases faster than in the batch reactor, and the effective reaction rate of the pulse system is globally greater than the batch reactor (Fig. 2a).
- For $\beta > 1$, the average concentration of the pulse decreases more slowly than in the batch reactor and the effective reaction rate of the pulse injected system is globally less than the batch reactor (Fig. 2c-d).

4

Qualitatively, this effect may be understood as follows. For $\beta < 1$, the reaction is more efficient when distributing a given mass in the low concentration range because of the form of the kinetics (Eq. (1)). Dilution by diffusion accelerates the transfer of mass towards lower concentration values and thus enhances the average kinetics compared to the batch case.As a result, the time at which the average concentration goes to zero (Fig. 2.a) decreases with decreasing Da as dilution accelerates the effective kinetics. The opposite effect occurs for $\beta > 1$, leading to a reduction of the effective kinetics compared to batch kinetics. For the extreme case of $\beta > 3$, dilution retards the reaction to such a level that the average concentration converges asymptotically to a nonzero value (Fig. 2.d), with the asymptotic residual concentration increasing with decreasing Da.

The impact of dilution on reaction kinetics may be also understood by plotting the total reaction rate as a function of the average concentration (Fig. 3). For linear kinetics, the effective kinetics are identical to the batch kinetics independent of Da (Fig. 3.b). For low Da and $\beta < 1$, the global reaction rates are always greater than the batch for a given average concentration (Fig. 3.a). For low Da and $\beta > 1$, the global reaction rates are always less than the batch for a given average concentration (Fig. 3.c and Fig. 3.d). The difference between effective reaction kinetics and batch kinetics can reach several orders of magnitude. At low Damköhler numbers (Blue dots in Fig. 3) and quasi-constant average concentration, the variation in the reaction rates is substantial (an increase for $\beta < 1$ and a decrease for $\beta > 1$) . This counterintuitive regime is due to the action of diffusion , which distributes mass towards low concentration values, such that while the total reaction rate varies, the overall rate is insufficient to affect the total mass. At high Damköhler numbers (Green dots in Fig. 4) the effective rate first follows a batch-like behavior and then departs towards effective kinetics that are a function on β. In the following, we present our analytical results for the effective kinetics as a function of β.

3.1 Reaction order $\beta < 1$

For $\beta < 1$, the average concentration reaches zero at a finite time t_f (Fig. 4.a). For large Damköhler numbers, diffusion does not have time to induce significant dilution before $t = t_f$. Therefore, this time is identical to the time required to consume the full reactant mass in batch

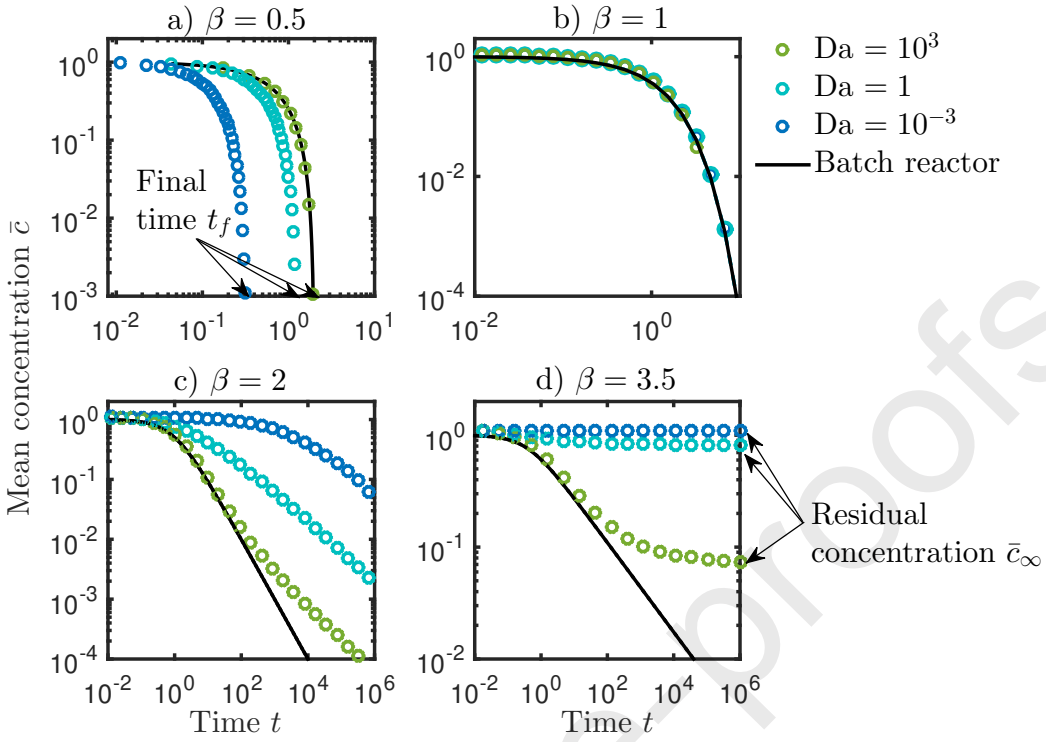

Figure 2: Average concentration in a reactive pulse as a function of time for a) $\beta = 0.5$, b) $\beta = 1$, c) $\beta = 2$ and d) $\beta = 3.5$. Numerical simulations for low, intermediate and high Da numbers (circles) are compared to batch kinetics (black solid line). The final time for full reactant consumption t_f, which occurs for $\beta < 1$, is indicated with arrows in figure a). The residual average concentration $\bar{c}_\infty$, which occurs for $\beta > 3$, is indicated with arrows in figure d). Note that the y-axis differs between panels to resolve the differences in concentration evolution.

reactions (Green dots and line in Fig. 4.a, Appendix B.2.1) :

$$t_f = \frac{1}{1-\beta}, \text{ for Da} > 1. \tag{19}$$

For low Damköhler numbers, using the assumption of a Gaussian concentration distribution, we obtain a solution for the evolution of the average concentration (Appendix B.1, Eq. (B.2)), in good agreement with numerical simulations (Blue dots and dashed lines in Fig. 4.a). This leads to the following estimate of t_f (Appendix B.1, Eq. (B.4)),

$$t_f \sim \text{Da}^{\frac{1-\beta}{3-\beta}}, \text{ for Da} < 1. \tag{20}$$

This scaling and the convergence to a constant value given by Eq. (19) at large Da are verified from numerical simulations in Fig. 4.b. The effect of dilution is thus to accelerate the effective kinetics, with a consumption time up to ten times less than predicted from the batch kinetics for Da $= 10^{-3}$.

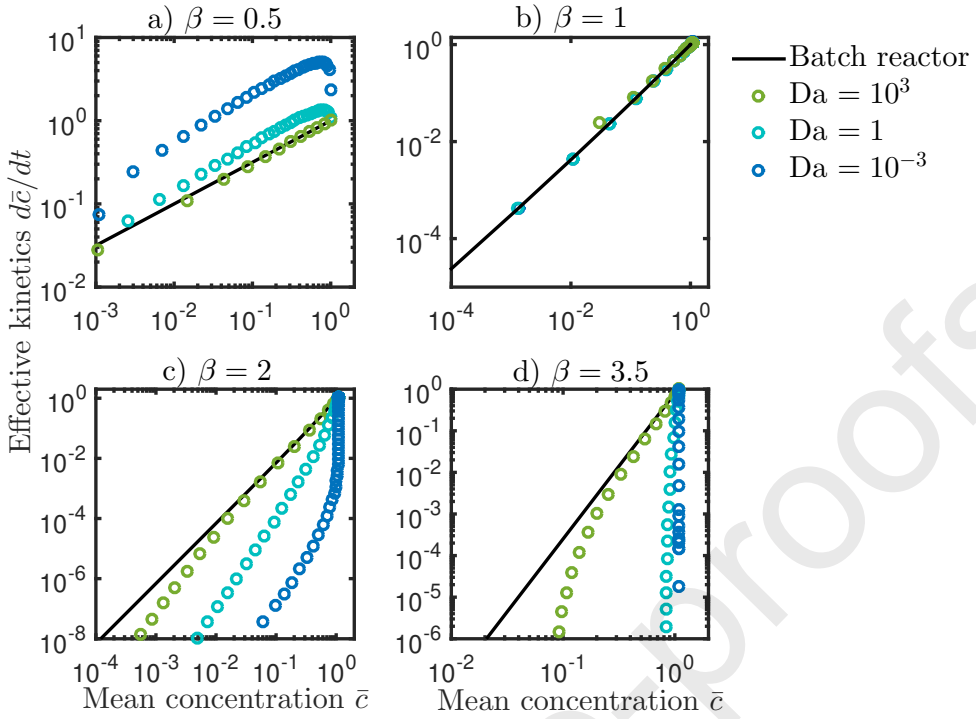

Figure 3: Effective kinetics of reactive pulses quantified as the rate of change of the mean concentration as a function of mean concentration for a) $\beta = 0.5$, b) $\beta = 1$, c) $\beta = 2$ and d) $\beta = 3.5$. Numerical simulations for low, intermediate and high Da numbers (circles) are compared to the batch reactor solution (black solid line). Note that the y-axis differs between panels to resolve the differences in concentration evolution.

3.2 Reaction order $1 < \beta < 3$

For $1 < \beta < 3$, we predict that the departure from the batch kinetics is not only a difference in the magnitude of the reaction but also in its order. The latter is shown by the power law scaling that relates the average reaction rate to the average concentration (dashed lines in Fig. 5), with an exponent that differs from the batch reaction order. For low Damköhler numbers, our solution implies that the average concentration decays in time as a power law (Appendix B.1, Eq. (B.6)),

$$\bar{c}(t) \sim t^{-\frac{3-\beta}{2(\beta-1)}}, \tag{21}$$

and the effective rate r_M follows (Appendix B.1, Eq. (B.9))

$$\frac{d\bar{c}}{dt} \sim \bar{c}^{\tilde{\beta}}, \tag{22}$$

with

the effective reaction order

$\tilde{\beta}$,

$$\tilde{\beta} = \frac{1+\beta}{3-\beta}. \tag{23}$$

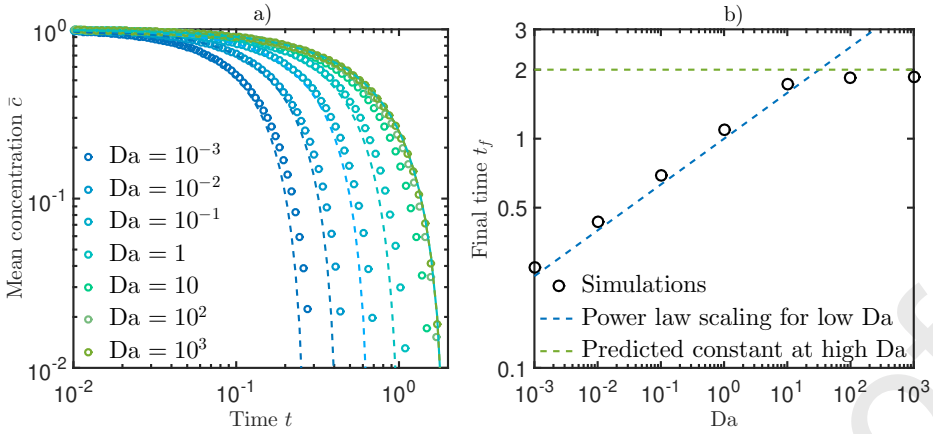

Figure 4: Effect of Damköhler on effective kinetics for $\beta = 0.5$, a) Average concentration as a function of time for several Damköhler numbers. Numerical results (dots) are compared to the analytical solutions of Eq. (B.2) (dashed lines). The batch solution is shown as a continuous line. b) Time t_f at which the mean concentration reaches zero as a function of Damköhler number. Black circles represents simulations, dashed lines represents the analytical predicions of Eq. (19) for low Damköhler numbers and Eq. (20) for high Damköhler number.

For high Damköhler numbers, two regimes occur (Fig. 8). The first regime, for $t < \mathrm{Da}$, follows the batch kinetics (Appendix B.2.1). In the second regime, for $t > \mathrm{Da}$, (Appendix B.2.2), the effective kinetics follow the same power law behavior as for low Damköhler number (Fig. 5.a) defined by Eq. (22).

These predictions are consistent with numerical simulations for all Damköhler numbers (Fig. 5.a) and all local reaction order β (Fig. 5.b). For low to intermediate Damköhler numbers, the effective kinetics follow the predicted power law kinetics, characterized by the effective reaction order $\tilde{\beta}$ for the full range of concentrations (Fig. 5.b). For large Damköhler numbers (green dots in Fig. 5.a) the effective kientic shows two regimes: a first regime following the batch kinetics given by Eq. (1) and a second power law regime given by Eq. (22). The difference between the effective and local reaction orders is largest for large reaction orders (Fig. 6). For $\beta = 1.5$, the effective order $\tilde{\beta} = 1.7$ is relatively close to the batch reaction order. Above $\beta = 1.5$, the effective order increases rapidly and is equal to $\tilde{\beta} = 3$ for $\beta = 2$. As β tends to 3, the deviation between the effective reaction order and the batch reaction order can become very large as the effective reaction order tends to infinity (Fig. 6).

3.3 Reaction order $\beta \geqslant 3$

For $\beta \geqslant 3$, the pulse reaction is much less efficient compared to a batch reactor, in the sense that the average reaction rate is smaller than in batch conditions for a given average concentration. For $\beta > 3$, dilution slows down the reaction so that the average concentration does not reach zero but converges to an asymptotic minimum value $\bar{c}_\infty$ (Fig. 7). For $\beta = 3$, the average concentration decays to zero logarithmically as $t \to \infty$ (Appendix B.1, Eq. (B.3)). Note that this behavior differs fundamentally from the lower reaction orders discussed above, for which the reaction rate is always larger than zero and there is no residual concentration, except for $\mathrm{Da} = 0$.

For low Damköhler numbers, the solution for the evolution of the mean concentration (Ap-

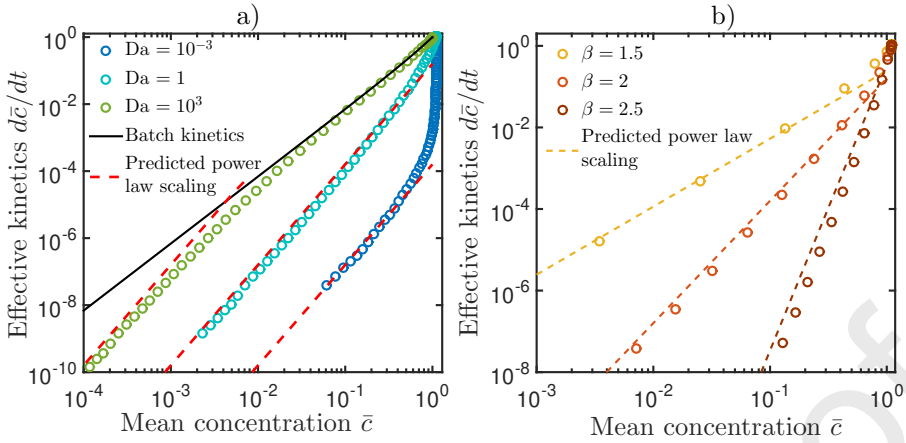

Figure 5: Effective kinetics in terms of mean concentration, a) $\beta = 2$, for Low, intermediate and high Da numbers, b) Da $= 1$ for different β in the range $1 < \beta < 3$. Numerical results (dots) are compared to analytical solutions (dashed lines). The power law behavior predicted by Eq. (22) is shown as a dashed line.

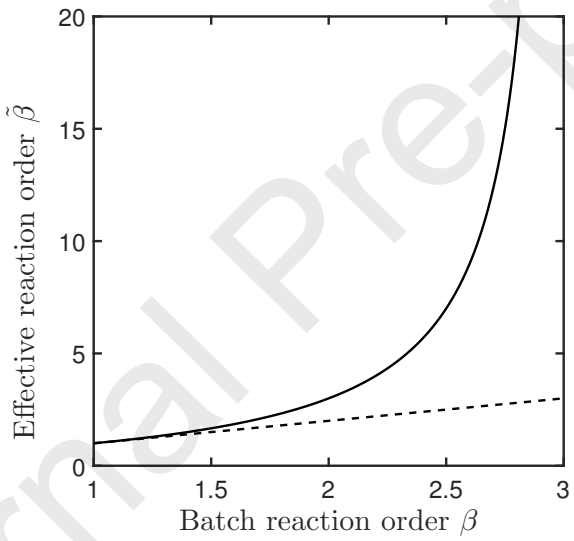

Figure 6: Effective reaction order $\tilde{\beta}$ predicted by Eq. (23) as a function of the batch reaction order for $1 < \beta < 3$ (solid line). The dashed line represents $\tilde{\beta} = \beta$.

pendix B.1, Eq. (B.2)) leads for $\beta > 3$ to an asymptotic value $\bar{c}_\infty$ such that (Eq. (B.5))

$$1 - \bar{c}_\infty \sim \mathrm{Da}. \tag{24}$$

As Da tends to zero, the asymptotic residual mean concentration tends to one (Fig. 7), which highlights the inhibiting effect of dilution on mass evolution for $\beta > 3$.

For high Damköhler numbers, the asymptotic residual mean concentration occurs in the

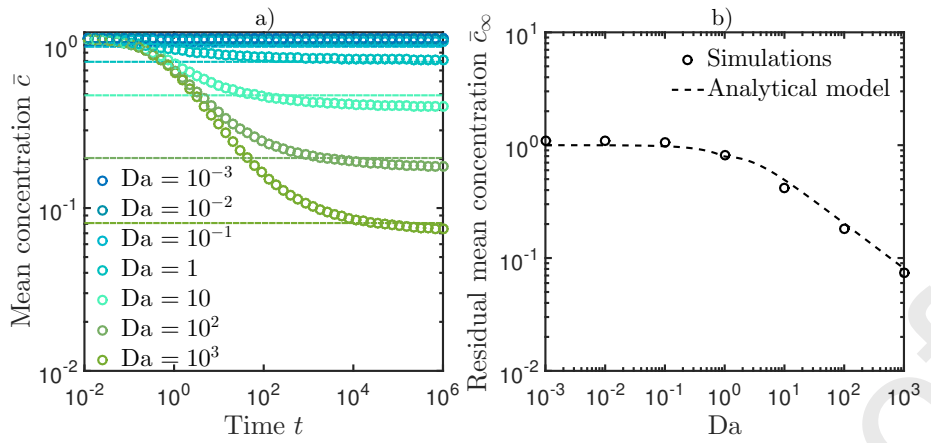

Figure 7: Effect of Damköhler on effective kinetics for $\beta = 3.5$, a) Numerical simulations (circles) as a function of time for different Damköhler number. Analytical model predictions for the asymptotic residual concentration are shown as dashed lines. b) Asymptotic residual mean concentration as a function of Damköhler number. Black circles represents simulations, the dashed black line represents the analytical model corresponding to Eq. (B.5) in Appendix B for low Damköhler numbers and to Eq. (25) for high Damköhler numbers.

second regime, leading to an asymptotic minimum value (Appendix B.2.2, Eq. (B.21))

$$\bar{c}_\infty \sim \mathrm{Da}^{-\frac{1}{\beta-1}}, \tag{25}$$

which again quantifies the inhibiting effect of dilution on reaction as Da increases. These analytical results closely match numerical simulations (Fig. 7.b).

4 Discussion

Our findings demonstrate that chemical gradients alter effective reactive kinetics through the coupling of diffusion and nonlinear reactions. By investigating the evolution of reactive solute pulses, as a paradigm for chemical gradients that evolve over space and time, we have uncovered a diverse spectrum of effective kinetic dynamics that depend on (1) the reaction nonlinearity (reaction order β) and (2) the relative importance of reaction and dilution quantified by the Damköhler number Da . A central conclusion of our study is that dynamic chemical gradients not only change the magnitude of the effective kinetic coefficient but also change the nature of the non-linearity compared to the local kinetics. This result is in contrast with previous studies that have studied how diffusive limitation, physical and geochemical heterogeneities (e.g. Soulaine et al., 2017; Wen and Li, 2017b; Deng et al., 2018), alter the effective kinetic coefficients, while keeping the same effective kinetic laws

4.1

as the local kinetics. While we have focused on simplified reaction kinetics to quantify and formalize this mechanism, these dynamics are expected to impact a large range of geochemical

systems where they are coupled to other processes. In the following, we discuss the relevance to common classes of biogeochemical reactions based on a synthesis of the results discussed above. Subsequently, we provide an example for a mineral dissolution reactions where rate discrepancies are commonly observed. However, the approach is also applicable to other types of reactions, including redox, precipitation, complexation and adsorption reactions, as discussed in the following section.

4.1 Characteristic persistence time of reactive pulses

To illustrate the consequences of the derived effective kinetics across a broad range of β and Da, we calculate the persistence time of reactive pulses that quantifies a characteristic time for the decay of the pulse mass under the effect of reaction. We define this time as a the time required for the pulse mass to reach a given fraction of the initial mass . To compare with the batch reactor, we divide it by the time it would take for a batch reactor to reach the same fraction of the initial mass. This normalized persistence time t_c is shown in Fig. 8 as a function of β and Da. We have taken here the fraction of the initial mass to calculate this time to be equal to 1%. Qualitatively similar results are obtained for other fractions. We have considered the full range of Damköhler numbers, from Da $= 10^{-3}$ (fast dilution compared to reaction) to Da $= 10^{3}$ (fast reaction compared to dilution). This covers a range of characteristic reaction times, that vary broadly depending on the type of reaction, and of transport time scales, which depend on the pulse size and species diffusion coefficient (Eq. (9)).

On the left-hand side of Fig. 8, for $\beta < 1$, reactants disappear on the order of ten times faster than in the batch in the low Damköhler range, which is consistent with the analytical estimate of t_f (Fig. 4). For $1 < \beta < 3$, the characteristic persistence time increases sharply with the non-linear reaction order β, reaching several orders of magnitude increase. This is due to the emergence of effective reaction orders $\tilde{\beta}$ that become much larger than the batch reaction order for increasing β (Fig. 6). Within the grey zone, for $\beta > 3$, residual mass persists indefinitely and the characteristic persistence time tends to infinity. Collectively, these findings imply that when concentration fields are heterogeneous the commonly used approach of coupling residence time to batch kinetics may underestimate/overestimate the persistence of reactants by orders of magnitude.

4.2

Our main analytical findings in the different quadrants of Fig. 8 provide a framework for assessing the impact of concentration gradients on effective kinetics for a given type of reaction, as discussed below.

4.2 Geochemical relevance of effective kinetics

Our results are strictly valid when the concentration of one element is spatially variable and the others are in excess in the fluid or in the mineral phase. This simplification isolates and formalizes the impact of transient concentration gradients on upscaled kinetics. In complex multi-component reactive system, this effect will act together with other known mechanisms, such as geochemical and physical heterogeneities, as well as multiple reactions. Although other processes will also contribute to the effective kinetics, we argue that the new phenomena described here will likely have a major contribution as it can alter reaction rates over orders of magnitude and modify the effective orders of reaction. For single step reactions, the reaction order β with respect to a given chemical species is equal to its stoichiometric coefficient. However, most

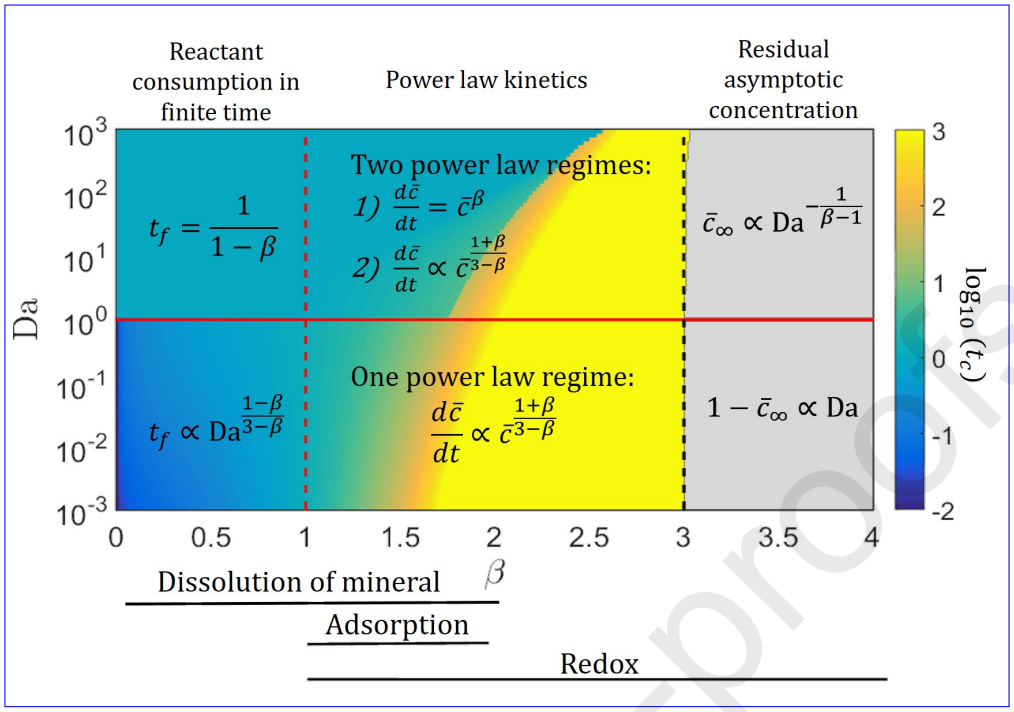

Figure 8: (Da, β) phase diagram of characteristic persistence time t_c and synthesis of main analytical results. The solid red line represents $\mathrm{Da} = 1$. The dashed red and black lines correspond respectively to $\beta = 1$ and $\beta = 3$. The color scale represents the time t_c needed for the mean concentration to reach 1% of initial mean concentration for the reactive pulses, normalized by the same time for the batch reactor. The main reaction enhancement occurs for $\beta < 1$ and $\mathrm{Da} < 1$ (blue area) while the effective reaction rate is strongly slowed down for $\beta > 1.5$ (yellow area). For $\beta > 3$, residual mass persists indefinitely and the characteristic persistence time may never be reached if the residual mass is larger than 1% (grey area). The typical range of effective reaction orders β for mineral dissolution, adsorption and redox reactions are indicated at the bottom.

biogeochemical reactions are complex multi-step reactions such that the rate-limiting step is unknown and hence most reaction orders are determined empirically and may range from 0 to 5.

The lower left hand side of Fig. 8 would be typical of silicate mineral dissolution where reactions involve multiple steps that can be effectively described by an adaptation of transition state theory (Aagaard and Helgeson, 1982; Lasaga et al., 1994; Steefel and Lasaga, 1994):

$$r = k \prod_{i=1}^{N} a_i^n \left(1 - \frac{Q}{K_{eq}}\right)^m, \tag{26}$$

where r is the overall rate, k is the intrinsic kinetic constant, a_i the ion activity, N the number of species, Q the ion activity product for the mineral-water reaction, and K_{eq} the corresponding equilibrium constant. The empirical exponents n and m introduce a non-linearity of the reaction rate with respect to the species concentration (Hellmann and Tisserand, 2006). Far from equilibrium, $Q \gg K_{eq}$ or $Q \ll K_{eq}$, and when a single species is limiting, equation (26) can be written as the simplified non-linear kinetics that we consider (equation (1)), with $\beta = n$. Effective reaction orders estimated from labo-

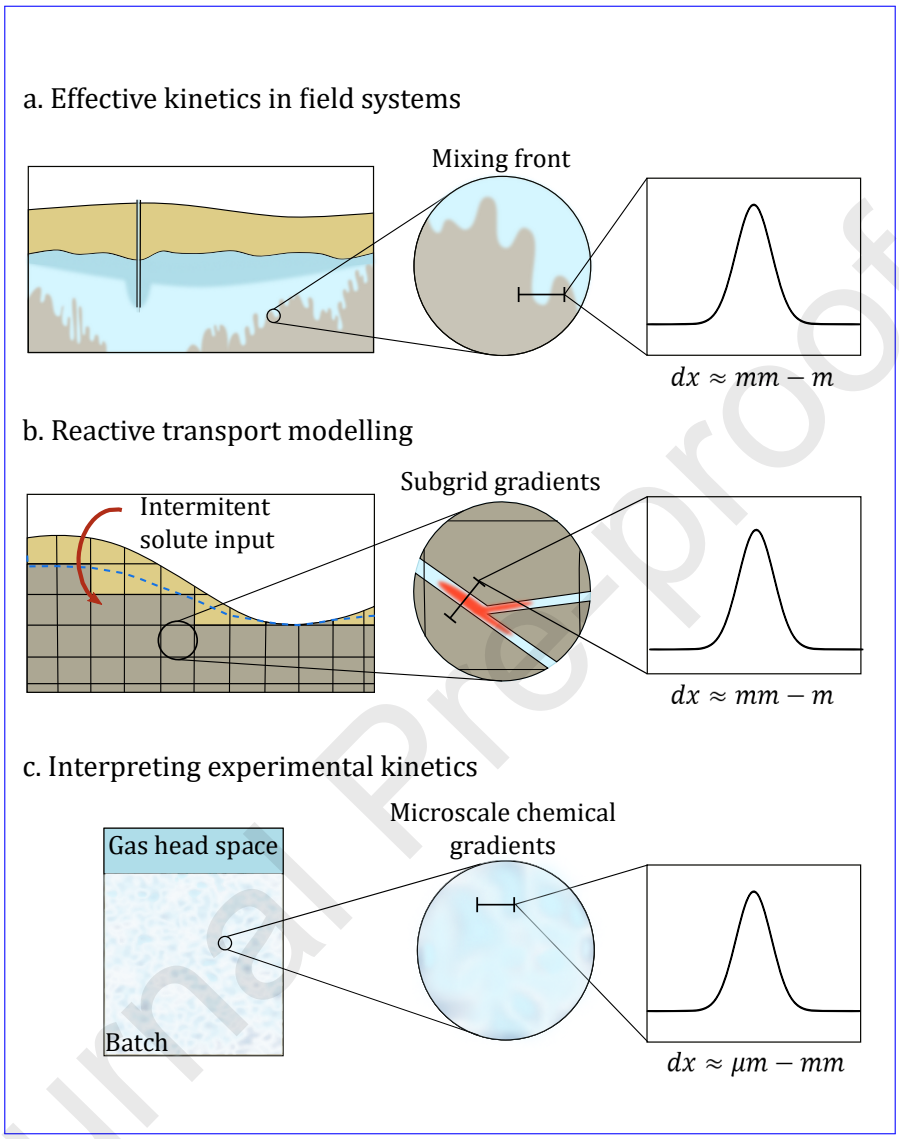

Figure 9: Illustration of different applications where unresolved chemical gradients may alter effective kinetics. a. Effective kinetics in field systems, such as CO_2 injection in the subsurface, where reactive pulses develop in mixing fronts. b. Reactive transport modeling, where subgrid chemical gradients cannot be resolved in models. c. Interpreting experimental kinetics in unmixed batches, where microscale chemical gradients can affect measured kinetics. The typical scales of expected chemical gradients for these applications is indicated as dx. textcolorblueUpdate the order of subfigures to match new order of section 5.

ratory experiments and typically range from $\beta = 0.1$ to 2 (Plummer and Wigley, 1976; Palandri and Kharaka, 2004) . Such mineral dissolution reactions are typically slow and therefore correspond to the low Da range. The upper right-hand sider region of Fig. 8 may be typical of redox reactios. Metal redox reactions are typically characterized by $1 \leqslant \beta \leqslant 4$, while other redox reactions tend to have lower orders $1 \leqslant \beta \leqslant 2$ (Bethke, 1996). Redox reactions involving organic matter may have orders as high as $\beta = 5$ (Bleam, 2017). In the middle region of Fig. 8, where t_c transitions rapidly, adsorption kinetics may be particularly susceptible to the effects observed here. Adsorption reaction kinetics are generally modelled with first-order or

4.3

pseudo-second-order kinetics (Rudzinski and Plazinski, 2006; Wu et al., 2009; Robati, 2013; Moussout et al., 2018) , which correspond to $\beta = 1$ or $\beta = 2$, but higher reaction orders are also observed (Largitte and Pasquier, 2016) .

The first application of our findings is for understanding the behavior of reactive solutes in field systems (Fig. 9a). As illustrated in Fig. 1, concentration gradients in natural systems can be driven by a diverse set of processes, ranging from intermittent sources to physical heterogeneity. For a given transport time, the reaction efficiency may be much faster (for $\beta < 1$) and much slower (for $\beta > 1$) than anticipated from batch kinetics (Fig. 8). This could lead to a much deeper penetration of reactive pulses or to a much faster consumption of solutes.

4.3

A second application is reactive transport modelling; to capture the effect of concentration gradients on reaction kinetics, reactive transport models should have a spatial resolution finer than the smallest scale of concentration gradients (Fig. 9 b). This is not possible for catchment scale applications (e.g. Li et al., 2017) but it is also challenging for modeling column experiments because chemical gradients often persist at the microscale (Heyman et al., 2020). Hence, our findings may help defining effective kinetics that quantify the impact of subscale gradients in reactive transport models. A third application is the interpretation of biogeochemical kinetics measured in experimental systems that are not well mixed, i.e. where chemical gradients persist (Fig. 9c). Geochemical reactions occurring at high temperatures and pressures, such as those associated with geologic carbon storage (e.g. DePaolo and Cole, 2013; Jun et al., 2013; Beckingham et al., 2016; Beckingham et al., 2017) , are often studied using batch reactors, where a gas headspace of a constant volume is used to maintain a constant pressure (Giammar et al., 2005; Johnson et al., 2014). Depending on the experimental conditions, pressure vessels can be difficult to mix via rocking or internal stirring, and are often static. Hence, in the absence of mechanical mixing, chemical gradients of different origin may develop, including dissolved gas convection, transport limitations and spatially heterogeneous reaction rates.

4.3 Example of the oxidation of pyrite by a pulse of dissolved oxygen

To illustrate these effective kinetics for a specific geochemical system, we take the example of pyrite dissolution by a pulse of dissolved oxygen. The aqueous oxidation of pyrite by oxygen is an example of geochemical process studied with reactive transport models to address a range of problems, including aquifer storage and recovery (Lazareva et al., 2015), acid mine drainage

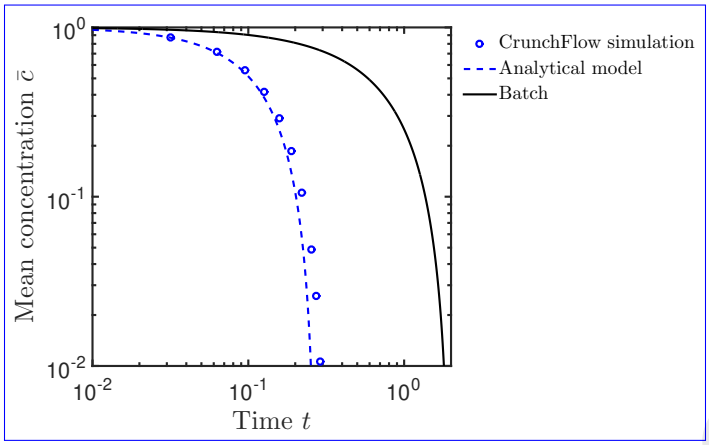

Figure 10: Simulation of pyrite dissolution by a pulse of dissolved oxygen for Da $= 10^{-3}$ ($\beta = 0.5$). Normalized mean concentration is shown as a function of normalized time, following the same definition as above. Results of the CrunchFlow simulation are shown as dots, the analytical model as a dashed line (Eq. B.2) and the batch model as a continuous line (Eq. B.11).

(Hubbard et al., 2009), and radioactive waste migration (Malmström et al., 2000; Yang et al., 2007). Intermittent release of dissolved oxygen, due to rainfall events or river stage variations (Fig. 1.a and 1.b), or flow heterogeneities (Fig. 1.e) often lead to small-scale dissolved oxygen gradients (Xu et al., 2000; Bochet et al., 2020) that are typically not resolved by reactive transport models. The reaction of oxidation of pyrite by oxygen can be written as

,

$$\mathrm{FeS_2} + \tfrac{7}{2}\,\mathrm{O_2} + \mathrm{H_2O} \longrightarrow \mathrm{Fe^{2+}} + 2\,\mathrm{SO_4^{2-}} + 2\,\mathrm{H^+}$$

Assuming that the other species are in excess, the kinetic rate law for pyrite oxidation by oxygen may be written with respect to oxygen as (McKibben and Barnes, 1986)

$$\frac{1}{3.5}\frac{dc_{O_2}}{dt} \approx -k c_{O_2}^{0.5}, \tag{27}$$

corresponding to $\beta = 0.5$.

For the geochemical system considered here, the kinetics of subscale unresolved oxygen pulses would be faster than predicted by batch kinetics (Fig. 8). For instance, assuming a Damköhler number of 10^{-4}, resulting from a kinetic rate constant of 6.6×10^{-9} mol/m^2/s (Yang et al., 2007) and a diffusion coefficient of 10^{-9} mol/m^2/s (Jung and Navarre-Sitchler, 2018a), dissolved oxygen would be consumed 10 times faster than it would be in the well-mixed homogeneous system. The more rapid release of both Fe^{2+} and trace metals typically associated with pyrite (i.e., As, Pb, etc.) may have further implications for water quality. Although our results imply that kinetic rates used in reactive transport models of systems with sub-grid scale concentrations will be subject to additional uncertainty, our approach provides a concrete means of evaluating the range of kinetic parameters to enable robust sensitivity analysis or uncertainty quantification (e.g. Fenwick et al., 2014; Song et al., 2015).

We have verified that this geochemical system can be accurately modeled by our framework under the considered assumptions (Fig. 10) using the multi-component reactive transport model CrunchFlow (Steefel et al., 2015). We first consider the case of a single pulse. The system is composed of pyrite with a porosity of 30% and dissolution kinetic constant $k = 10^{-8.31}$

Table 1: Initial and injection chemistry used in CrunchFlow simulations for a single pulse, pyrite dissolution

Species	Initial condition (mol/L)	Injection condition (mol/L)
Fe^{2+}	10^{-8}	10^{-8}
H^+	10^{-4}	10^{-4}
$O_{2,aq}$	10^{-11}	10^{-4}
SO_4^{2-}	10^{-8}	10^{-8}
Cl^-	Equilibrates charge	Equilibrates charge

m mol^{-1} s^{-1} (Yang et al., 2007). The considered solute species are $O_{2,aq}$, Fe^{2+}, SO_4^{2-}, and H^+. For the initial condition in the domain prior to injection, the species concentrations are $c_{O_2} = 10^{-11}$ mol/L, $c_{Fe^{2+}} = 10^{-8}$ mol/L, $c_{SO_4^{2-}} = 10^{-8}$ mol/L, and pH is 4. Chloride is designated as the charge balancing ion to maintain electroneutrality. In the injected pulse, concentrations are the same as in the domain except for the oxygen concentration is set as $c_0 = 10^{-4}$ mol/L (Bochet et al., 2020, Table 1). The simulations were performed at 25°C with a diffusion coefficient of 10^{-7} m^2 s^{-1} (Elberling et al., 1994), leading to Da $= 10^{-3}$ (Table 2). The CrunchFlow simulation is in good agreement with the analytical model (Fig. 10). As predicted, the average concentration reaches zero much faster than the batch.

In order to evaluate the effect of a non-ideal concentration profile, we performed a CrunchFlow simulation with five irregularly spaced pulse injections of width 10^{-2} m each, with different initial oxygen concentrations ($log(c_{O_2}) = -4, -5, -6, -7, -8$) (Table 2). The initial conditions are the same as in the single pulse case (Table 1) and all the injected concentrations except oxygen are the same as in the background domain. The equivalent batch is defined with initial concentration equal to the mean of the pulse initial concentrations. The parameters are adapted to the single-pulse analytical model with an equivalent pulse width equal to the sum of the pulse widths, and an equivalent initial concentration set as the mean of injection concentrations, resulting in Da= 5 10^{-2} (Table 2). In this case, the match with the analytical prediction remains excellent (Fig. 11) even though the concentration distribution is more complex than assumed in the analytical derivations.

5 Conclusions

The effective kinetics of reactive pulses reveal a rich diversity of behaviors driven by the interplay between dilution and non-linear reaction (Fig. 8). In the presence of concentration gradients, diffusion acts to redistribute mass towards lower concentrations, which, when coupled with non-linear reactions, can either enhance or inhibit the reaction efficiency depending on the local reaction order. We have derived approximate analytical solutions that capture these reactive dynamics and predict the different effective kinetic laws as a function of Damköhler number and the reaction order, which are representative of a range of reactive transport systems (Fig. 1, 8 and 9). An important consequence of our results is the emergence of new effective kinetic laws characterized by upscaled orders that can be very different from those of the local kinetics. The coupling of transient concentration gradients and non-linear reactions hence leads to effective

Table 2: Parameters of the analytical model for the pyrite dissolution case.

Parameter	w_0	D	c_0	ν	k	A	Φ	τ_D	τ_R	Da
Unit	m	m^2/s	mol/L	[–]	[unit]	m^2/m^3	[–]	[–]	[–]	[–]
Single pulse $\beta = 0.5$	10^{-2}	10^{-7} [a]	10^{-4} [b]	3.5	$4.8\ 10^{-9}$ [c]	350	0.3	$1.6\ 10^{-5}$	$1.6\ 10^{-2}$	10^{-3}
Several pulses $\beta = 0.5$	10^{-2}	10^{-7}	10^{-4} 10^{-5} 10^{-6} 10^{-7} 10^{-8}	3.5	$4.8\ 10^{-9}$	350	0.3	$4\ 10^{-4}$	$7.5\ 10^{-3}$	$5\ 10^{-2}$

[a] (Elberling et al., 1994)
[b] (Bochet et al., 2020)
[c] (Yang et al., 2007)

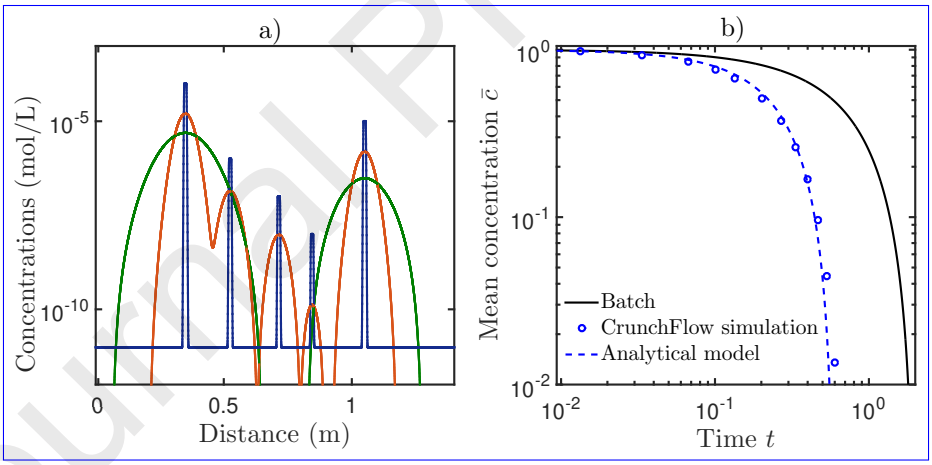

Figure 11: Simulation of pyrite dissolution by multiple pulses of dissolved oxygen ($\beta = 0.5$). Five pulses with different initial concentrations and irregularly spaced are injected in the domain. a) is the concentration profile in space at normalized time $t \approx 10^{-5}$ (blue), $t \approx 10^{-2}$ (orange), $t \approx 10^{-1}$ (green). b) the normalized mean concentration as a function of normalized time for the CrunchFlow simulation (dots), an equivalent batch system (with initial concentration equal to the mean of injected concentrations Eq. (B.11), continuous line), and an equivalent analytical model (considering one pulse with initial concentration equal to the mean of injected concentrations, Eq. (B.2), dashed line), thus corresponding to Da = $5\ 10^{-2}$.

kinetics that can be much more non-linear than the batch kinetics (Fig. 6).

To isolate this mechanism and derive approximate analytical solutions for the effective kinetics, we considered here the idealized case of reactive pulses evolving through diffusion and reaction. In complex natural reaction networks, this effect acts together with a range of other processes and therefore it is difficult to understand and quantify. Other important phenomenon known to impact the effective kinetics include the limited access of solutes to reactive surfaces and mixing limitations, due to physical and geochemical heterogeneity at the pore or Darcy scale (Molins et al., 2014; Beckingham et al., 2017; Wen and Li, 2018; Jung and Navarre-Sitchler, 2018a; Valocchi et al., 2
. In multi-components systems, our results are strictly valid when one element is varying in space and time and the others are in excess. In natural systems several elements may be spatially variable and react with different orders leading to more complex behaviour. However, since the effect that we have uncovered leads to orders of magnitude differences between batch and effective reaction rates, it is likely playing a major, and so far unappreciated, role in multi-component systems.

Although we explicitly solve the system for the ideal case of pulses, our general findings are expected to apply qualitatively to different types of concentration landscapes. Indeed, in the presence of concentration inhomogeneities, induced by intermittent reactant release or physical heterogeneity (Fig. 1), diffusion tends to redistribute mass towards lower concentrations, which leads to reaction enhancement or inhibition depending on the local reaction order β as described here. The derived analytical framework is an essential step to integrate a range of biogeochemical reactions in new mixing theories that describe the statistics of concentration gradients (Le Borgne et al., 2017). The lamella mixing theory was successfully used to predict the upscaled kinetics of mixing-driven reactions at pore scale (De Anna et al., 2014b) and Darcy scale (Le Borgne et al., 2014; Bandopadhyay et al., 2018) by coupling the one-dimensional compression-diffusion equation transverse to stretched solute lamellae with bi-molecular reactions in the fluid phase. By solving explicitly the coupling of diffusion and non-linear reactions , the method presented here resolves the main difficulty for the development of a reactive lamella framework to upscale the effective kinetics of a range of non-linear reactions under incomplete mixing conditions, including fluid-solid reactions.

These findings would thus be useful to interpret the result of reactive experiments in which subscale chemical gradients develop due to poor mixing. These analytical results may also be used to guide reactive transport models that cannot fully resolve the scale of concentration gradients, which occurs in many reactive transport problems. Finally, they provide a new framework to understand the effect of concentration gradients on chemical reactions in field applications, in particular to understand the possible longer/smaller persistent time or penetration length of reactive solutes. These findings indeed suggest that the characteristic persistence time of biogeochemical pulses can differ by orders of magnitude from the predictions of models that couple solute residence time with batch kinetics. Reactive pulses are consumed much faster when the order of the reaction is less than one, whereas they persist for a much longer time when the order of the reaction is larger than one. These effects are particularly important at low Damköhler number i.e., for reactions that are slow compared to the characteristic diffusion time. For orders of reaction larger than three, dilution slows down reaction to the point that a residual mass persists asymptotically.

Acknowledgments

CLT and TLB gratefully acknowledge funding by the ERC under the project *ReactiveFronts* 648377. CLT would like to thank also l'Ecole des Docteurs de l'UBL, le Conseil Regional de

Bretagne and OZCAR-RI for supporting this work. TA is supported by a Marie Skłodowska Curie Individual Fellowship, under the project *ChemicalWalks* 792041. CB acknowledges funding from Region Bretagne and Rennes Metropole.

Appendix A Notations

We detail all notations used in the study in table 3.

Appendix B Analytical solutions

This appendix details the analytical derivations for effective kinetics under coupled diffusion and non-linear reactions based on the assumption of Gaussian distribution of the reactant (Eq. (13)) for $t \gg \mathrm{Da}$ and of negligible diffusion for $t \ll \mathrm{Da}$. The validity of these assumptions is discussed in Appendix C. The cases of low and high Damköhler are detailed separately below.

B.1 Low Damköhler number

In the limit of low Da, diffusion quickly deforms the pulse into a Gaussian distribution (Eq. (13)), whose variance evolves diffusively (see Appendix C and Fig. C.3),

$$\sigma^2(t) \approx \frac{t + \mathrm{Da}/12}{\mathrm{Da}}, \tag{B.1}$$

where we have set $\sigma^2(0) = 1/12$ to match the variance of the initial rectangular profile. Inserting Eq. (B.1) into (14), we obtain

$$M(t) = \left[M_i - \frac{2}{\sqrt{\beta}} \frac{1-\beta}{3-\beta} \left(\frac{2\pi}{\mathrm{Da}} \right)^{\frac{1-\beta}{2}} \left[(t+\mathrm{Da})^{\frac{3-\beta}{2}} - \mathrm{Da}^{\frac{3-\beta}{2}} \right] \right]^{\frac{1}{1-\beta}}, \tag{B.2}$$

with the initial mass $M_i \approx M(0) = 1$. Note that for $\beta = 1, 3$ this solution is singular and is not valid. For linear kinetics, $\beta = 1$, the concentration profile is exactly Gaussian, and the total mass decays exponentially. For $\beta = 3$, combining Eq. (14) and Eq. (B.1), and carrying out the integration explicitly, we obtain

$$M_{\beta=3}(t) = \left[1 + \frac{\mathrm{Da}}{\sqrt{3\pi^2}} \log\left(1 + \frac{12t}{\mathrm{Da}} \right) \right]^{-1/2}, \tag{B.3}$$

which decays to zero logarithmically as $t \to \infty$.

Since the average concentration is proportional to the total mass (equation (4)), the dimensionless average concentration is equal to the dimensionless mass, $\overline{c(t)} = M(t)$. When $\beta < 1$, the mass reaches zero in a finite time according to Eq. (B.2), given to leading order in Da by

$$t_f = \left(\frac{\sqrt{\beta}}{2} \frac{3-\beta}{1-\beta} \right)^{\frac{2}{3-\beta}} \left(\frac{\mathrm{Da}}{2\pi} \right)^{\frac{1-\beta}{3-\beta}}. \tag{B.4}$$

For $\beta > 3$, the mass converges from above to an asymptotic minimum value according to Eq. (B.2). To leading order in Da, this gives,

$$\bar{c}_\infty = 1 - \frac{2\mathrm{Da}}{\sqrt{\beta}(\beta-3)(2\pi)^{\frac{\beta-1}{2}}}. \tag{B.5}$$

Table 3: Definition of model parameters and units

Parameter	Definition	Units
r	Reaction rate	mol $L^{-\mathrm{d}}$ T^{-1}
c	Concentration	mol $L^{-\mathrm{d}}$
c_0	Initial concentration	mol $L^{-\mathrm{d}}$
$\overline{c}$	Mean concentration	mol $L^{-\mathrm{d}}$
$\overline{c}_\infty$	Normalized residual mean concentration, [–]	
β	non-linear power law exponent	[–]
$\tilde{\beta}$	Power law exponent of the effective kinetic	[–]
k	reaction rate constant	$\mathrm{mol}^{1-\beta} L^{\mathrm{d}(\beta-1)}$ T^{-1}
D	Diffusion coefficient	L^2 T^{-1}
Da	Damköhler number	[–]
L	Characteristic length	L
M	Mass	kg
S	Reference surface	L^2
w_0	Initial width	L
σ	Normalized variance	[–]
t	Time, normalized time	T, [–]
t_c	Normalized persistence time	[–]
t_f	Normalized final time, $\beta < 1$	[–]
τ_D	Diffusion characteristic time	T
τ_R	Reaction characteristic time	T
u	Fluid velocity	L T^{-1}
V	Volume of the batch	L^3
x	Distance	mol $L^{-\mathrm{d}}$ T^{-1}

For $1 < \beta < 3$, Eq. (B.2) follows a power-law decay, which leads to the average concentration,

$$\overline{c}(t) \approx \sqrt{\frac{2\pi}{\mathrm{Da}}} \left(\frac{\sqrt{\beta}}{2} \frac{3-\beta}{\beta-1} \right)^{\frac{1}{\beta-1}} t^{-\frac{3-\beta}{2(\beta-1)}}, \tag{B.6}$$

for $t \gg \mathrm{Da}$.

Differentiating Eq. (B.6), we find

$$\frac{d}{dt}\overline{c}(t) = -\frac{3-\beta}{2(\beta-1)} \frac{\overline{c}(t)}{t}, \tag{B.7}$$

Because the average concentration decreases monotonically, $\overline{c}(t)$ is invertible, Solving Eq. (B.6) for time as a function of mean concentration, we have

$$t(\overline{c}) = \left(\frac{2\pi}{\mathrm{Da}} \right)^{\frac{\beta-1}{3-\beta}} \left(\frac{\sqrt{\beta}}{2} \frac{3-\beta}{\beta-1} \right)^{\frac{2}{3-\beta}} \overline{c}^{-\frac{2(\beta-1)}{3-\beta}}. \tag{B.8}$$

Thus, the effective kinetics are given by

$$\frac{d}{dt}\overline{c}(t) = \beta^{-\frac{1}{3-\beta}} \left(\frac{\mathrm{Da}}{\pi} \frac{\beta-1}{3-\beta} \right)^{\frac{\beta-1}{3-\beta}} \overline{c}^{\frac{1+\beta}{3-\beta}}. \tag{B.9}$$

B.2 High Damköhler number

We now develop an approximate description for the behavior of the average concentration at high Damköhler. This involves two different regimes.

B.2.1 First regime, $t \ll \mathrm{Da}$

First, for times $t \ll \mathrm{Da}$, diffusion has not had time to significantly deform the initial condition. Thus, the average concentration evolves approximately according to the batch dynamics,

$$\frac{d\overline{c}(t)}{dt} = -\overline{c}(t)^{\beta}, \tag{B.10}$$

and we obtain

$$\overline{c}(t) = [1 + (\beta-1)t]^{-\frac{1}{\beta-1}}. \tag{B.11}$$

For $\beta < 1$, the average concentration reaches zero during this regime at the time given by Eq. (19).

B.2.2 Second regime, $t \gg \mathrm{Da}$,

For $t > \mathrm{Da}$, the spreading of the pulse by diffusion cannot be neglected. Rearranging Eqs. (14) and (18), we obtain for the variance

$$\frac{d\log\sigma(t)}{dt} = \frac{1}{2\mathrm{Da}\sigma^2(t)} - (\sqrt{\beta}-1)\frac{d\log M(t)}{dt}. \tag{B.12}$$

If the first term on the right hand side of Eq. (B.12) dominates compared to the second term, the evolution of the variance is approximately diffusive. Otherwise, if the second term dominates,

the evolution of the variance is driven by the effect of reaction. Inserting Eq. (B.11) into (B.12), the condition for diffusion-dominated growth is thus

$$\sigma(t)^{3-\beta}M(t)^{\beta-1} < \frac{\sqrt{\beta}-1}{\sqrt{\beta}}\frac{(2\pi)^{\frac{\beta-1}{2}}}{2\mathrm{Da}}. \tag{B.13}$$

We start by evaluating this inequality at $t = \mathrm{Da}$, which is the onset of this second regime. Since mass follows the batch dynamics in the first regime (Eq. (B.11)), at $t = \mathrm{Da}$, it is given by

$$M(\mathrm{Da}) = [1 + (\beta-1)\mathrm{Da}]^{-\frac{1}{\beta-1}}. \tag{B.14}$$

We substitute Eq. (B.14) and $\sigma(\mathrm{Da}) = 1/12$ (corresponding to the initial variance of a rectangular pulse, assumed not to change appreciably up to $t = \mathrm{Da}$) in Eq. (B.13), which gives the condition for a dominant diffusive variance growth at $t = \mathrm{Da}$,

$$\frac{2\mathrm{Da}}{(2\pi)^{\frac{\beta-1}{2}}}\frac{\sqrt{\beta}-1}{\sqrt{\beta}}\frac{12^{-\frac{3-\beta}{2}}}{1+(\beta-1)\mathrm{Da}} < 1. \tag{B.15}$$

For a given β, the left hand side of Eq. (B.15) is largest for $\mathrm{Da} \to \infty$. Therefore, if the criterion holds in this limit, it holds for all Da. In this limit, the condition is

$$\frac{2}{\sqrt{\beta}(\sqrt{\beta}+1)(2\pi)^{\frac{\beta-1}{2}}12^{\frac{3-\beta}{2}}} < 1. \tag{B.16}$$

This holds for $\beta \lesssim 5$, as verified numerically. We focus on such β since higher β are not commonly encountered. Therefore, at $t = \mathrm{Da}$, the variance growth is dominated by diffusion for the range of β that we consider, leading to a variance equal to

$$\sigma^2(t) \approx \sigma^2(\mathrm{Da}) + \frac{t-\mathrm{Da}}{\mathrm{Da}}, \tag{B.17}$$

with $\sigma^2(\mathrm{Da}) = 1/12$, and a mass given by the same equation as for the low Da regime, with the initial mass $M_i \approx M(\mathrm{Da})$, see Eq. (B.2). To test whether the criterion of diffusion dominated variance holds true at larger times, we substitute Eq. (B.17) and Eq. (B.2) in Eq. (B.13). This gives the criterion

$$\frac{2\mathrm{Da}}{(2\pi)^{\frac{\beta-1}{2}}}\frac{\sqrt{\beta}-1}{\sqrt{\beta}}\frac{\left[\frac{1}{12}+\frac{t-\mathrm{Da}}{\mathrm{Da}}\right]^{\frac{3-\beta}{2}}}{M(\mathrm{Da}) - \frac{2}{\sqrt{\beta}}\frac{1-\beta}{3-\beta}\left(\frac{2\pi}{\mathrm{Da}}\right)^{\frac{1-\beta}{2}}\left[(t+\mathrm{Da})^{\frac{3-\beta}{2}} - \mathrm{Da}^{\frac{3-\beta}{2}}\right]} < 1. \tag{B.18}$$

It can be verified numerically that this criterion holds true at all times. For $t \to \infty$, this simplifies into

$$\frac{3-\beta}{\sqrt{\beta}+1} < 1, \tag{B.19}$$

which is always true for $\beta > 1$. Hence, the variance evolves diffusively at $t = \mathrm{Da}$ and at all later times, and a regime with reaction-dominated variance growth is never observed. The accuracy of the growth of the variance according to Eq. (B.17) is discussed in Appendix C.

The effective kinetics can thus be derived as follows for different β. For $1 < \beta < 3$, the effective kinetics remain given by Eq. (B.9), and the average concentration by Eq. (B.6) with $M_i = M(\mathrm{Da})$ (Eq. (B.14)). For $\beta > 3$, according to Eq. (B.11) after replacing the initial mass M_i by $M(\mathrm{Da})$, the mass tends to an asymptotic constant value given by

$$M_\infty = \left[M(\mathrm{Da}) + \mathrm{Da}\frac{2}{\sqrt{\beta}}\frac{\beta-1}{\beta-3}(2\pi)^{-\frac{\beta-1}{2}}\right]^{-\frac{1}{\beta-1}}. \tag{B.20}$$

At sufficiently large Da, we can neglect $M(\mathrm{Da})$ according to Eq. (B.14) because $\mathrm{Da}^{-\frac{1}{\beta-1}} \ll \mathrm{Da}$. Thus, we obtain the asymptotic value for the average concentration,

$$\bar{c}_\infty \approx \mathrm{Da}^{-\frac{1}{\beta-1}} \sqrt{2\pi} \left(\frac{\sqrt{\beta}}{2} \frac{\beta-3}{\beta-1} \right)^{\frac{1}{\beta-1}} . \tag{B.21}$$

Appendix C Hypothesis validation

In addition to the numerical validation of the analytical derivation for the effective kinetics, we further test the validity of the assumptions that we use in our analytical derivations. The Gaussian assumption and the variance growth assumptions are discussed separately below.

C.1 Gaussian assumption

Here we assess the validity of the Gaussian assumption for different Damköhler numbers at times corresponding to different regimes. As highlighted by Eq. (13), Gaussian distributions of different widths σ and maximum value c_{peak} collapse to a single curve when represented according to the normalized variables x/σ and c/c_{peak}. It is thus convenient to use this normalization to test the Gaussian assumption. Furthermore, Gaussian curves are uniquely characterized by the power law scaling

$$\log(c/c_{peak}) \sim (x/\sigma)^{-2} . \tag{C.1}$$

Therefore, Gaussian distributions are characterized by a straight line of slope 2 when representing $\log(|\log(c/c_{peak})|)$ against $\log(|x/\sigma|)$. Hence, any deviation from this slope corresponds to a non-Gaussian profile.

In Fig. C.1, we test the Gaussian assumption in the case of $\beta = 2$ for low and high Damköhler numbers, respectively $\mathrm{Da} = 10^{-3}$ and $\mathrm{Da} = 10^{3}$. At low Da, diffusion acts over much smaller time scales than reaction, and the profiles are Gaussian at all times (Fig. C.1.a and c), consistently with the hypothesis of Appendix B.1. For high Da, the early time profiles are non Gaussian and close to the initial square injection (Fig. C.1.b and d). In this regime, we do not assume Gaussianity but instead the dominance of reaction over diffusion (Appendix B.2.1). At late times, $t \gg \mathrm{Da}$, the profiles are very close to Gaussian (Fig. C.1.a and C.1.b) and closely follow the power law scaling of Eq. (C.1) (Fig. C.1.b and d), which is consistent with the assumption of Appendix B.2.2.

In Fig. C.2, we test the Gaussian assumption for the case of $\beta = 0.5$ for low Damköhler number, $\mathrm{Da} = 10^{-3}$. We do not represent large Da in Figure C.2 because mass reaches zero before $t = \mathrm{Da}$ in this case and only the first regime where we do not assume Gaussianity (Appendix B.2.1) is relevant. Again, consistently with the assumption of Appendix B.1, for low Da, the profiles are very close to Gaussian at all times (Fig. C.2.a) and closely follows the power law scaling of Eq. (C.1) (Fig. C.2.b). Results are similar for other reaction orders $\beta < 1$.

These results confirm the assumptions that we have made in Appendix B for deriving approximated analytical solution for the evolution of concentration distributions. For $t \ll \mathrm{Da}$, we dot not assume that profiles are Gaussian but we assume that diffusion plays no role and that the evolution of concentration profiles is dominated by reaction alone. For small Da, this regime is very short and not considered here. For large Da, this regime is discussed in Appendix B.2.1. For $t \gg \mathrm{Da}$, we assume that profiles are Gaussian, which is consistent with numerical simulations for all values of Da and β. This regime is discussed in Appendix B.1 and B.2.2.

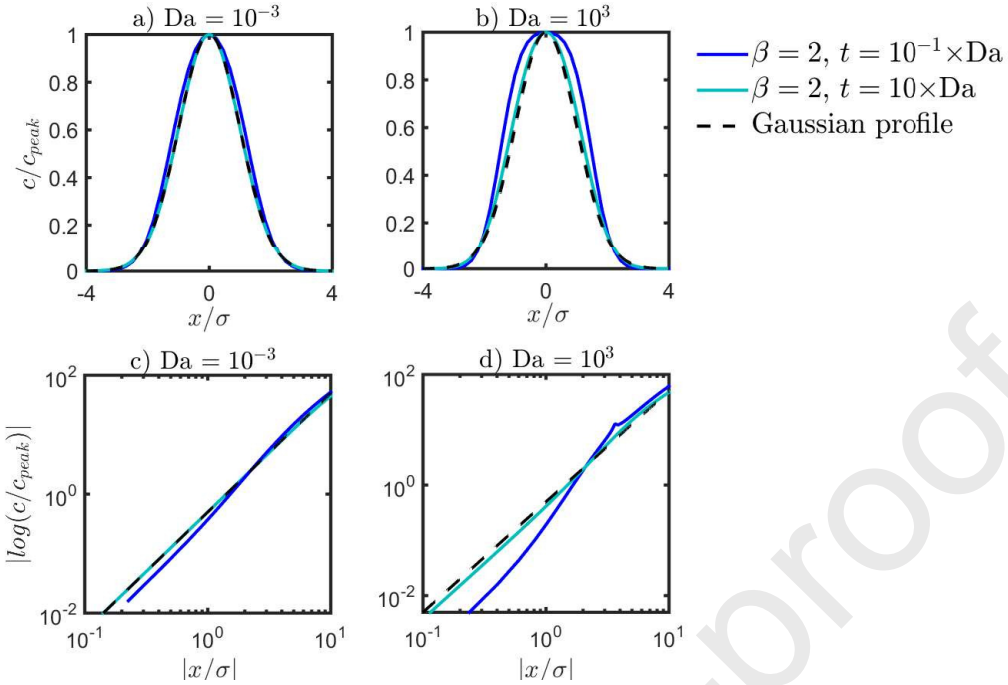

Figure C.1: Test of Gaussianity of reactive pulses from numerical simulations for $\beta = 2$. Comparison of reactive profiles, normalized by their peak values c_{peak} along the y axis and their standard deviation σ along the x axis, with Gaussian profiles at early and late times, respectively $t \approx 10^{-1} \times$ Da and $t \approx 10 \times$ Da for a) Da $= 10^{-3}$, and b) Da $= 10^{3}$. Test of Gaussian power law scaling (Eq. (C.1)) for the same cases respectively for c) low Da and d) high Da.

C.2 Variance growth assumption

Here, we assess the validity of the assumption that the evolution of the variance is dominated by the diffusion term in Eq. (B.12). This leads to the prediction that the variance is constant for $t \ll$ Da and grows diffusively for $t \gg$ Da following Eq. (B.1) for Da ≤ 1 and Eq. (B.17) for Da > 1. We compare the variance growth in time obtained from numerical simulations with these predictions for different Damköhler numbers and β in Fig. C.3.

In all cases, simulations are found to be in good agreement with analytical solutions. Note that for $\beta < 1$, the variance computed from numerical simulations starts decreasing at the end of the simulations, which is not captured by our model (Fig. C.3, a). A short time before the whole profile reaches zero, concentrations on the sides are reacting faster than they diffuse so that the variance starts to decrease before the whole profile reaches zero. This regime of variance decay is thus very short.

6 Research data

Research Data associated with this article can be accessed at https://doi.org/10.5281/zenodo.4114532.

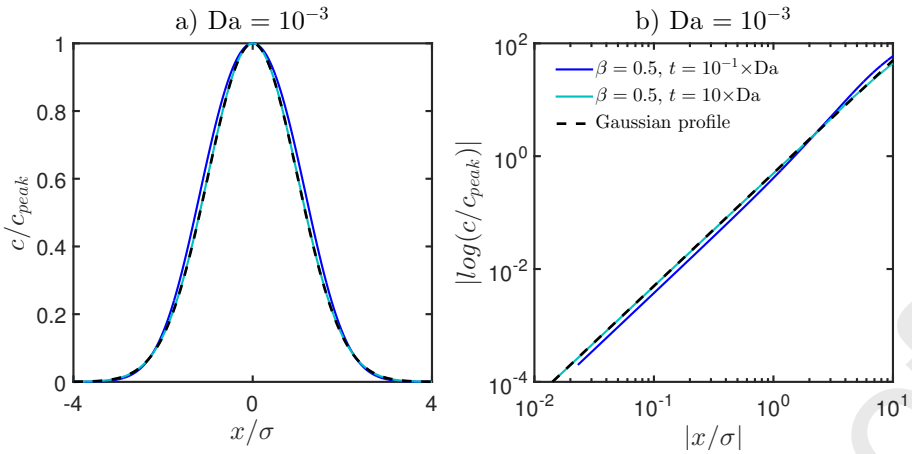

Figure C.2: Test of Gaussianity of reactive pulses from numerical simulations for $\beta = 0.5$. a) Comparison of reactive profiles, normalized by their peak values c_{peak} along the y axis and their standard deviation σ along the x axis, with Gaussian profiles at early and late times, $t \approx 10^{-1}\times$Da and $t \approx 10\times$Da for Da $= 10^{-3}$. The high Da profile is not represented because the mean concentration reaches zero before the times at which we assume Gaussianity, $t =$ Da. b) Test of Gaussian power law scaling represented by Eq. (C.1).

References

Aagaard, P. and H. C. Helgeson (1982). "Thermodynamic and kinetic constraints on reaction rates among minerals and aqueous solutions; I, Theoretical considerations". In: *American journal of Science* 282.3, pp. 237–285.

Abel, C. D. T., S. K. Sharma, S. A. Mersha, and M. D. Kennedy (2014). "Influence of intermittent infiltration of primary effluent on removal of suspended solids, bulk organic matter, nitrogen and pathogens indicators in a simulated managed aquifer recharge system". In: *Ecological engineering* 64, pp. 100–107.

Al-Yamani, W., S. Green, R. Pangilinan, S. Dixon, S. A. Shahid, P. Kemp, and B. Clothier (2019). "Water use of Al Samr (Acacia tortilis) forests irrigated with saline groundwater and treated sewage effluent in the hyper-arid deserts of Abu Dhabi". In: *Agricultural Water Management* 216, pp. 361–364.

Atchley, A. L., R. M. Maxwell, and A. K. Navarre-Sitchler (2013). "Using streamlines to simulate stochastic reactive transport in heterogeneous aquifers: Kinetic metal release and transport in CO2 impacted drinking water aquifers". In: *Advances in water resources* 52, pp. 93–106.

Atchley, A. L., A. K. Navarre-Sitchler, and R. M. Maxwell (2014). "The effects of physical and geochemical heterogeneities on hydro-geochemical transport and effective reaction rates". In: *Journal of contaminant hydrology* 165, pp. 53–64.

Bandopadhyay, A., P. Davy, and T. Le Borgne (2018). "Shear flows accelerate mixing dynamics in hyporheic zones and hillslopes". In: *Geophysical Research Letters* 45.21, pp. 11–659.

Battiato, I. and D. M. Tartakovsky (2011). "Applicability regimes for macroscopic models of reactive transport in porous media". In: *Journal of contaminant hydrology* 120, pp. 18–26.

Battiato, I., D. M. Tartakovsky, A. M. Tartakovsky, and T. Scheibe (2009). "On breakdown of macroscopic models of mixing-controlled heterogeneous reactions in porous media". In: *Advances in water resources* 32.11, pp. 1664–1673.

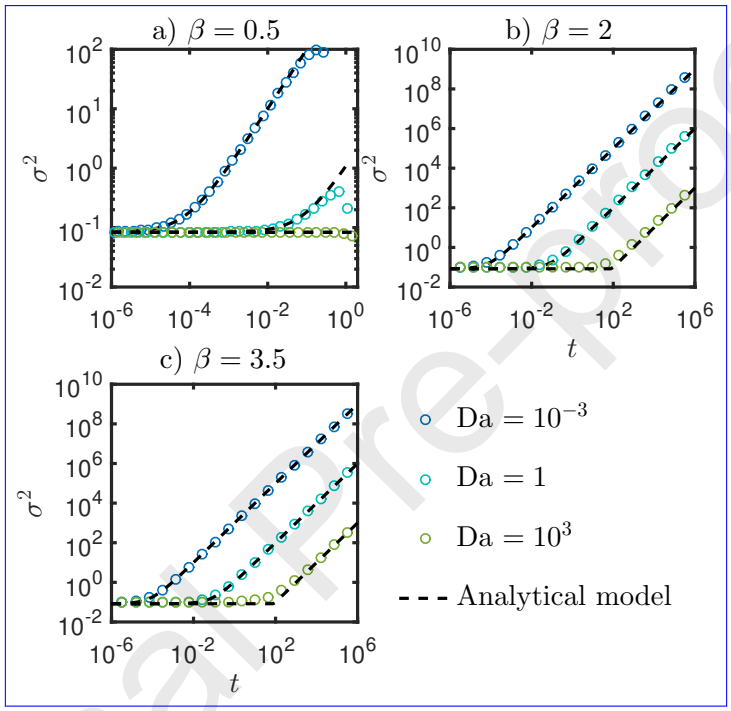

Figure C.3: Test of analytical model for variance growth. Temporal evolution of the reactive pulse variance for a) $\beta = 0.5$, b) $\beta = 2$, c) $\beta = 3.5$, and Da $= 0.001$ (blue circles), Da $= 1$ (turquoise circles), and Da $= 1000$ (green circles). The analytical model predictions, shown by black dashed lines, is given by Eq. (B.1) for Da ≤ 1 and Eq. (B.17) for Da ≥ 1

Beckingham, L. E., E. H. Mitnick, C. I. Steefel, S. Zhang, M. Voltolini, A. M. Swift, L. Yang, D. R. Cole, J. M. Sheets, J. B. Ajo-Franklin, et al. (2016). "Evaluation of mineral reactive surface area estimates for prediction of reactivity of a multi-mineral sediment". In: *Geochimica et Cosmochimica Acta* 188, pp. 310–329.

Beckingham, L. E., C. I. Steefel, A. M. Swift, M. Voltolini, L. Yang, L. M. Anovitz, J. M. Sheets, D. R. Cole, T. J. Kneafsey, E. H. Mitnick, et al. (2017). "Evaluation of accessible mineral surface areas for improved prediction of mineral reaction rates in porous media". In: *Geochimica et Cosmochimica Acta* 205, pp. 31–49.

Berkowitz, B., A. Cortis, M. Dentz, and H. Scher (2006). "Modeling non-Fickian transport in geological formations as a continuous time random walk". In: *Reviews of Geophysics* 44.2.

Bethke, C. (1996). *Geochemical reaction modeling: Concepts and applications*. Oxford University Press on Demand.

Bleam, W. (2017). "Chapter 9-reduction-oxidation chemistry". In: *Soil and Environmental Chemistry*, pp. 445–489.

Bochet, O., L. Bethencourt, A. Dufresne, J. Farasin, M. Pédrot, T. Labasque, E. Chatton, N. Lavenant, C. Petton, B. W. Abbott, et al. (2020). "Iron-oxidizer hotspots formed by intermittent oxic–anoxic fluid mixing in fractured rocks". In: *Nature Geoscience* 13.2, pp. 149–155.

Burté, L., C. A. Cravotta III, L. Bethencourt, J. Farasin, M. Pédrot, A. Dufresne, M.-F. Gerard, C. Baranger, T. Le Borgne, and L. Aquilina (2019). "Kinetic study on clogging of a geothermal pumping well triggered by mixing-induced biogeochemical reactions". In: *Environmental science & technology* 53.10, pp. 5848–5857.

Datta, S., B. Mailloux, H.-B. Jung, M. A. Hoque, M. Stute, K. M. Ahmed, and Y. Zheng (2009). "Redox trapping of arsenic during groundwater discharge in sediments from the Meghna riverbank in Bangladesh". In: *Proceedings of the National Academy of Sciences* 106.40, pp. 16930–16935.

De Anna, P., J. Jimenez-Martinez, H. Tabuteau, R. Turuban, T. Le Borgne, M. Derrien, and Y. Meheust (2014a). "Mixing and reaction kinetics in porous media: An experimental pore scale quantification". In: *Environmental Science and Technology* 48.1, pp. 508–516.

De Anna, P., M. Dentz, A. Tartakovsky, and T. Le Borgne (2014b). "The filamentary structure of mixing fronts and its control on reaction kinetics in porous media flows". In: *Geophysical Research Letters* 41.13, pp. 4586–4593.

DePaolo, D. J. and D. R. Cole (2013). "Geochemistry of geologic carbon sequestration: an overview". In: *Reviews in Mineralogy and Geochemistry* 77.1, pp. 1–14.

Deng, H., S. Molins, D. Trebotich, C. Steefel, and D. DePaolo (2018). "Pore-scale numerical investigation of the impacts of surface roughness: Upscaling of reaction rates in rough fractures". In: *Geochimica et Cosmochimica Acta* 239, pp. 374–389.

Dentz, M., T. Le Borgne, A. Englert, and B. Bijeljic (2011a). "Mixing, spreading and reaction in heterogeneous media: A brief review". In: *Journal of contaminant hydrology* 120, pp. 1–17.

— (2011b). "Mixing, spreading and reaction in heterogeneous media: A brief review". In: *Journal of Contaminant Hydrology* 120-121, pp. 1–17.

Dutta, T., A. Carles-Brangarí, D. Fernàndez-Garcia, S. Rubol, J. Tirado-Conde, and X. Sanchez-Vila (2015). "Vadose zone oxygen (O2) dynamics during drying and wetting cycles: an artificial recharge laboratory experiment". In: *Journal of Hydrology* 527, pp. 151–159.

Elberling, B, R. Nicholson, and J. Scharer (1994). "A combined kinetic and diffusion model for pyrite oxidation in tailings: a change in controls with time". In: *Journal of Hydrology* 157.1-4, pp. 47–60.

Fenwick, D., C. Scheidt, and J. Caers (2014). "Quantifying asymmetric parameter interactions in sensitivity analysis: application to reservoir modeling". In: *Mathematical Geosciences* 46.4, pp. 493–511.

Giammar, D. E., R. G. Bruant Jr, and C. A. Peters (2005). "Forsterite dissolution and magnesite precipitation at conditions relevant for deep saline aquifer storage and sequestration of carbon dioxide". In: *Chemical Geology* 217.3-4, pp. 257–276.

Gramling, C. M., C. F. Harvey, and L. C. Meigs (2002). "Reactive transport in porous media: A comparison of model prediction with laboratory visualization". In: *Environmental science & technology* 36.11, pp. 2508–2514.

Guo, J., M. Quintard, and F. Laouafa (2015). "Dispersion in porous media with heterogeneous nonlinear reactions". In: *Transport in Porous Media* 109.3, pp. 541–570.

Hellmann, R. and D. Tisserand (2006). "Dissolution kinetics as a function of the Gibbs free energy of reaction: An experimental study based on albite feldspar". In: *Geochimica et Cosmochimica Acta* 70.2, pp. 364–383.

Hermans, T., F. Nguyen, M. Klepikova, A. Dassargues, and J. Caers (2018). "Uncertainty quantification of medium-term heat storage from short-term geophysical experiments using Bayesian evidential learning". In: *Water Resources Research* 54.4, pp. 2931–2948.

Heyman, J., D. R. Lester, R. Turuban, Y. Méheust, and T. Le Borgne (2020). "Stretching and folding sustain microscale chemical gradients in porous media". In: *Proceedings of the National Academy of Sciences*.

Hinsinger, P., C. Plassard, C. Tang, and B. Jaillard (2003). "Origins of root-mediated pH changes in the rhizosphere and their responses to environmental constraints: a review". In: *Plant and soil* 248.1-2, pp. 43–59.

Hubbard, C. G., S. Black, and M. L. Coleman (2009). "Aqueous geochemistry and oxygen isotope compositions of acid mine drainage from the Río Tinto, SW Spain, highlight inconsistencies in current models". In: *Chemical Geology* 265.3-4, pp. 321–334.

Hubert, A., T. Aquino, H. Tabuteau, Y. Méheust, and T. Le Borgne (2020). "Enhanced and non-monotonic effective kinetics of solute pulses under Michaelis–Menten reactions". In: *Advances in Water Resources* 146, p. 103739.

Johnson, N. C., B. Thomas, K. Maher, R. J. Rosenbauer, D. Bird, and G. E. Brown Jr (2014). "Olivine dissolution and carbonation under conditions relevant for in situ carbon storage". In: *Chemical Geology* 373, pp. 93–105.

Jun, Y.-S., D. E. Giammar, and C. J. Werth (2013). *Impacts of geochemical reactions on geologic carbon sequestration*.

Jung, H. and A. Navarre-Sitchler (2018a). "Physical heterogeneity control on effective mineral dissolution rates". In: *Geochimica et Cosmochimica Acta* 227, pp. 246–263.

— (2018b). "Scale effect on the time dependence of mineral dissolution rates in physically heterogeneous porous media". In: *Geochimica et Cosmochimica Acta* 234, pp. 70–83.

Keiluweit, M., P. S. Nico, M. Kleber, and S. Fendorf (2016). "Are oxygen limitations under recognized regulators of organic carbon turnover in upland soils?" In: *Biogeochemistry* 127.2, pp. 157–171.

Kirchner, J. W. and C. Neal (2013). "Universal fractal scaling in stream chemistry and its implications for solute transport and water quality trend detection". In: *Proceedings of the National Academy of Sciences* 110.30, pp. 12213–12218.

Kitanidis, P. K. (1994). "The concept of the dilution index". In: *Water resources research* 30.7, pp. 2011–2026.

Kitanidis, P. K. and P. L. McCarty (2012). *Delivery and Mixing in the Subsurface: Processes and Design Principles for In Situ Remediation*. Vol. 4. Springer Science & Business Media.

Largitte, L. and R. Pasquier (2016). "A review of the kinetics adsorption models and their application to the adsorption of lead by an activated carbon". In: *Chemical Engineering Research and Design* 109, pp. 495–504.

Lasaga, A. C., J. M. Soler, J. Ganor, T. E. Burch, and K. L. Nagy (1994). "Chemical weathering rate laws and global geochemical cycles". In: *Geochimica et Cosmochimica Acta* 58.10, pp. 2361–2386.

Lazareva, O., G. Druschel, and T. Pichler (2015). "Understanding arsenic behavior in carbonate aquifers: Implications for aquifer storage and recovery (ASR)". In: *Applied Geochemistry* 52, pp. 57–66.

Le Borgne, T., M. Dentz, and E. Villermaux (2013). "Stretching, coalescence, and mixing in porous media". In: *Physical review letters* 110.20, p. 204501.

Le Borgne, T., T. R. Ginn, and M. Dentz (2014). "Impact of fluid deformation on mixing-induced chemical reactions in heterogeneous flows". In: *Geophysical Research Letters* 41.22, pp. 7898–7906.

Le Borgne, T., M. Dentz, and E. Villermaux (2015). "The lamellar description of mixing in porous media". In:

Le Borgne, T., P. D. Huck, M. Dentz, and E. Villermaux (2017). "Scalar gradients in stirred mixtures and the deconstruction of random fields". In:

Li, L., C. I. Steefel, and L. Yang (2008). "Scale dependence of mineral dissolution rates within single pores and fractures". In: *Geochimica et Cosmochimica Acta* 72.2, pp. 360–377.

Li, L., K. Maher, A. Navarre-Sitchler, J. Druhan, C. Meile, C. Lawrence, J. Moore, J. Perdrial, P. Sullivan, and A. e. a. Thompson (2017). "Expanding the role of reactive transport models in critical zone processes". In: *Earth-science reviews* 165, pp. 280–301.

Llewellyn, G. T., F. Dorman, J. L. Westland, D. Yoxtheimer, P. Grieve, T. Sowers, E. Humston-Fulmer, and S. L. Brantley (2015). "Evaluating a groundwater supply contamination incident attributed to Marcellus Shale gas development". In: *Proceedings of the National Academy of Sciences* 112.20, pp. 6325–6330.

Magesan, G. N., C. D. A. McLay, and V. V. Lal (1998). "Nitrate leaching from a free-draining volcanic soil irrigated with municipal sewage effluent in New Zealand". In: *Agriculture, ecosystems & environment* 70.2-3, pp. 181–187.

Maher, K. (2011). "The role of fluid residence time and topographic scales in determining chemical fluxes from landscapes". In: *Earth and Planetary Science Letters* 312.1-2, pp. 48–58.

Maher, K. and C. P. Chamberlain (2014). "Hydrologic regulation of chemical weathering and the geologic carbon cycle". In: *Science* 343.6178, pp. 1502–1504.

Maher, K. and A. Navarre-Sitchler (2019). "Reactive transport processes that drive chemical weathering: From making space for water to dismantling continents". In: *Reviews in Mineralogy and Geochemistry* 85.1, pp. 349–380.

Maher, K. and K. U. Mayer (2019). "The art of reactive transport model building". In: *Elements* 15.2, pp. 117–118.

Maher, K., C. I. Steefel, D. J. DePaolo, and B. E. Viani (2006). "The mineral dissolution rate conundrum: Insights from reactive transport modeling of U isotopes and pore fluid chemistry in marine sediments". In: *Geochimica et Cosmochimica Acta* 70.2, pp. 337–363.

Malmström, M. E., G. Destouni, S. A. Banwart, and B. H. E. Strömberg (2000). "Resolving the scale-dependence of mineral weathering rates". In: *Environmental science & technology* 34.7, pp. 1375–1378.

Malzone, J. M., C. S. Lowry, and A. S. Ward (2016). "Response of the hyporheic zone to transient groundwater fluctuations on the annual and storm event time scales". In: *Water Resources Research* 52.7, pp. 5301–5321.

McKibben, M. A. and H. L. Barnes (1986). "Oxidation of pyrite in low temperature acidic solutions: Rate laws and surface textures". In: *Geochimica et Cosmochimica Acta* 50.7, pp. 1509–1520.

Meile, C. and K. Tuncay (2006). "Scale dependence of reaction rates in porous media". In: *Advances in Water Resources* 29.1, pp. 62–71.

Molins, S., D. Trebotich, C. I. Steefel, and C. Shen (2012). "An investigation of the effect of pore scale flow on average geochemical reaction rates using direct numerical simulation". In: *Water Resources Research* 48.3.

Molins, S., D. Trebotich, L. Yang, J. B. Ajo-Franklin, T. J. Ligocki, C. Shen, and C. I. Steefel (2014). "Pore-scale controls on calcite dissolution rates from flow-through laboratory and numerical experiments". In: *Environmental science & technology* 48.13, pp. 7453–7460.

Moussout, H., H. Ahlafi, M. Aazza, and H. Maghat (2018). "Critical of linear and nonlinear equations of pseudo-first order and pseudo-second order kinetic models". In: *Karbala International Journal of Modern Science* 4.2, pp. 244–254.

Murphy, S. F., R. B. McCleskey, D. A. Martin, J. H. Writer, and B. A. Ebel (2018). "Fire, flood, and drought: extreme climate events alter flow paths and stream chemistry". In: *Journal of Geophysical Research: Biogeosciences* 123.8, pp. 2513–2526.

Navarre-Sitchler, A. and S. Brantley (2007). "Basalt weathering across scales". In: *Earth and Planetary Science Letters* 261.1-2, pp. 321–334.

Palandri, J. L. and Y. K. Kharaka (2004). *A compilation of rate parameters of water-mineral interaction kinetics for application to geochemical modeling.* Tech. rep. Geological Survey Menlo Park CA.

Panfilov, M. (2010). "Underground storage of hydrogen: in situ self-organisation and methane generation". In: *Transport in porous media* 85.3, pp. 841–865.

Perry, R. H., D. W. Green, and J. O. Maloney (1997). "Perry's handbook of chemical engineering". In: *Perry's Handbook of Chemical Engineering.*

Plummer, L. N. and T. M. L. Wigley (1976). "The dissolution of calcite in CO2-saturated solutions at 25 C and 1 atmosphere total pressure". In: *Geochimica et Cosmochimica Acta* 40.2, pp. 191–202.

Pujades, E., S. Orban P.and Bodeux, P. Archambeau, S. Erpicum, and A. Dassargues (2017). "Underground pumped storage hydropower plants using open pit mines: How do groundwater exchanges influence the efficiency?" In: *Applied energy* 190, pp. 135–146.

Robati, D. (2013). "Pseudo-second-order kinetic equations for modeling adsorption systems for removal of lead ions using multi-walled carbon nanotube". In: *Journal of nanostructure in Chemistry* 3.1, p. 55.

Rolle, M. and T. Le Borgne (2019). "Mixing and reactive fronts in the subsurface". In: *Reviews in Mineralogy and Geochemistry* 85.1, pp. 111–142.

Rudzinski, W. and W. Plazinski (2006). "Kinetics of solute adsorption at solid/solution interfaces: a theoretical development of the empirical pseudo-first and pseudo-second order kinetic rate equations, based on applying the statistical rate theory of interfacial transport". In: *The Journal of Physical Chemistry B* 110.33, pp. 16514–16525.

Salehikhoo, F., L. Li, and S. L. Brantley (2013). "Magnesite dissolution rates at different spatial scales: The role of mineral spatial distribution and flow velocity". In: *Geochimica et Cosmochimica Acta* 108, pp. 91–106.

Serrano, S. E. (2001). "Solute transport under non-linear sorption and decay". In: *Water Research* 35.6, pp. 1525–1533.

— (2003). "Propagation of nonlinear reactive contaminants in porous media". In: *Water Resources Research* 39.8.

Skeel, R. D. and M. Berzins (1990). "A method for the spatial discretization of parabolic equations in one space variable". In: *SIAM journal on scientific and statistical computing* 11.1, pp. 1–32.

Song, X., J. Zhang, C. Zhan, Y. Xuan, M. Ye, and C. Xu (2015). "Global sensitivity analysis in hydrological modeling: Review of concepts, methods, theoretical framework, and applications". In: *Journal of hydrology* 523, pp. 739–757.

Soulaine, C., S. Roman, A. Kovscek, and H. A. Tchelepi (2017). "Mineral dissolution and wormholing from a pore-scale perspective". In:

Steefel, C. I. and A. C. Lasaga (1994). "A coupled model for transport of multiple chemical species and kinetic precipitation/dissolution reactions with application to reactive flow in single phase hydrothermal systems". In: *American Journal of science* 294.5, pp. 529–592.

Steefel, C., C. Appelo, B. Arora, D. Jacques, T. Kalbacher, O Kolditz, V. Lagneau, P. Lichtner, K. U. Mayer, J. Meeussen, et al. (2015). "Reactive transport codes for subsurface environmental simulation". In: *Computational Geosciences* 19.3, pp. 445–478.

Steefel, C. I., D. J. DePaolo, and P. C. Lichtner (2005). "Reactive transport modeling: An essential tool and a new research approach for the Earth sciences". In: *Earth and Planetary Science Letters* 240.3-4, pp. 539–558.

Szulczewski, M. L., C. W. MacMinn, H. J. Herzog, and R. Juanes (2012). "Lifetime of carbon capture and storage as a climate-change mitigation technology". In: *Proceedings of the National Academy of Sciences* 109.14, pp. 5185–5189.

Trauth, N. and J. H. Fleckenstein (2017). "Single discharge events increase reactive efficiency of the hyporheic zone". In: *Water Resources Research* 53.1, pp. 779–798.

Urióstegui, S. H., R. K. Bibby, B. K. Esser, and J. F. Clark (2016). "Quantifying groundwater travel time near managed recharge operations using 35S as an intrinsic tracer". In: *Journal of Hydrology* 543, pp. 145–154.

Valocchi, A. J., D. Bolster, and C. J. Werth (2019). "Mixing-limited reactions in porous media". In: *Transport in Porous Media* 130.1, pp. 157–182.

Van Cappellen, P. and J.-F. Gaillard (2018). "Biogeochemical dynamics in aquatic sediments". In: *Reactive transport in porous media*, pp. 335–376.

Villermaux, E. (2019). "Mixing versus stirring". In: *Annual Review of Fluid Mechanics* 51, pp. 245–273.

Wang, L., H. Wen, and L. Li (2018). "Scale dependence of surface complexation capacity and rates in heterogeneous media". In: *Science of The Total Environment* 635, pp. 1547–1555.

Weber J., W. J., P. M. McGinley, and L. E. Katz (1991). "Sorption phenomena in subsurface systems: concepts, models and effects on contaminant fate and transport". In: *Water research* 25.5, pp. 499–528.

Wen, H. and L. Li (2017a). "An upscaled rate law for magnesite dissolution in heterogeneous porous media". In: *Geochimica et Cosmochimica Acta* 210, pp. 289–305.

— (2017b). "An upscaled rate law for magnesite dissolution in heterogeneous porous media". In: *Geochimica et Cosmochimica Acta* 210, pp. 289–305.

— (2018). "An upscaled rate law for mineral dissolution in heterogeneous media: The role of time and length scales". In: *Geochimica et Cosmochimica Acta* 235, pp. 1–20.

White, A. F. and S. L. Brantley (2003). "The effect of time on the weathering of silicate minerals: why do weathering rates differ in the laboratory and field?" In: *Chemical Geology* 202.3-4, pp. 479–506.

Wu, F.-C., R.-L. Tseng, S.-C. Huang, and R.-S. Juang (2009). "Characteristics of pseudo-second-order kinetic model for liquid-phase adsorption: a mini-review". In: *Chemical Engineering Journal* 151.1-3, pp. 1–9.

961 Xu, T., S. P. White, K. Pruess, and G. H. Brimhall (2000). "Modeling of pyrite oxidation in
962 saturated and unsaturated subsurface flow systems". In: *Transport in porous media* 39.1,
963 pp. 25–56.
964 Yang, C., J. Samper, J. Molinero, and M. Bonilla (2007). "Modelling geochemical and microbial
965 consumption of dissolved oxygen after backfilling a high level radiactive waste repository".
966 In: *Journal of Contaminant Hydrology* 93.1-4, pp. 130–148.

Declaration of interests

☒ The authors declare that they have no known competing financial interests or personal relationships that could have appeared to influence the work reported in this paper.

☐The authors declare the following financial interests/personal relationships which may be considered as potential competing interests: